FH AACHEN
UNIVERSITY OF APPLIED SCIENCES

FH Aachen Campus Jülich

Faculty 3 Chemistry and Biotechnology

European Master of Nuclear Applications

Preparation and characterization of U / Nd microspheres synthesized by internal gelation

Master Thesis by

Christian Schreinemachers, Dipl.-Ing. (FH)

Jülich, April 2013

The experimental work was carried out at Forschungszentrum Jülich GmbH in the Institute of Energy and Climate Research, IEK-6: Nuclear Waste Management and Reactor Safety.

This work was supervised by:

Prof. Dr. rer. nat. U. W. Scherer

Dr. rer. nat. G. Modolo

Declaration

This thesis is my own independent work and is the result of my sole efforts. No other sources or references have been used in its production apart from the quoted ones.

Jülich, April 25, 2013

CHRISTIAN SCHREINEMACHERS

Abstract

In the context of advanced nuclear fuel cycles including partitioning and transmutation (P&T), actinide co-conversion processes play an important role. Therefore actinide ceramics are considered to be used as precursor for the fabrication of innovative fuels.

A suitable conversion method is the sol-gel route by internal gelation. It's advantage is the prevention of dust formation during synthesis and the fact, that spherical particles are already formed at the gel stage. Within the framework of the EU project ASGARD (FP7 Euratom) preparation of UO_2 / Nd_2O_3 microspheres is studied.

The present work shows that the preparation of UO_2 / Nd_2O_3 with Nd contents up to $\approx 45\,\%$ is possible by the internal gelation technique. ADUN solutions were used as precursor for the fabrication of the microspheres. U / Nd green bodies in a χ(Nd) range of $0 - 42.63\,\%$ were synthesized.

Although the process was manual, an average particle mass with a small standard deviation was achieved. A spherical particle shape was proven by SEM and with optical microscopy. The green body diameter was measured and a particle density was calculated.

The thermal behavior of the U / Nd microspheres was investigated by TG/DSC, in the region of 550-700 °C the particle compositions with $\chi(\mathrm{Nd}) \leq 17.40\,\%$ transit endothermic accompanied with an stepwise mass loss. The spheres containing higher Nd amounts showed an exothermic effect.

XRD analyses show orthorhombic and cubic crystal lattice structure of the particle compositions treated in air ($\vartheta = 1300\,°\mathrm{C}$), which agrees with SEM investigations. The lattice parameter of the cubic structure was determined. The result of this analyses goes in accordance with published data [33] and a crystallization as described in a phase diagram for higher temperature was confirmed.

Investigation of the control group powders, treated in a reducing H_2:Ar atmosphere at 1300 °C, showed in a χ(Nd) range of 13-26.4 % a formation of two cubic phases. This goes in accordance to published data [39]. Comparisons with further reference data shows that formation of a UO_2 / Nd_2O_3 single phase composition is difficult for this χ(Nd) range.

The particles, synthesized by internal gelation and treated in H_2:Ar atmosphere ($\vartheta = 1300\,°\mathrm{C}$) showed only one cubic phase, for the whole observed χ(Nd) range. However, the expected linear behavior according to Vegard's rule was observed for compositions $\chi(\mathrm{Nd}) \leq 27.59\,\%$, only. An additional sintering process of the particles with compositions of $\chi(\mathrm{Nd}) \geq 33.49\,\%$ at a higher temperature ($\vartheta = 1600\,°\mathrm{C}$) for 5 hours led to the expected crystallization of a single phase UO_2 / Nd_2O_3 ceramic behaving to Vegard's rule.

The results of this work show that equilibrium solid solutions of the sensitive UO_2 / Nd_2O_3 system can be fabricated by the internal gelation synthesis route with Nd contents of $\leq 42.63\,\%$.

Contents

1. Introduction

The steady growth of the world population in the long run leads to a greater demand for energy. This fact calls for a sustainable, competitive and secure energy for the future. Several kinds of energy sources are available, each having advantages and disadvantages.

Wind or solar energy, the renewable energy sources, present a high sustainability and are environmentally friendly but their reliability is limited. Due to this reasons they can not be used exclusively.

Combustion of fossil fuels, such as coal, oil or natural gas are currently the main source of energy in the world. It is easy to procure and reliable. But the large quantities of carbon dioxide, emitted during the combustion process, are considered to be a major contribution to the greenhouse effect.

Energy generated by nuclear fission provides the benefits of an abundant fuel and no emissions of carbon dioxide, but the public acceptance of this energy source is low, especially due to the production of high level radioactive waste. Therefore, an innovative waste management strategy reducing the spent fuels radiotoxicity is of prime importance to improve the public acceptance of this energy source.

In the year 2011 the net electricity generation from nuclear power was about 2.500×10^{12} kWh worldwide. This a reduction compared to 2010 (2.630×10^{12} kWh) [1], which can be largely explained on the shutdowns of Japanese reactors after the Fukushima accident. Another consequence of the accident is the disconnection of 8 nuclear power plants in Germany. The share of nuclear power in global electricity generation in 2011 was around 12 %. The EU is the world's leading economic region in the production of nuclear energy with approximately 870×10^{9} kWh in 14 member states [1].

Considering the trend of the last 50 years, the growth of nuclear power in the 1980s is remarkable. During this time large nuclear power plants went to operation. They were projects which began in the wake of the first oil price crisis and provided a power of ≥ 1.000 MW per block. This still provides considerable production capacities.

Today, the operation of nuclear power plants is characterized by a continued high availability of the global average close to 80 %. Currently, in 31 countries, 437 nuclear power plants with a total power of 390 213 MW are operated worldwide. 67 nuclear reactors are under construction and about 200 more in planning or pre-planning stage to commissioning by 2030 [1].

2. Basics and Background

The present work deals with the fabrication of oxidic uranium / neodymium microspheres. This particles simulate a fuel for innovative nuclear reactors. The following section describes the physical fission process as well as the principle of a nuclear power plant briefly. Afterwards a short introduction into the chemistry of uranium is given, followed by different methods of nuclear fuel fabrication. Furthermore, the used measurement technique as well as the scope of work are described.

2.1. Power generation by nuclear fission

A neutron induced nuclear fission can be generally described as a reaction according to equation (2.1). The fissionable nucleus is symbolized as A, while B and D represent fission products. The energy released during this process is described as ΔE and ν represent the number of neutrons ($^{1}_{0}\mathrm{n}$) emitted.

$$\mathrm{A} + {}^{1}_{0}\mathrm{n} \longrightarrow \mathrm{B} + \mathrm{D} + \nu\,{}^{1}_{0}\mathrm{n} + \Delta E \tag{2.1}$$

The average binding energy per nucleon E_B/A is shown in Figure 2.1. Elements of a mass around 230-240 u have an average binding energy per nucleon of $\approx 7.5\,\mathrm{MeV}$. Nuclei having a mass of 80-150 u show a value of 8.4 MeV, these nuclei appear as fission products. The difference in the average binding energy per nucleon of round about 0.9 MeV, the sum of E_B/A is equal to the amount of energy that is emitted during a fission process of such a heavy nucleus. Due to the fact that this nuclei consists of 230–240 nucleons, the delivered energy per fission is about 200 MeV. Heavy elements are also used due to the fact, that ν is equal to 2–3, which enables a sustaining chain reaction of this fisson process.

The nuclear reaction that takes place if an neutron hits an heavy nucleus is not only depending on the nucleus itself, also on the neutron's energy. Besides fission reactions, neutron capture reactions (n, γ) are possible, which increases the nuclear mass by one, furthermore gamma photons are released. The *cross-section* (σ) describes the probability that a nuclear reaction with a neutron takes place and has the unity *barn* ($1\,\mathrm{b} = 10^{-28}\,\mathrm{m}^2$). Excitation functions for neutron fission (σ_f) reactions, and neutron capture ($\sigma_{n,\gamma}$) reactions, in dependency of the neutrons energy are shown in Figure 2.2. The neutron energy is displayed in electron Volt (eV) and there are graphs plotted for ^{232}Th, ^{235}U, ^{238}U and ^{239}Pu.

As already mentioned, the cross-section of a chosen reaction mainly depends on the kinetic energy of the incident particle. Summarized one can say that the probability for a certain nuclear

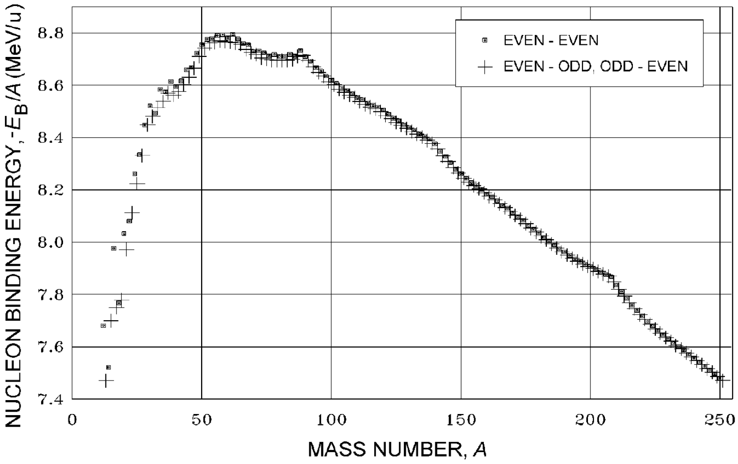

Figure 2.1.: Binding energy per nucleon E_B/A for the most stable isobars as function of mass number A, [2].

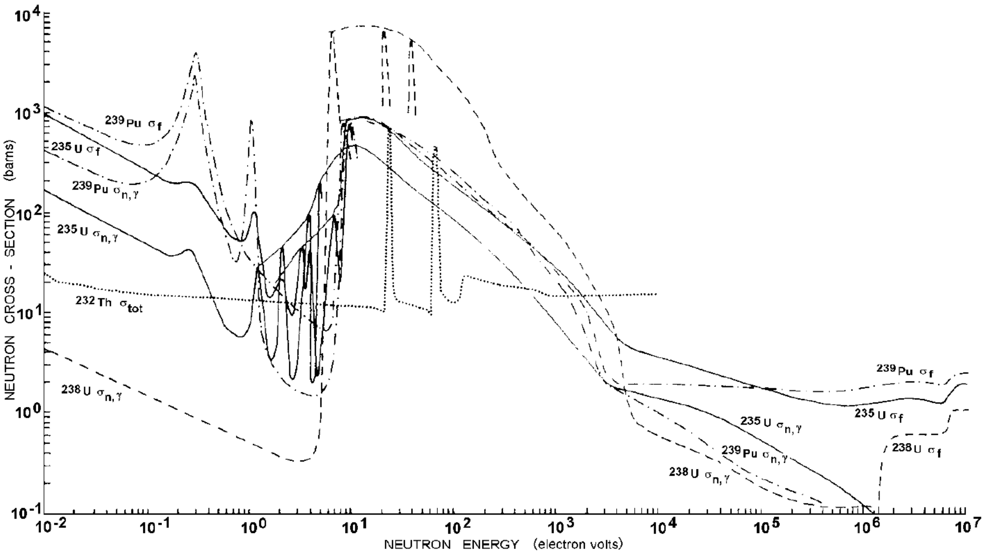

Figure 2.2.: Cross-sections for n-capture ($\sigma_{n,\gamma}$), fission (σ_f), and total (σ_{tot}) as a function of neutron energy, [2].

reaction is a function of the energy transferred to the nucleus by the incident particle. These energy dependencies are called *excitation function.* Due to the effect that neutrons are not charged they are not able to undergo Coulomb forces and interact, with high σ values, in low energy regions. The higher their velocity is, the shorter is the retention time next to the nucleus and the probability for an interaction. So one can observe an inversely proportional relation between the cross-section and the kinetic energy of the neutron. This relation is valid for energy regions $\leq 1\,\mathrm{eV}$ of all nuclei and reactions shown in Figure 2.2. At higher energies one can recognize maxima (resonance peaks). At these positions, the kinetic energy is equal to the excitation energy of the nucleus, which increases the reaction yield remarkable. Afterwards a continuing decrease of σ can be recognized. Due to this reaction regions the neutrons are classified, it is distinguished between

- cold neutrons ($\leq 2\,\mathrm{meV}$),
- thermal neutrons ($\leq 100\,\mathrm{meV}$),
- epithermal neutrons ($\leq 1\,\mathrm{eV}$) and
- fast neutrons ($10\,\mathrm{keV} - 20\,\mathrm{MeV}$).

The fission process can be presented as follows. Trigger of the nuclear fission is the capture of a neutron by a nucleus. The binding energy of the neutron is distributed as excitation energy to the nucleus, resulting its deformation. This may lead to the fission into to two fragments and a few neutrons (2.4 for the fission of ^{235}U and 2.9 for the fission of ^{239}Pu). An overview of the chain yields delivered by fission of ^{235}U with thermal neutrons, as well as for other common nuclei, are shown in 2.3.

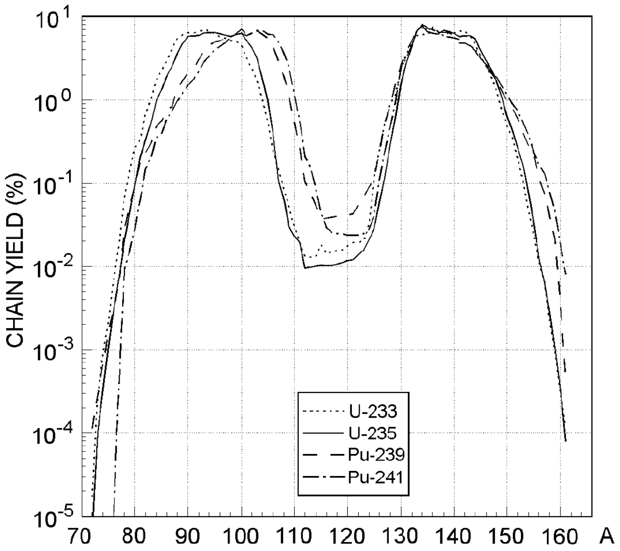

Figure 2.3.: Chain yield curves for ^{233}U, ^{235}U, ^{239}Pu and ^{241}Pu fission with thermal neutrons, [2].

2.1.1. The nuclear reactor

A nuclear reactor is a device that ensures a self-sustaining chain reaction in a safe environment. Fission reactors are in general distinguished by their neutron spectra. On the one hand a thermal reactor, and on the other hand fast neutron reactor. But due to the existence of a lot of different reactor subtypes, they are further classified by the following criteria [3]:

- fuel (e. g. U_{nat}, enriched U, Pu),
- moderator (e. g. graphite, heavy water, light water),
- distribution of fuel and moderator (homogeneous reactors, which means moderator and fuel are in the same phase, or heterogeneous reactors, separated assembling of fuel and moderator),
- coolant (e. g. gas cooled reactors, water cooled reactors, malten salt reactors) and
- application (research reactor or power reactor).

The principle of a nuclear power reactor, is like the one of a conventional fossil combustion plant. Steam drives a turbine, followed by alternator, which converted the kinetic energy into electrical energy. The difference is the way how the steam is generated. Fissionable material is placed into a pool, due too the fission the surrounding media is heated up, and in the case of water steam is generated. Quite common power reactor designs are the boiling water reactor (BWR), which works as described and the pressurized water reactor (PWR), which has a second water loop to avoid a contact of contaminated water and the turbine. Both operate with usual water and are, due to this, classified as light water reactors.

A schematic cross section of a PWR is shown in Figure 2.4. Highlighted in red is the so called *primary loop*, which consists of the *reactor core* (fuel) and the *control rods*. They are placed in the *reactor vessel*, which is connected to a *pressurizer* (to ensure a constant pressure). The water circuits are driven by pumps. Blue marked is the secondary circuit where the *steam generator* is working as a heat exchanger. As the name already implied this is the place where water is converted into steam, which drives the *alternator*, that is followed. Finally, the condenser cools the steam down to water, which is led back to the steam generator again. These circuits are isolated from the environmental by the *containment structure*.

The early prototypes were built in the 1950s and are called *Generation I* reactors, they were built up to the middle of the 1960s. *Generation II* describe commercial power plants, like that which are currently operating in Germany. A BWR and a PWR (compare fig. 2.4), are only a few examples for this reactor class. They were built up to the middle of the 90s and were replaced by the *Generation III* reactors.

Since these days reactors developed with an evolutionary design are built as *Generation III+* systems. The *european pressurized water reactor* EPR is one example.

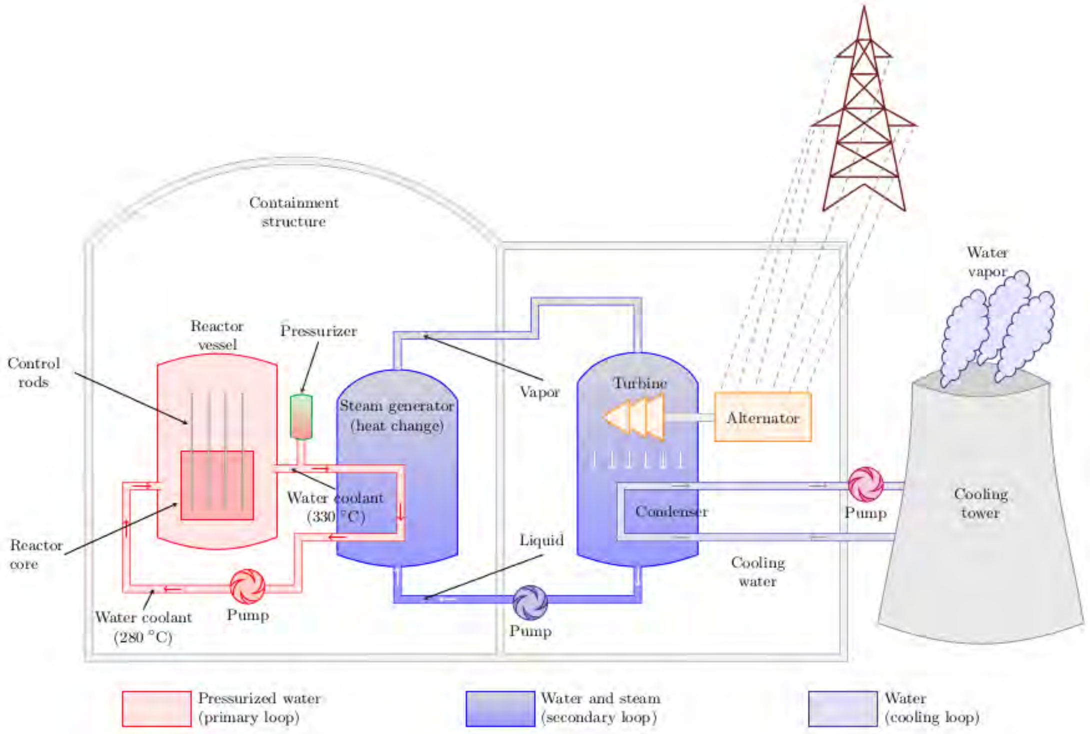

Figure 2.4.: Diagram of a pressurized water reactor, according to Faccanoni [4].

2.2. Chemical properties of uranium

Uranium is a radioactive element with three natural isotopes: ^{234}U, ^{235}U and ^{238}U. The natural abundance, as well as the radioactive half-life are shown in Table 2.1 [5]. All isotopes decay by α mode. ^{238}U and ^{234}U decay according to the *4n chain* (thorium chain) and end up as stable ^{208}Pb isotope, while the ^{235}U ends up as stable ^{207}Pb isotope, according to the *4n+3 chain* (actinium chain).

Table 2.1.: Natural uranium isotopes, data according to Magill et al. [5].

Isotope	Abundance / %	Half-life / a
^{234}U	0.0054	2.455×10^5
^{235}U	0.7204	7.038×10^8
^{238}U	99.2742	4.468×10^9

In nature, uranium mainly appears as *pitchblende* with a chemical composition that is largely UO_2, but also containing UO_3 and oxides of lead, thorium and rare earth elements. The largest pitchblende deposits are located in the State of the Congo and in the Czech Republic. A further mineral consisting of triuranium octoxide U_3O_8 is *uraninite*. Uranium is recovered by mining. The ore is crushed and milled, and a separation by physical and chemical processes from the other rocks is done. Then a leaching with an acid or a base and the presence of an oxidant (e. g. MnO_2, Na_2ClO_3) takes place. The oxidation is necessary to convert the uranium, present in the ore in oxidation state +IV, poorly soluble, to the hexavalent form, which is highly soluble. Equation (2.2) shows an example for such a leaching process, using H_2SO_4 [6].

$$UO_2 + H_2SO_4 + \frac{1}{2}O_2 \longrightarrow UO_2(SO_4) + H_2O \tag{2.2}$$

By extraction with the aid of an acid, up to 90 % of the containing uranium can be obtained from the ore. The uranyl sulfate ($UO_2(SO_4)$) contains a number of impurities, which are removed in further purification processes (decantation, filtration, solvent extraction, ion exchange, etc.). Then an addition of MgO, NaOH or NH_3 takes place, to precipitate the uranium from the solution. By the use of NH_3 ammonium diuranate is formed, which precipitates as $(NH_4)_2U_2O_7$. It is thickened, filtered, washed and dried. Because of its yellow color, it was given the name *yellow cake*. The concentrate, fabricated in modern plants, is about 80 % of U_3O_8.

Uranium +VI Thermal treatment of uranium +VI salts lead to the red / yellow colored uranium trioxide UO_3. It is soluble in acids as well as in bases. In the case of acids uranates (${UO_4}^{2+}$) are formed (which immediately convert to diuranates ${U_2O_7}^{2+}$) and end up as uranyl compound (${UO_2}^{2+}$). They are derived from uranic acid $UO_2(OH)_2$ (uranyl hydroxide) which has, in contrast to sulfuric acid with the same structure $SO_2(OH)_2$, acidic and basic properties. This is visualized in equation (2.3) [7].

$${UO_4}^{2-} + 2\,H^+ \rightleftharpoons UO_2(OH)_2 \rightleftharpoons {UO_2}^{2+} + 2\,OH^- \tag{2.3}$$

Uranium appears in its halogenide compounds only towards F and Cl in the hexavalent state: UF_6 (monoclinic non colored crystals, $T_M = 69.2\,°C$ (triple point), $T_B = 56.2\,°C$ (sublimation), UCl_6 (monoclinic green crystals) [7].

Uranium +IV Uranium trioxide UO_3 can be converted to uranium dioxide UO_2, by thermal treatment at 900 °C in a hydrogen atmosphere [7]. Uranium dioxide is black colored and has a density of $10.97\,\frac{g}{cm^3}$. It has a melting point of $T_M = 2200\,°C$ and a crystal structure according to the fluorite type (cubic, $a = 5.4682\,Å$, [8]). The crystal lattice of UO_2 is presented in Figure 2.5. The green sphere indicates the U^{4+} cation with a coordination number of 8, while the O^{2-} anion (coordination number: 4) is indicated by the red sphere. UO_2 behaves like a base. In the case of calcination in air, UO_3 and UO_2 will form the green colored U_3O_8. Triuranium octoxide can be seen as a mixture, consisting of $UO_2 \cdot 2\,UO_3$.

Uranium +III By the use of strong reducing agents, also trivalent uranium compounds can be formed, e. g. UBr_3 (dark red colored crystals) and UI_3 (black colored crystals). They are oxidized to uranium +IV compounds by H_2 release, in water.

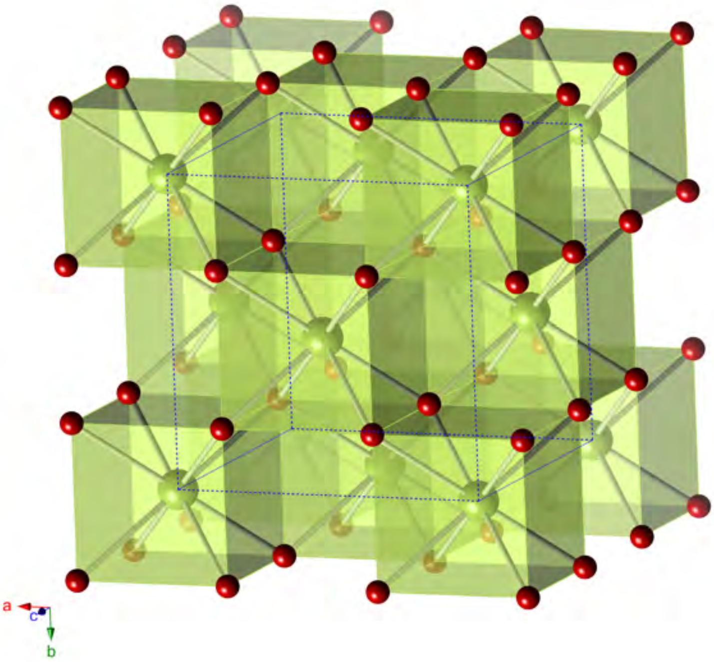

Figure 2.5.: The UO_2 crystal lattice according to Barrett et al. [8].

2.3. Nuclear fuel cycle

The nuclear fuel cycle describes the required steps for the supply of a nuclear power plant with fuel elements (front-end) and the disposal of spent fuel (back-end). The front-end includes the steps uranium ore mining, conversion, enrichment and fuel fabrication. For the disposal of spent fuel it can be chosen between the direct disposal (once through) and the reprocessing including final storage (twice through), as shown in figure 2.6.

Front end The precursor material of the nuclear fuel cycle's front end is the uranium ore, it is mined and treated as described in the section 2.2 (p. 7). Due to the fact that only ^{235}U is fissible and its abundance of 0.7204 % is to low to ensure a critical mass within a LWR, the isotope ratio of the uranium is changed to ^{235}U contents of 3-5 %. Furthermore, the technical quality of the yellow cake is improved. Impurities may lead to a higher neutron absorption cross section and disturbing side reactions.

To fulfill this so called enrichment process, the yellow cake is converted to gaseous uranium hexafluoride (conversion). During this conversion several chemical reactions are necessary which improve the chemical purity as well. As already mentioned, UF_6 sublimates at normal pressure at a temperature of 56.2 °C. The gaseous UF_6 is cleaned from contained solids by filtering and from other gases by freezing them out. With a purity of 99.5 %, it is stored in steel containers and transported to the enrichment plant. Different methods are developed for enrichment: the diffusion, centrifuge and separating nozzles procedures. The most common technique nowadays is the centrifugal enrichment.

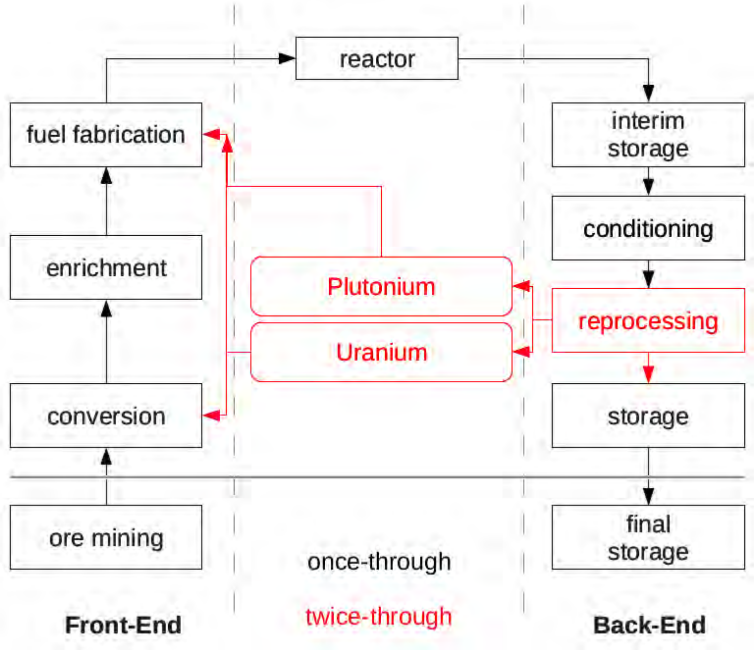

Figure 2.6.: The nuclear fuel cycle.

The nuclear fuel fabrication plant converts the in ^{235}U enriched UF_6 to UO_2 by the use of a dry or wet chemical method. The UF_6 is being reacted with ammonia and CO_2 in water, which will form ammonium uranyl carbonate (AUC, compare equations (2.4) and (2.5)) [6].

$$UF_6 + 2\,H_2O \longrightarrow UO_2F_2 + 4\,HF \tag{2.4}$$

$$UO_2F_2 + 6\,NH_3 + 8\,CO_2 + 3\,H_2O \longrightarrow (NH_4)_4[UO_2(CO_3)_3] + 2\,NH_4F \tag{2.5}$$

The yellow colored AUC precipitates from the solution and can be separated by filtering. Ammonia, CO_2, HF are separated from the UO_3 by heating. Afterwards, it is reduced in an hydrogen atmosphere at high temperatures to the UO_2 (compare *Uranium chemistry*, p. 7). The UO_2 occurs as grey colored powder, for the use in LWR it is pressed to pellets. These green bodies are sintered at a temperature of 1700 °C in a reducing hydrogen atmosphere. In the further fabrication process a polishing takes place and the pellets are transfered into the cladding tubes. Afterwards, these rods are filled with helium gas (1-30 bar) and sealed by welding. The fuel rods produced in this way are assembled to a fuel element (mostly consisting of 144 or 196, depending on their application). Further nuclear fuel fabrication methods, as well as special fuels for unconventional purposes, are introduced in the subsection *Fuel Fabrication* on page 15.

Reactor operation The fuel is used in a nuclear reactor for several years. According to a defined schedule, their position is changed to optimize their burn up during this process. Due to a decrease of fissionable inventory and increase of fission products in the fuel, they have to be renewed after some time. During the annual reactor revision these fuel elements are exchanged and the spent fuel elements are stored in a pool next to the reactor. During the operation period the content of the fuel has changed significantly:

- The fissile ^{235}U is used partly by nuclear fission and partly by converting it into ^{236}U. Radioactive fission products are formed. The consumption of fissile material is called burn-up. The degree of burn-up is measured in thermal energy generated per mass fuel. In light water reactors average burn-up values of 45 $\frac{\mathrm{MWd}}{\mathrm{kg}}$ are achieved (1 MWd = 24.000 kWh).
- By neutron capture reactions with ^{238}U, the plutonium isotope ^{239}Pu produced. The ^{239}Pu is partly fissioned by thermal neutrons or converted to other actinides. Due to other (n,γ) reactions further actinides are formed. Due to their small amount, they are called *minor actinides* (MA). Figure 2.7 gives an overview about the nuclear processes taking place in the fuel, during reactor operation.

A whole branch of *transuranium* (TRU) isotopes are formed. The ^{235}U and the ^{238}U are initially in the fuel, the scheme is organized like a nuclide chart.

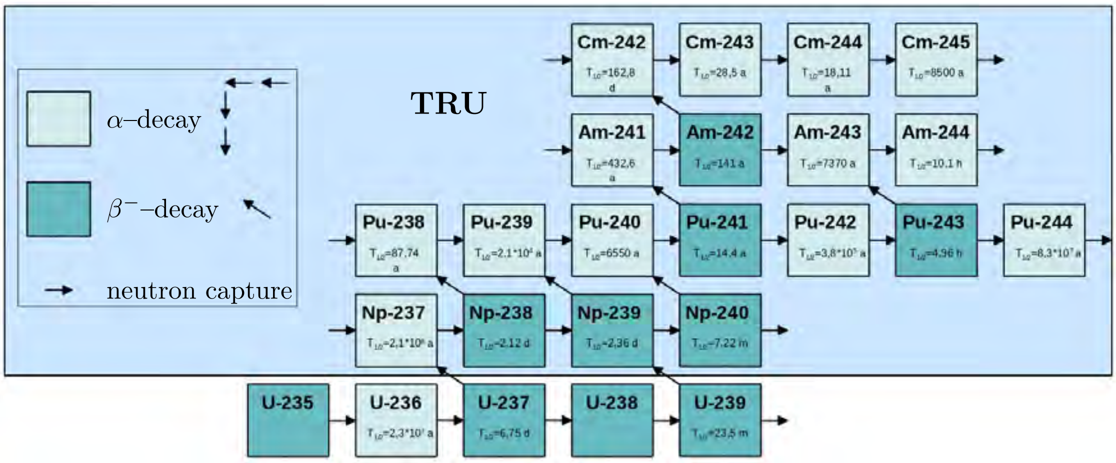

Figure 2.7.: Nuclear reactions of uranium during irradiation.

Figure 2.8 shows the composition of fresh fuel and spent fuel for light water reactors (data taken from Volkmer [6]). In both cases ^{238}U contributes the major part. The fresh fuel was enriched to a ^{235}U content of 3.3 %. Within a burn-up of 33 $\frac{\mathrm{MWd}}{\mathrm{kg}}$, 0.86 % ^{235}U are still left in the fuel. Furthermore the spent fuel consists of 0.42 % ^{236}U formed by (n,γ) reactions. The fission products (FP) contribute 3.25 % to the mass. The mass content of the minor actinides (MA), like Np, Am and Cm, is quite small (0.06 %) but they are interesting due to their high radiotoxicity. Furthermore, 0.93 % of the spent fuels mass is Pu generated by (n,γ) reactions. 94.48 % of the initial ^{238}U content is still remaining in the fuel.

The contribution of the actinides and fission products to the radiotoxicity of one ton of spent fuel is shown in Figure 2.9. It can be seen clearly that the major part of the radiotoxicity in the first

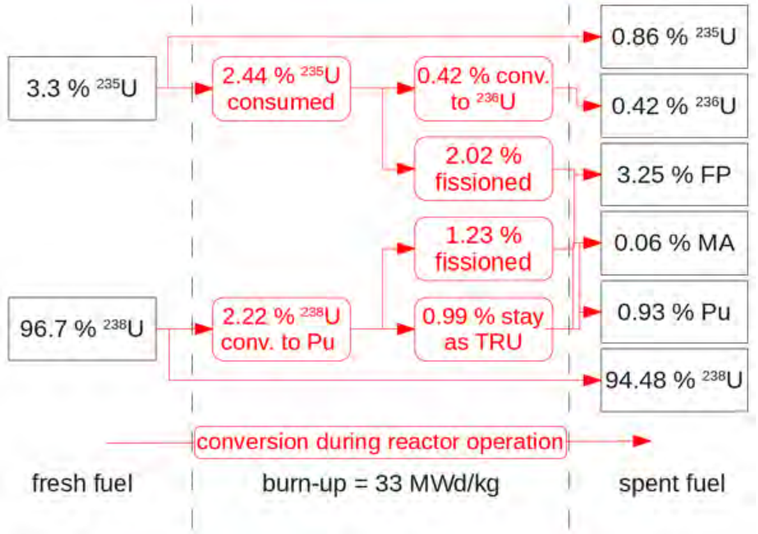

Figure 2.8.: The composition of fresh and spent LWR fuel.

100 years originates from the fission products. Plutonium and minors actinides, mainly americium, are responsible for the long term radiotoxicity of the spent fuel.

Radioactive waste is divided into different classes, the criteria have changed over the years. A classification of the waste in low active waste (LAW), medium active waste (MAW) and high active waste (HAW) was done previously, based on the dose rate only. As for the safety assessment of the disposal heat generation is of interest, they are now in heat-generating waste and those with negligible heat-generation classified (see Figure 2.10) [10]. The contribution of the heat-generating waste to the total volume is quite low, while it contains most of the radioactivity. The waste with negligible heat-generation is about 95 % of the volume, but contains one percent of the radioactivity only.

Once through fuel cycle As already mentioned, one possibility to handle radioactive waste is the direct disposal in deep geological formations. The spent fuel is taken out of the reactor and given into a spent fuel storage pool at the power plant. It stays there until the generation of heat reaches one-hundredth of the original value, which is reached after several years.

After this decay time, the fuel assembly is given into a transport container and shipped into an interim storage, to further remove decay heat. Afterwards it is mechanically decomposed into fuel rod and structure material. The fuel rods are packed into final storage containers without any conditioning, those are inserted into deep geological formations for the final storage.

Closed fuel cycle The reprocessing of spent fuel makes a reuse as **m**ixed **ox**ide (MOX) fuel possible. For that purpose the spent fuel is also given into a spent fuel storage pool at the power plant. Afterwards it is transported to a reprocessing plant (e. g. La Hague or Sellafield for Europe), where the fuel element is disassembled and the fuel rods are dissolved in nitric acid (HNO_3). This solution contains the fission and activation products as well as the not fissioned fuel and is further

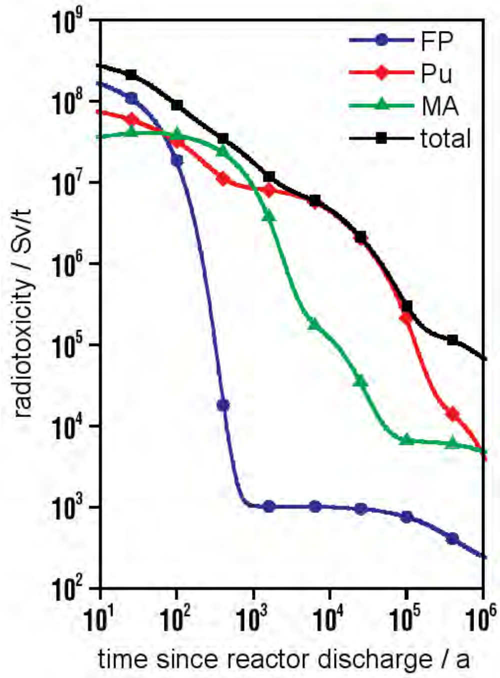

Figure 2.9.: Radiotoxicity of spent fuel in dependency of time [9].

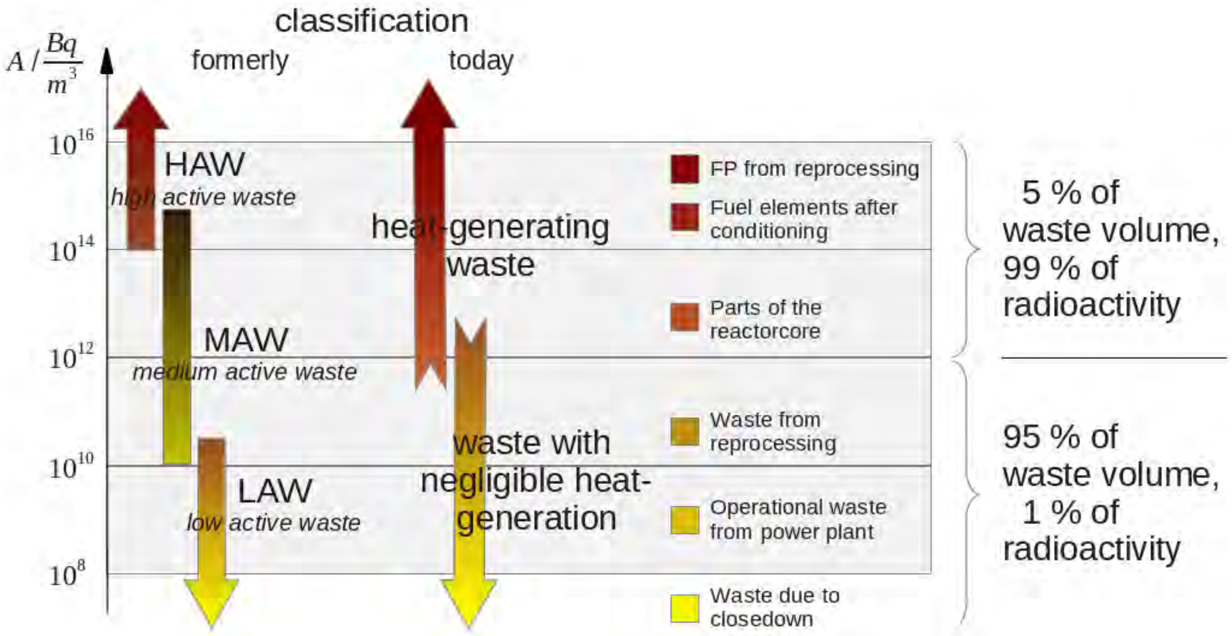

Figure 2.10.: Classification of racioactive waste [10].

on treated chemically. The uranium and plutonium are separated by a liquid-liquid extraction process, which is called PUREX (**p**lutonium and **u**ranium **r**efining by **ex**traction).

After the dissolution of the fuel rods, sodium nitrite ($NaNO_2$) is added to the solution. It acts as a reducing agent to generate plutonium ions in the oxidation state +IV. Afterwards, an extraction from this 2-3 $\frac{mol}{L}$ nitric solution according to equation (2.6) and (2.7) takes place. The extractant used is "tri-butylphosphate" (TBP) dissolved in kerosene. This ester is able to complex actinide metal ions which are in the oxidation state +IV or +VI.

$$\mathrm{UO_2{}^{2+} + 2\,NO_3{}^{-} + 2\,TBP \rightleftharpoons UO_2(NO_3)_2(TBP)_2} \tag{2.6}$$

$$\mathrm{Pu^{4+} + 4\,NO_3{}^{-} + 2\,TBP \rightleftharpoons Pu(NO_3)_4(TBP)_2} \tag{2.7}$$

In a further step the plutonium is reduced to +III and a back-extracted to the aqueous phase. The uranium stays dissolved as TBP-complex in the organic phase. Then a back-extraction with diluted nitric acid takes place. The fission products and the minor actinides remain in the PUREX raffinate. Currently this raffinate is vitrified and disposed as high active waste (HAW) [3].

Advanced closed fuel cycle Another opportunity for the handling of radioactive waste is the closed fuel cycle, which can be achieved by the so called **p**artitioning and **t**ransmutation (P&T) strategy. Partitioning describes the separation of long lived radiotoxic isotopes. Transmutation is the burn up of these radionuclides with fast reactors or accelerator driven systems [11].

The influence of actinides on the spent fuels radiotoxicity was already demonstrated in Figure 2.9. It takes a time of 170×10^3 years to reach the radiotoxicity of the amount natural uranium, needed to produce 1 ton of fuel, for the waste excluding any treatment. This time decreases by a factor of 10 (16×10^3 a) due to U and Pu separation like its done in the previously explained PUREX process. A further separation of the MA would decrease this time more significantly. With a separation factor of 99.9 % a time of 330 a could be achieved to reach the reference radiotoxicity. So one can conclude that the partitioning and transmutation of plutonium and minor actinides would lead to a significant reduction of the long-term radiotoxicity. The long-lived fission products are, due to their low proportion of long-term radiotoxicity, and their low long-term heat generation of minor interest [9].

2.4. State of the scientific and technical knowledge

The work done in this thesis contributes to the ASGARD project, under the Seventh Euratom Framework Programme for Nuclear Research and Training Activities (FP7 Euratom).

ASGARD is an acronym standing for ***a**dvanced fuel**s** for **G**eneration IV re**a**ctors: **r**eprocessing and **d**issolution*. The project is focusing on research of advanced, innovative nuclear fuel fabrication and their respective reprocessing issues for Generation IV reactors, it is coordinated by Chalmers Technical University and 16 institutions from 9 European countries are involved. The Generation IV reactor class is defined in the following paragraph.

Generation IV reactors The generation IV reactors are a series of theoretical reactor designs that are being investigated presently. An implementation for commercial purposes is not expected before 2030. Research in these technologies was officially started by the Generation IV International Forum (GIF), which was launched in 2000 and established in 2001 by nine countries (Argentina, Brazil, Canada, France, Japan, South Korea, South Africa, the United Kingdom and the United States) under the aegis of the United States. During the further process China, the European Union, Russia and Switzerland joined this project. Five goals are the target of this research, in terms of sustainability, safety & reliability, economics and proliferation resistance and physical protection. After a development phase of 2 years, 6 reactor designs are the most favored, three of these designs are fast reactors and interesting for transmutation purposes:

- Gas-cooled fast reactor (GFR),
- Lead-cooled fast reactor (LFR),
- Sodium-cooled fast reactor (SFR).

2.4.1. Fuel fabrication

With regard to the Generation IV reactors and requirements for effective transmutation, advanced concepts for fuel production are necessary. The common powder technique has already been described in section *Nuclear fuel cycle* on page 10. For fast reactors, particle fuels show good properties and is described more detailed further on.

Particle fuel Advanced fuel concepts replace the pellets by particles (*Sphere pac* or *Vipac* fuel) [12]. Particle fuels show good swelling behavior and spherical particles, which are used for sphere pac fuels, can be fabricated dustless with a wet chemical method. A scheme of a sphere pac fuel and a fuel rod, fabricated by conventional pellet methods is shown in Figure 2.11. The shown sphere pac fuel consists of spheres belonging to two different size fractions.

A further advantage of particle fuel is power savings during fuel production. There is no need for any mechanical treatment of the fabricated particles, they can be directly inserted into the fuel pin. The fabrication of the mentioned Vipac fuel is a dry route and starts with a pyrochemical process. Spent fuel is dissolved in a molten salt and electrolyzed. The MOX, depositing at the electrode, is

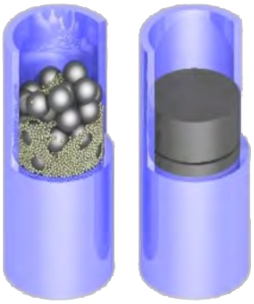

Figure 2.11.: Scheme of a sphere pac fuel in comparison to conventional pellet fuel [13].

further on crushed, milled and sieved into 3–7 size fractions. Afterwards a feeding into fuel rods takes place. Vipac fuel has been developed for fast systems, but studies for thermal systems has also been investigated [12].

Sol gel processes

Sphere pac fuel can be achieved by several techniques, quite common wet chemical routes are sol gel methods. This synthesis strategy transforms an aqueous colloidal solution "sol" into a solid "gel".

From a chemical point of view, a gel can be presented as a polymer. During the gelation process, bridges between the molecules are formed, similar to a polymerization. Industrially relevant are the *external gelation*, and the *internal gelation* method.

An overview about the common techniques is given in the following paragraphs. The internal gelation method was used for the particle synthesis during this work and is described more in detail in the next subsection. An advantage of these technique is that a co-processing of different metals is possible. Furthermore, a wide range of sphere sizes can be fabricated and the technique is capable for non oxide ceramics (nitride, carbide) [14].

2.4.1.1. External gelation

One of the widest used sol gel processes in the production of nuclear fuels was studied in Jülich [15] and was used to fabricate fuel kernels for the German gas-cooled reactor *AVR* (Arbeitsgemeinschaft Versuchsreaktor). The so called *TRISO* (Tristructural-isotropic) fuel-kernels were synthesized by an external gelation fabrication route. Long time experience showed that this process is usable to produce high quality UO_2 microspheres. An industrial scale with a production of about 400 kg UO_2 spheres for AVR fuel was achieved [16].

The external gelation process bases on a sol containing $UO_2(NO_3)_2$, an organic polymer (e.g. polyvinyl alcohol) and a modifier agent. For this purpose *tetrahydrofurfuryl alcohol* (THFA) is a common substance. The solution is given dropwise through a vibrating nozzle into an ammonia solution. A mass transfer of the ammonia into the droplet takes place and causes the precipitation of the uranyl nitrate as ammonium diuranate. After a certain aging time, the particles are washed with water or low concentrated ammonia solutions. A further washing step with organic substances follows to remove residual humidity of the gels. The green bodies are dried and calcinated at a temperature range of 400-600 °C, then sintered in reducing H_2:Ar atmosphere at 1600-1700 °C leading to the UO_2 microspheres [17].

Total gelation The *total gelation* is a further strategy, based on an external gelation. The benefits of an internal gelation are implemented, but without the disadvantage of silicon oil as heat carrier. Good products with a high sphericity were fabricated, when applying this method [18].

Water extraction Another technique is the *water extraction*, a sol is given dropwise into organic alcohols, which removes water from the sol and leads to the gelification. The resulting precipitated particles are free of organic impurities.

Hydrolysis of metal-alkoxides A further method, mainly used to fabricate high purity Ti or Si ceramics, is the *hydrolysis of metal-alkoxides.* The sol contains $M(\mathrm{O}R)_x$ (with $M = \mathrm{Ti}, \mathrm{Si}$ & $R = \mathrm{C_2H_5}, \mathrm{C_3H_7}, \mathrm{C_4H_9}$) and is given into water. Using this method, narrow particle size distribution is reached.

2.4.1.2. Internal gelation

During the 1970s nuclear fuel research in Jülich was not only focused on the external gelation process. The KEMA process developed in the Netherlands [19] was adapted and further improved. In contrast to external gelation, the sol for internal gelation processes already contains the gelification agent. Hexamethylenetetramine (HMTA) and urea are used for this purpose. When HMTA undergoes a temperature increase, it decomposes to ammonia. The resulting pH increase in the sol induces the gelation. The temperature increase takes place by extruding droplets of the cooled sol to a temperated water immiscible medium. Common substances are paraffin and several silicone oils.

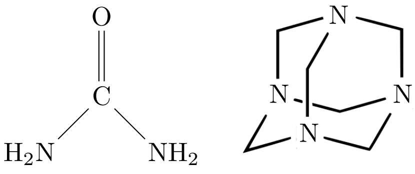

(a) urea **(b)** HMTA

Figure 2.12.: The gelification agents urea and HMTA.

A fabrication process developed in Jülich according to Förthmann [20] is shown in Figure 2.13. The precursor solution is cooled until it is given dropwise into the gelation column. The temperated oil, which is used as heat carrier to induce the gelation, is recirculated. The particles formed are collected in a flask [21]. In contrast to the originally developed KEMA process for the synthesis of uranium microspheres by internal gelation, Förthmann added the gelification agents in solid form to the precursor solution, while the original route used dissolved gelification substances. A comparison of both preparation processes is shown schematically in Figure 2.14.

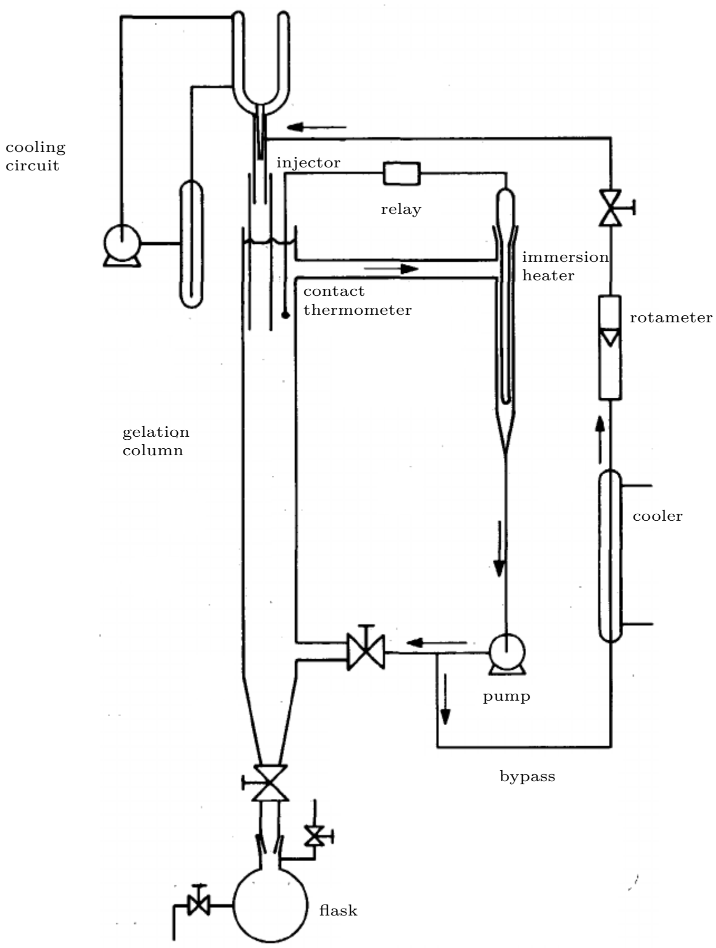

Figure 2.13.: Scheme of an internal gelation process according to Förthmann [20].

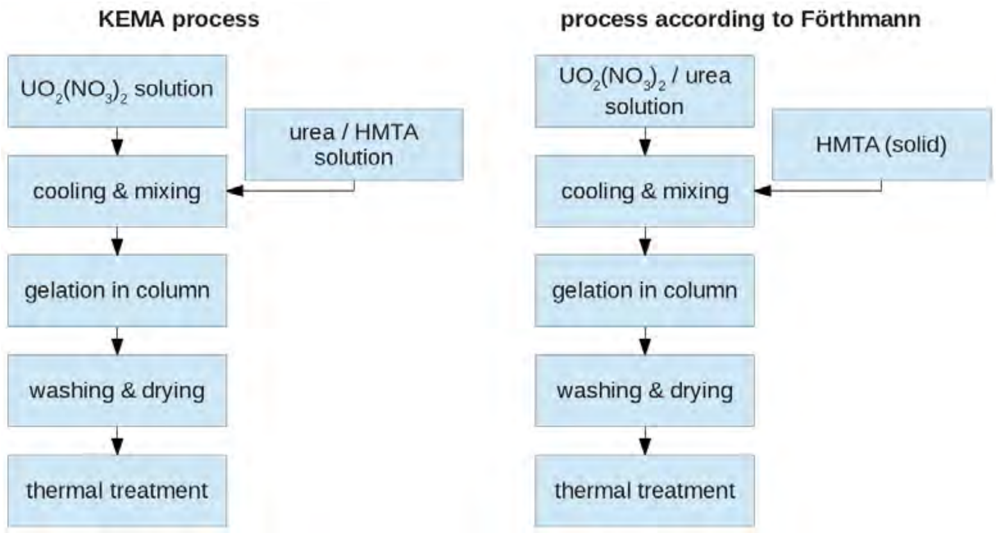

Figure 2.14.: Flow chart comparison of the KEMA process [19] and the process according to [20].

Several basic investigations on the chemical principle of the internal gelation method are discussed in literature. According to Collins et al. [22] and Vaidya [14] the cooling during the sol preparation prevents the uranyl ion from hydrolysis. An uranyl urea complex ($UO_2[CO(NH_2)_2]_2^{2+}$) is formed. At increased temperature this complex and HMTA decompose. The resulting pH increase leads to gelification of the sol. The process for U is shown in the reactions (2.8) to (2.12).

$$UO_2^{2+} + 2\,CO(NH_2)_2 \rightleftharpoons UO_2[CO(NH_2)_2]_2^{2+} \tag{2.8}$$

$$(CH_2)_6N_4 + H^+ \rightleftharpoons (CH_2)_6N_4H^+ \tag{2.9}$$

$$(CH_2)_6N_4H^+ + 6\,H_2O + 3\,H^+ \longrightarrow 4\,NH_4^+ + 6\,CH_2O \tag{2.10}$$

$$UO_2^{2+} + 2\,H_2O \rightleftharpoons UO_2(OH)_2 + 2\,H^+ \tag{2.11}$$

$$UO_2(OH)_2 + 2\,H_2O \longrightarrow UO_3 \cdot 2\,H_2O\downarrow \tag{2.12}$$

Acid deficient uranyl nitrate

Common starting solutions for many conversion processes are **a**cid **d**eficient **u**ranyl **n**itrate (ADUN) solutions. An ADUN solution has a higher stoichiometric amount of uranyl ions than NO_3^- ions.

Normally the ratio of uranyl ions to nitrate ions is one to two (1 : 2). During the dissolution of uranyl nitrate, protons are released which cause a higher acid concentration in the solution. The hydrolysis reaction according to equation (2.13) describes this process.

$$UO_2(NO_3)_2 + H_2O \longrightarrow UO_2(OH)^+ + 2\,NO_3^- + H^+ \tag{2.13}$$

This reaction reveals the formation of nitric acid, dissociated in NO_3^- and H^+ ions. A change in the ratio nitrate ion to uranyl ion achieves a prehydrolyzed stock solution. Such an ADUN solution can contain uranium concentrations of $c(\mathrm{U}) \approx 3.0\,\frac{\mathrm{mol}}{\mathrm{L}}$ without precipitation of solids. The pH values of such a solution can reach approximately 2, while the pH value of a saturated stoichiometric uranyl nitrate solution ($c(\mathrm{U}) = 2.1\,\frac{\mathrm{mol}}{\mathrm{L}}$) is about 0.3. A further advantage of an ADUN solution is that less HMTA and urea are needed for an internal gelation process.

Such a solution can be produced by many synthesis routes. Preparation by solvent extraction [23] or dissolution of uranium trioxide in aqueous solution of uranyl nitrate [24] are common ways.

2.5. Measurement technique

2.5.1. Inductively Coupled Plasma Mass Spectrometry

Inductively **c**oupled **p**lasma **m**ass **S**pectrometry (ICP-MS) is a method to analyze different inorganic elements. It is quite common in applications to perform qualitative and quantitative element analysis.

An aqueous sample is nebulized into a spray chamber to form an aerosol. Small droplets of this aerosol are introduced into an Ar plasma with temperatures of approximately 6000 °C. Under this conditions the sample is dried,vaporized, atomized and ionized. The plasma is achieved by a radiofrequency coil, that is wrapped around the so called plasma torch. The coil is supplied by a high frequency generator. The ions then pass into the vacuum system of the following mass spectrometer part of the device. The ions are separated according to their mass to charge ratio ($\frac{m}{z}$) by the use of a quadrupole magnet and detected by a secondary electron multiplier.

Since this method is very sensitive, it is used in trace analysis. It is possible to determine many elements in a short time simultaneously. Furthermore, the ICP-MS is used to determine isotope ratios.

2.5.2. Thermogravimetric analysis

Thermo**g**ravimetry (TG) describe the detection of change in mass of a sample as function of temperature and time, with a so-called thermobalance. The sample is introduced into a crucible (for example Al_2O_3 or Pt) and placed into a furnace, coupled to a scale which registers the mass changes during a defined temperature program.

Differential **s**canning **c**alorimetry (DSC) is a method to determine the required or released heat energy of a sample. Therefore the temperature difference between a sample and a reference sample is measured at a defined temperature program. The physical properties determined in this way of the sample are plotted as function of temperature. Exothermic reactions of the sample are indicated by a rising temperature difference, while endothermic reaction decrease in the temperature difference.

By coupling of TG and DSC, it is possible to analyze phase transitions in the sample material and investigate its thermal behavior.

2.5.3. Scanning electron microscope

The aim of the **S**canning **e**lectron **m**icroscope (SEM) investigations is the morphological characterization of the samples. Furthermore, chemical analysis of the samples in terms of qualitative and semi-quantitative can be performed.

In contrast to an ordinary light microscope, the scanning electron microscope is not generating a direct image. With the aid of a cathode, an electron beam is generated, which is collected and focused, before the sample is scanned. The electrons can be scattered elastically or inelastically and be analyzed with appropriate detectors, when impinging on the specimen surface. Thus, interactions of the sample material with the electron produce an image.

The backscattered electrons are analyzed in the backscattered electron detector. The backscatter coefficient depends on the atomic number of the material. In heavy elements a strong backscattering let this area appear bright. Based on the backscattered electrons a material contrast image can be obtained. Inelastically scattered electrons release some of their kinetic energy by interactions with the sample material. The secondary electrons resulting from the interaction in the superficial layers, can be visualized with a Large Field Detector. This resulting image represents the surface topography.

From the interaction of the electron beam with the specimen result X-rays, which can be analyzed using an **E**nergy-**d**ispersive **X**-ray spectroscopy (EDX) detector. From the recorded X-ray spectrum, the chemical composition of the sample, can be determined.

Furthermore, the **e**vironmental **s**canning **e**lectron **m**icroscope (ESEM) mode enables to investigate samples under varying climatic conditions during the measurement.

2.5.4. X-ray powder diffraction

X-**r**ay powder **d**iffraction (XRD) is used to investigate the long-range order phenomena of a material from which the crystal structure is derived. It can be used to perform a qualitative and a quantitative phase analysis. In powder diffraction, monochromatic X-rays are used. The sample is irradiated with the monochromatic beam at the incident angle Θ, as schematically shown in Figure 2.15.

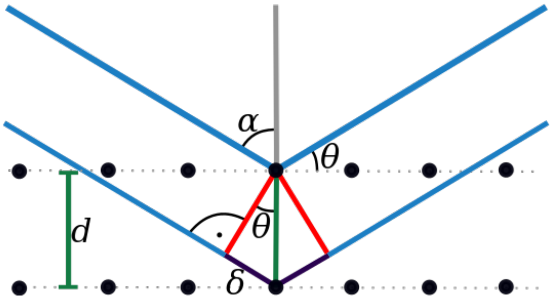

Figure 2.15.: Bragg-reflection at crystal lattice [25].

When the beam is scattered by an atom, a reflex for the diffraction pattern is produced. Constructive interference occurs only when the path of the reflected beams differs by an integer multiple of the wavelength. This condition is expressed in the Bragg equation, shown as (2.14).

$$n\lambda = 2d\sin\Theta \tag{2.14}$$

The wavelength of the X-rays is symbolized by λ, n is a natural number indicating the order of diffraction, while the lattice spacing is expressed by d and Θ is the Bragg angle. A charge-coupled-device (CCD) detector records the reflections of the respective intensity, so that the intensity can be plotted as function of the diffraction angle 2Θ.

2.6. Scope of work

The aim of this thesis was the preparation of uranium based microspheres, which can be used as particles for innovative nuclear fuel fabrication, by the synthesis route of an internal gelation. This dustless particle generation process should be able to be applied for co-conversion. For this purpose, neodymium is used as surrogate for trivalent actinides.

Spherical particles containing a UO_2 matrix and different portions of Nd should be prepared, with a Nd content up to 40 %. Moreover a control group of equal U / Nd compositions should be prepared by common powder route.

A characterization of the fabricated products should be performed, including detailed X-ray diffraction analysis and SEM investigations. A comparison of the lattice structure belonging to the particles and powders has to be carried out.

3. Experimental part

Spherical U / Nd oxide particles with different neodymium contents were prepared. Compositions with Nd contents in a range of 0-40 % with an increment of 5 % were synthesized by internal gelation, whereas Nd was used as surrogate for trivalent actinides, such as americium. The Nd mole fraction is expressed as $\chi(\mathrm{Nd})$, which is defined in equation (3.1), n symbolizes the amount of substance.

$$\chi(\mathrm{Nd}) = \frac{n(\mathrm{Nd})}{n(\mathrm{Nd}) + n(\mathrm{U})} \tag{3.1}$$

3.1. Preparation of microspheres

The general principal of internal gelation is described in section 2.4.1.2 on page 17. The important steps of the fabrication are summarized in Figure 3.1. The prepared sol is dropped into a column containing silicon oil with a temperature of 90 °C. After cooling down to room temperature, the particles are washed and transfered into an ammonia solution. After aging and further washing steps, the particles are dried at air and finally thermal treated. The following subsections describe this procedure in detail.

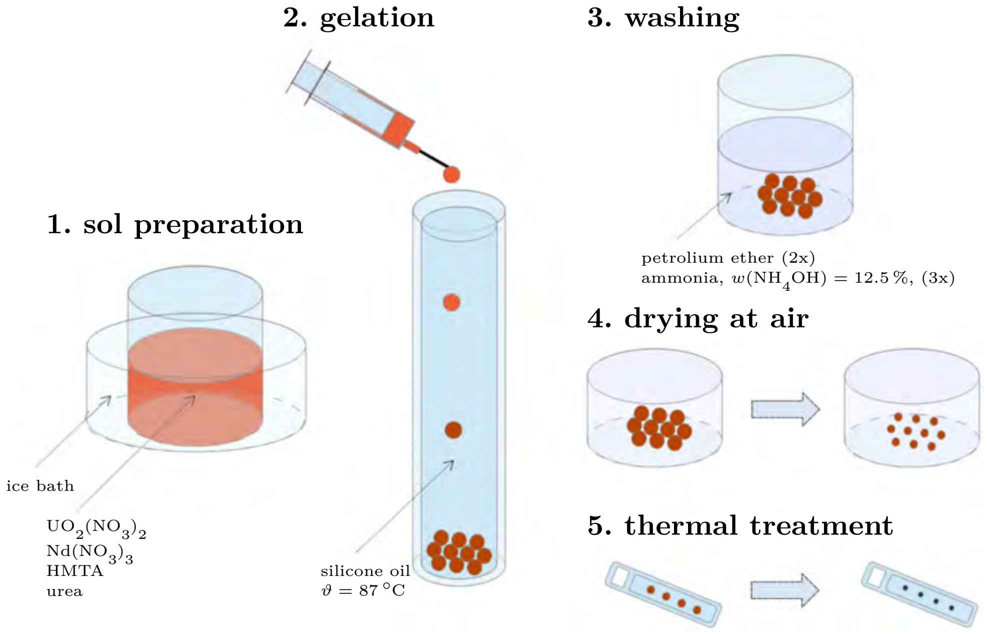

Figure 3.1.: Schematic overview of the microsphere fabrication process by internal gelation.

3.1.1. Preparation of precursors

$UO_2(NO_3)_2$-solution As precursor, a saturated $UO_2(NO_3)_2 \cdot 6\,H_2O$ solution with approximately $c(UO_2(NO_3)_2) = 2.1\,\frac{mol}{L}$ was used. It was generated by weighing the specific amount of $UO_2(NO_3)_2 \cdot 6\,H_2O$ into a volumetric flask, which was filled up with ultrapure water. A clear yellow solution was generated by shaking and the U mass concentration was determined by ICP-MS ($1 : 10^7$ dilution, matrix: ultrapure water / HNO_3).

ADUN An ADUN solution was used as feed solution and fabricated by the dissolution of uranium trioxide in a saturated solution of uranyl nitrate [24]. The required UO_3 was synthesized by thermal decomposition of $UO_2(NO_3)_2 \cdot 6\,H_2O$ according to Wheeler et al. [26].

- A mass of approximately 5 g $UO_2(NO_3)_2 \cdot 6\,H_2O$ was weighed into a crucible and heated up to 400 °C. A furnance (*Heraeus*) combined with a temperature control unit (*Horst, "HT-30"*) was used to perform this treatment. The temperature was kept for one hour. A red powder was produced and XRD analyses of the resulting powder were performed.

- The dissolution of the UO_3 powder provides the advantage to be proton consuming as well, compare equation (3.2). The quantity to achieve a U concentration of $3\,\frac{mol}{L}$ was calculated. The specific amount of UO_3 was weighed into a weighing funnel and added to the already characterized $UO_2(NO_3)_2$ solution. The mixture was stirred for 1–3 days kept at $\vartheta = 70\,°C$ in an oil bath.

$$UO_3 + 2\,H^+ \longrightarrow {UO_2}^{2+} + H_2O \tag{3.2}$$

- A formation of hydroxides during the dissolution according to equation (3.3) and (3.4) could explain that after one week of stirring at 70 °C no clear solution was achieved. The suspension was centrifuged (*Heraeus, "Multifuge 3+"*) and decanted. Afterwards, the U content was determined by ICP-MS ($1 : 10^7$ dilution, matrix: ultrapure water / HNO_3) and the ${NO_3}^-$ content by photometric analysis ($1 : 10^4$ dilution, Nitrate test kit: *Dr. Lange "LCK 339"*).

$$UO_3 + 3\,{UO_2}^{2+} + H_2O \longrightarrow 2\,[(UO_2)_2(OH)]^{3+} \tag{3.3}$$

$$UO_3 + {UO_2}^{2+} + H_2O \longrightarrow [(UO_2)_2(OH)]^{2+} \tag{3.4}$$

$Nd(NO_3)_3$-solution A neodymium solution with a concentration of $c(\mathrm{Nd(NO_3)_3}) = 2.98\,\frac{\mathrm{mol}}{\mathrm{L}}$ was used to produce the particles. It was produced by weighing a specific amount of $Nd(NO_3)_3 \cdot 6\ H_2O$ into a volumetric flask, which was filled up with ultrapure water. A clear violet solution was generated by shaking, the Nd content was determined by ICP-MS ($1 : 10^7$ dilution, matrix: ultrapure water / HNO_3).

3.1.2. Preparation of sol

The amount of the organic gelation agents urea and HMTA, which were used for the synthesis of the microspheres is defined by their ratio to the total metal concentration according to the equations shown in equation (3.5) and (3.6).

$$R(\mathrm{urea}) = \frac{n(\mathrm{urea})}{n(M^{n+})} \tag{3.5}$$

$$R(\mathrm{HMTA}) = \frac{n(\mathrm{HMTA})}{n(M^{n+})} \tag{3.6}$$

The internal gelation was done according to Daniels et al. [27] and the amount of urea ($R(\mathrm{urea}) = 1.8$) was adapted. In the before mentioned work particles with a constant Nd content of 10 % were prepared.

In previous experiments it could be figured out that for higher Nd contents less HMTA is needed. Therefore $R(\mathrm{HMTA}) = 1.35$ was used to perform the internal gelation in this work. The parameters $R(\mathrm{urea})$ and $R(\mathrm{HMTA})$ were kept constant for all particle fractions independent of their Nd content.

The sol was prepared by weighing the amount of urea into a vial and cooling it in an ice bath on a magnetic stirrer. Afterwards the specific volumes of $Nd(NO_3)_3$ solution and ADUN solution were added with a pipette. Then the amount of HMTA, weighed in into a weighing funnel, was given to the cooled vial. After stirring a while the sol was ready for gelation and stable in the ice bath. A volume of approximately 2 mL was produced.

3.1.3. Gelation and washing

Approximately half of the produced volume (1 mL) was taken into a 2 mL syringe and dropped into a double-walled column filled with silicone oil. The heating jacket of the column was heated by a temperature control device to $\vartheta = 90\,°\mathrm{C}$ (inside: $\vartheta = 87\,°\mathrm{C}$). The used gelation column is shown in Figure 3.2.

Figure 3.2.: Double-walled gelation column, filled with silicone oil.

When the addition of the sol to the column was completed the temperature control device was switched off. When the column achieves room temperature, the microspheres were transferred to a beaker with the help of a PTFE sieve as shown in Figure 3.3, (a). Afterwards the particles were washed with a volume of 100 mL petroleum ether 3 times, to remove residues of the silicone oil. A photograph of the washed particles is shown in Figure 3.3, (b). Then a volume of 100 mL NH_4OH ($w = 12.5\,\%$) was added.

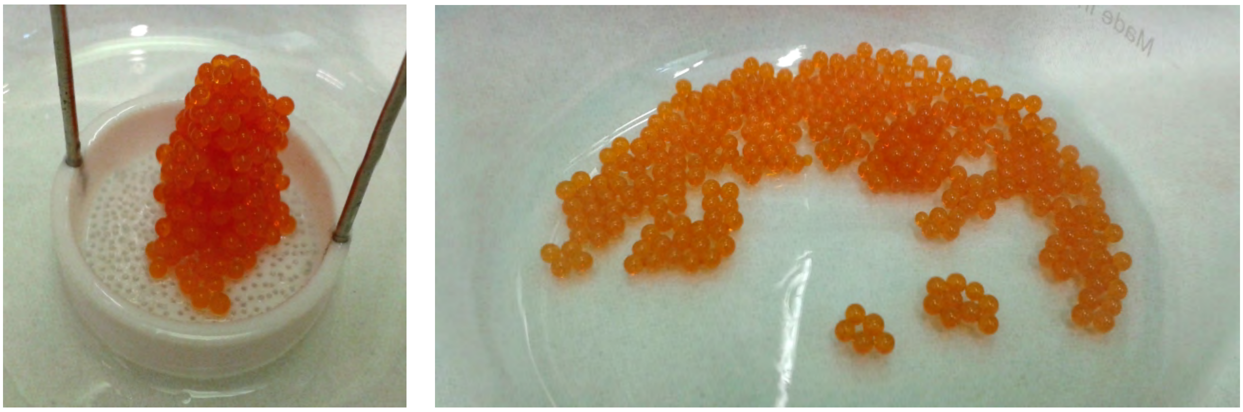

(a) before washing

(b) after washing

Figure 3.3.: Washing of fabricated U / Nd microspheres ($\chi(\mathrm{Nd}) = 5.80\,\%$).

After an aging of 24 hours the microspheres were washed twice with NH_4OH ($w = 12.5\,\%$). Samples of the aging water and the washing waters were taken and analyzed by ICP-MS to estimate the Nd and U losses during the washing steps. The particles were transferred to a petri dish, half covered with a glass to prevent dust contamination, where they were dried for two days at room temperature. Photographs of the microspheres before and after drying are shown in Figure 3.4.

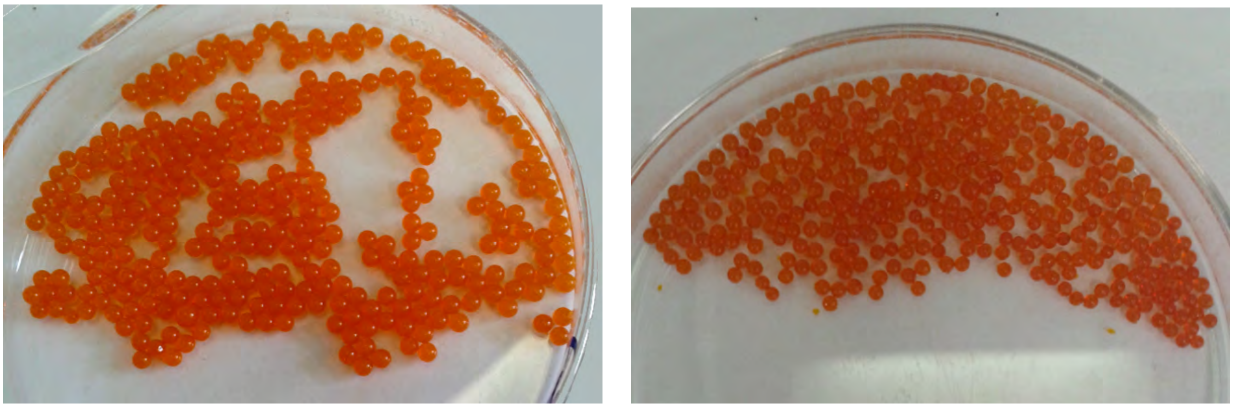

(a) before drying **(b)** after drying

Figure 3.4.: Drying of fabricated U / Nd microspheres ($\chi(\text{Nd}) = 11.99\,\%$).

Furthermore, ICP-MS analyses of the green bodies were done. Therefore 2 microspheres of each composition (approx. 10 mg) were dissolved in 1 mL HNO_3 (65 % ultrapure) and a volume of 9 mL matrix solution (ultrapure water / HNO_3) was added, the mixture was shaken well. A 1 : 1000 dilution of this mixture was prepared, which was further diluted by 1 : 100. The last step was repeated once more to generate a 1 : 10^7 dilution which was measured by ICP-MS to determine the Nd and U content.

3.1.4. Thermal treatment

Thermal treatment of the raw particles was carried out in air and in a reducing H_2:Ar (4:96) atmosphere. Particles of each fraction were weighed into crucibles, placed in a high temperature furnace (*Linn High Therm*, *HT1800*) and heated up to 1300 °C with $3\,\frac{°\text{C}}{\text{min}}$ according to the temperature program in Figure 3.5. During the treatment in reducing atmosphere, a H_2:Ar gas flow of $1.2\,\frac{\text{L}}{\text{min}}$ was kept. Further investigations were done with microspheres heated up to a maximum temperature of 1600 °C, which was held for 5 hours. The same temperature gradient as mentioned before ($3\,\frac{°\text{C}}{\text{min}}$) was used. This temperature program is also plotted in Figure 3.5.

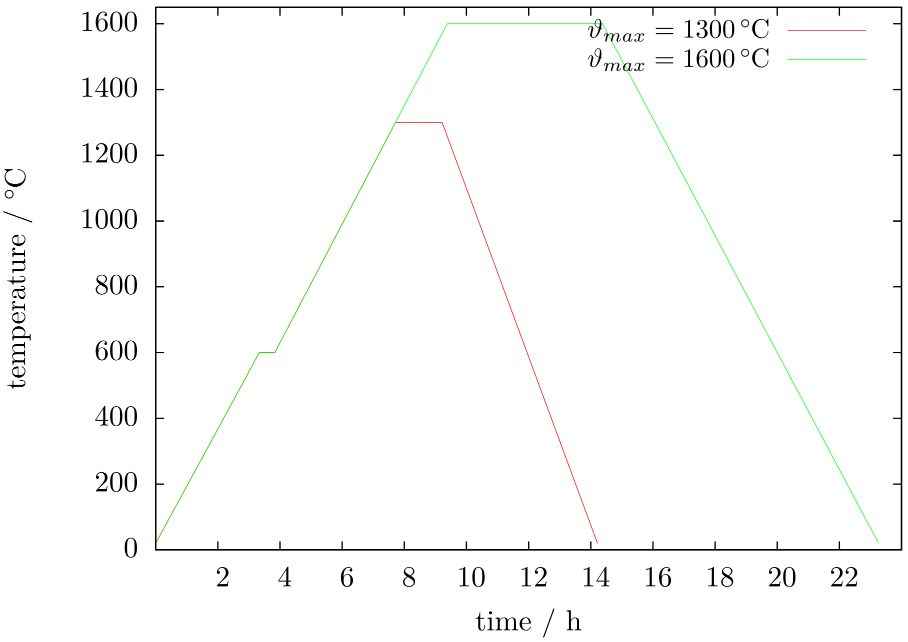

Figure 3.5.: Temperature program used for thermal treatment of microspheres.

3.2. Control group

3.2.1. Preparation of powders

Powders of oxidic U and Nd mixtures with the same $\chi(\mathrm{Nd})$ contents as the particles were also synthesized ($\chi(\mathrm{Nd}) = 5 - 40\,\%$ with an increment of $5\,\%$). The preparation was done by thermal denitration, the powders act as control group for the prepared microspheres, which was due to a gap in the presence of XRD data dealing with Nd / U solid solutions reasonable.

Stock solution Stock solutions with a metal concentration of $1\,\frac{\mathrm{mol}}{\mathrm{L}}$ were used as precursors. They were prepared by weighing $\mathrm{UO_2(NO_3)_2 \cdot 6\,H_2O}$ and $\mathrm{Nd(NO_3)_3 \cdot 6\,H_2O}$ into volumetric flasks. Ultrapure water was added and clear solutions were produced by shaking. Samples for ICP-MS analysis were taken to determine the precise U and Nd content in the initial solutions.

Evaporation Corresponding volumes of the stock solutions were pipetted into a beaker and heated with a magnetic stirrer. As example, the mixtures containing $\chi(\mathrm{Nd}) = 25 - 40\,\%$, are shown during evaporation in Figure 3.6. The left beaker at the bottom contains the $\chi(\mathrm{Nd}) = 25\,\%$ mixture, while the $\chi(\mathrm{Nd}) = 40\,\%$ powder is in the right beaker on the top.

Thermal treatment The dried powders were further treated in two steps. First they were calcined in air. A temperature program according to Figure 3.7 was used. Afterwards, the powders were treated in a reducing $\mathrm{H_2}$:Ar atmosphere at a maximum temperature of 1300 °C. The same temperature program (Figure 3.5) as for the microspheres was used.

Figure 3.6.: Evaporation of $UO_2(NO_3)_2$ / $Nd(NO_3)_3$ solution mixtures on a magnetic stirrer.

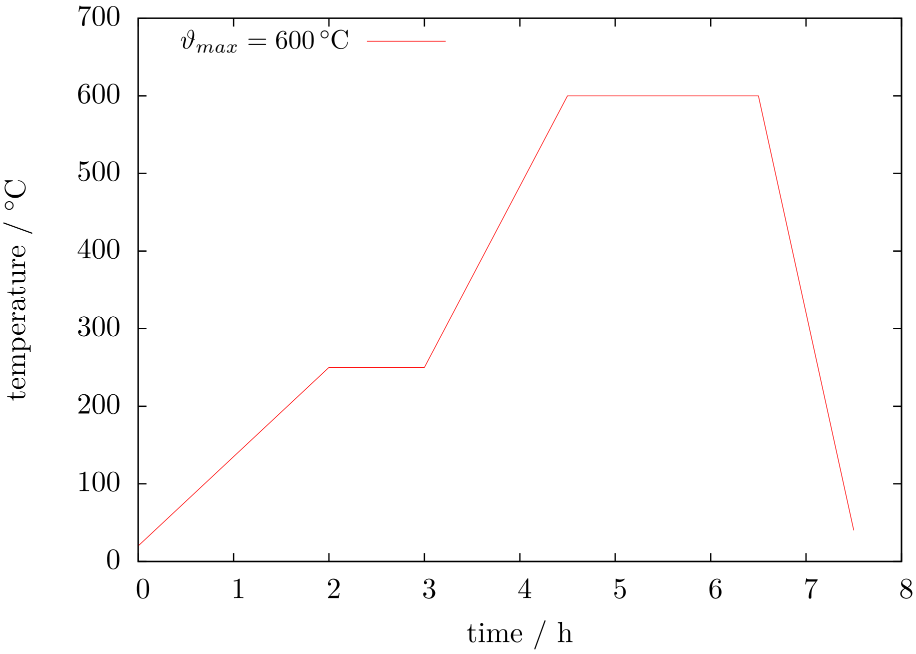

Figure 3.7.: Temperature program used for the calcination of U / Nd oxide powders in air at 600 °C.

3.3. Characterization methods

3.3.1. ICP-MS

All ICP-MS analyses were performed with the device *Elan 6100 DRC* by *PerkinElmer/SCIEX*. The system was calibrated with 0.1 ppb, 1 ppb, 10 ppb and 100 ppb U / Nd solutions, prepared by diluting certified 10 ppm single element standards. A solution containing ultrapure water and HNO_3 (1 % V/V) was used as dilution matrix.

- Two microspheres of each fraction were dissolved in 1 mL concentrated HNO_3. A volume of 9 mL matrix solution was added and the samples were further diluted $1 : 10^7$, then the measurement took place. The determined mass concentrations $\beta(\mathrm{U})$ and $\beta(\mathrm{Nd})$ were transformed to molar concentrations c, which were used to calculate $\chi(\mathrm{Nd})$.

3.3.2. Optical microscope

The microspheres were characterized by determining the diameter (d) and mass (m), which were used to calculate the particle volume (V) and its density (ρ).

- The mass of 30 microspheres (dried at air), of each fraction, was determined.
- Each weighed particle was analyzed by the use of an optical microscope (*Zeiss*, *Axiotech*) (compare fig. 3.8). A photography of each microsphere was taken with a magnification of 50. Moreover, a 10 mm standard was recorded.

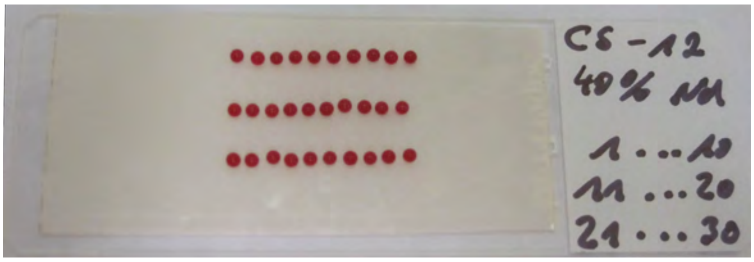

Figure 3.8.: Microspheres prepared for optical microscope investigations.

- The images of the spheres of each composition and the corresponding standard were added to a composite image as shown in Figure 3.9. The in this way generated composite images were analyzed with the software ImageJ (Version: "1.46 r"), provided by the US *National Institutes of Health*. By using the standard characteristic particle parameters e. g. surface area and diameters were determined. As example particles with $\chi(\mathrm{Nd}) = 42.63\,\%$ are shown in Figure 3.9.

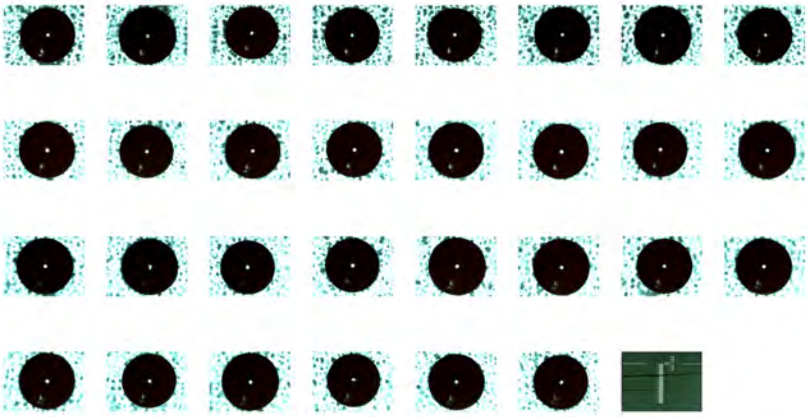

Figure 3.9.: Composite image for ImageJ particle analyses (χ(Nd) = 42.63 %).

3.3.3. SEM/EDX

SEM/EDX analyses (*FEI*, *Quanta 200F*) were performed to investigate the shape, morphology and homogenity of the prepared U / Nd microspheres. Therefore, size measurements were done and the chemical composition was investigated by EDX, using an *EDAX Genesis 4000* system. Three microspheres of each composition were glued onto a conductive carbon tab, mounted on an aluminum specimen holder (compare Figure 3.10). The analysis were performed in a low vacuum mode with a pressure of 60 Pa, to avoid artifacts due to sputtering on a conductive layer. A working distance of 10 mm was chosen and the analyses were performed with a current of 7-20 kV.

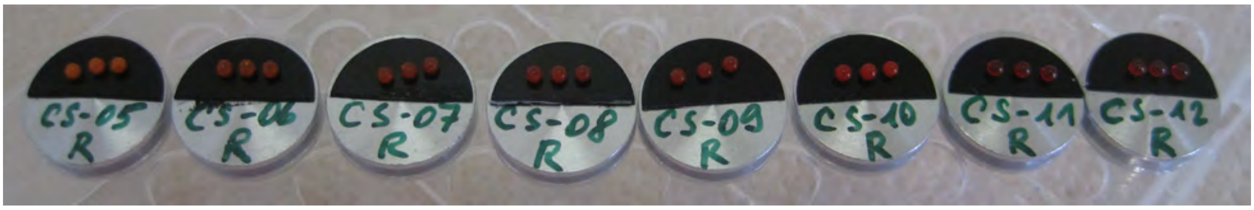

Figure 3.10.: Microspheres prepared for SEM/EDX investigations.

- Size measurements were done with images, recorded with a magnification of 150 x. The diameter in four positions of a microsphere, as shown in image (a) of Figure 3.11, was measured. Three microspheres of each batch were analyzed and the average batch diameter was generated.
- The EDX investigations to determine the homogeneity and chemical composition, were also performed at the SEM parameters. A square area was marked on the surface of each particle (magnification of 150 x), in that way that the squares corners are attached to the perimeter of the sphere (compare image (b), fig. 3.11). Then the measurement for 50 live seconds was started. These measurements are only semi-quantitative and the measurement conditions as

well as the sample geometry can cause large deviations. Again three particles per fraction were analyzed and an average $\chi(Nd)$ content was calculated.

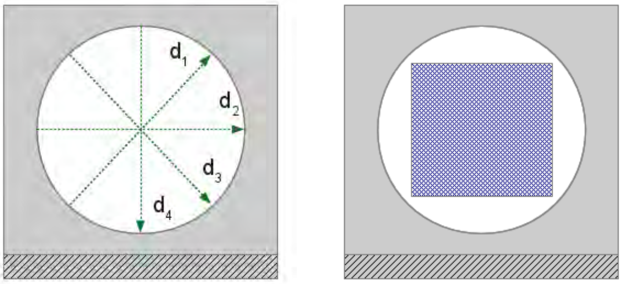

(a) SEM *d* measurements **(b)** EDX analysis

Figure 3.11.: SEM/EDX investigations.

Environmental scanning electron microscope (ESEM) observations were performed to explain the cracks on the surface of the untreated microspheres.

- The sample was mounted on a temperature-controllable sample plate and 4 drops of water were added to the temperating system (compare fig. 3.12). The chamber was closed and the sample was cooled to 5 °C. A humidity of 97.0 % and a pressure of 850 Pa was established. The sample was heated up from 5 °C to 50 °C ($5\,\frac{°C}{min}$), while the pressure was kept constant. After reaching a temperature of 50 °C, the pressure was stepwise reduced to 70 Pa (3.0 % humidity). The whole process was observed at a magnification of 300 x and recorded.

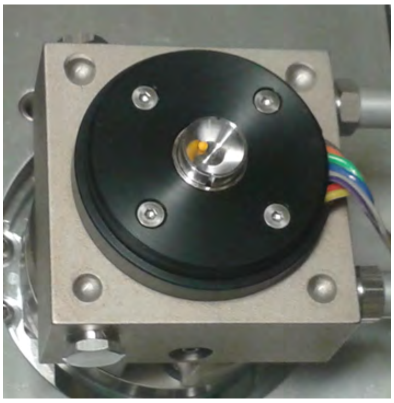

Figure 3.12.: UO_2 particle before ESEM analysis.

3.3.4. TG/DSC

To investigate the thermal behavior and phase transitions TG/DSC analysis were performed (*Netzsch*, *STA 449 C Jupiter*).

- Six particles of each fraction were analyzed. The whole measurement took place in a synthetic air atmosphere, heated up from 25-1300 °C with a constant rate of 10 $\frac{°\mathrm{C}}{\mathrm{min}}$.

3.3.5. XRD

XRD investigations were carried out to define the structure of the crystalline sample. All measurements were performed at room temperature with a *D8 Advance* by *Bruker AXS GmbH*.

- Two particles of each U / Nd composition were ground in a mortar under acetone after thermal treatment. Some drops of this suspension were placed on a Si sample carrier. After drying, the analysis was performed. A 2Θ diffraction angle range from 10-100° with an increment of 0.02° for 1 s was measured. For some samples a 2Θ range of 10-130° was scanned.
- The software *Match!* (Version: 1.11 f) by *Crystal Impact* was used for data analysis and to standardize the diffraction pattern to an intensity of 1,000.
- A Gaussian function according to equation (3.7) was used to fit the pattern and determine the diffraction angle. The variable I symbolizes the reflex intensity.

$$I(2\Theta) = I_0 \cdot e^{-\left(\frac{(2\Theta - 2\Theta_0)^2}{2\sigma_{2\Theta}^2}\right)} \tag{3.7}$$

For each diffraction angle, a cell parameter a was calculated according to Bragg's law (compare eq. (2.14), p. 21), taking equation (3.8) for cubic systems into account. The lattice spacing is described by d, while a is the lattice parameter belonging to the respective 2Θ value. The integers h, k and l are called Miller indices. The X-ray diffraction pattern were assigned to their Miller indices by the use of the already mentioned software *Match!*.

$$d = \frac{a}{\sqrt{h^2 + k^2 + l^2}} \tag{3.8}$$

Furthermore, the lattice parameter a of the crystal structure, as well as the unit cell volume of the cubic system, were determined by the use of the Nelson-Riley method [28]. According to equation (3.9) a Nelson-Riley parameter ($f(\Theta)$) is calculated for each diffraction angle. Afterwards, the a parameter, achieved by Bragg's law is plotted vs. the Nelson-Riley parameter. The resulting datapoints were analyzed by a linear regression, the interception point is equal to the lattice parameter a of the crystal structure.

$$f(\Theta) = \frac{1}{2}\left(\frac{\cos^2\Theta}{\sin\Theta} + \frac{\cos^2\Theta}{\Theta}\right) \tag{3.9}$$

- The mean crystal size L and the lattice distortion $< \epsilon^2 >^{0.5}$ were determined by applying the Hall-Williamson method [29]. The relation, shown in equation (3.10), is converted to the form shown in equation (3.11).

$$B\cos\Theta = \frac{\lambda}{L} + 4 < \epsilon^2 >^{0.5} \sin\Theta \tag{3.10}$$

$$\frac{B\cos\Theta}{\lambda} = 4 < \epsilon^2 >^{0.5} \frac{\sin\Theta}{\lambda} + \frac{1}{L} \tag{3.11}$$

  The term $\frac{B\cos\Theta}{\lambda}$ is plotted as function of $\frac{\sin\Theta}{\lambda}$. By applying a linear regression, the multiplicative inverse of the interception point is equal to the mean crystal size, and the lattice distortion is in accordance to a quarter of the slope.

An example of a XRD pattern after standardization is shown in Figure 3.13. The presented diffractogram belongs to the U / Nd composition with χ(Nd) = 11.99 % treated in reducing H_2:Ar atmosphere at 1300 °C. Each reflex was fitted by the use of a Gaussian function and the diffraction angle was determined. In this way, 10 values for the observed reflexes were obtained. The reflexes were assigned to their Miller indexes (h, k, l) and an a_i value was determined. The Nelson-Riley function was used to calculate a parameter belonging to each reflex (compare equation (3.9)). The results of these calculation are exemplarily listed in Table 3.1 for the χ(Nd) = 11.99 % composition.

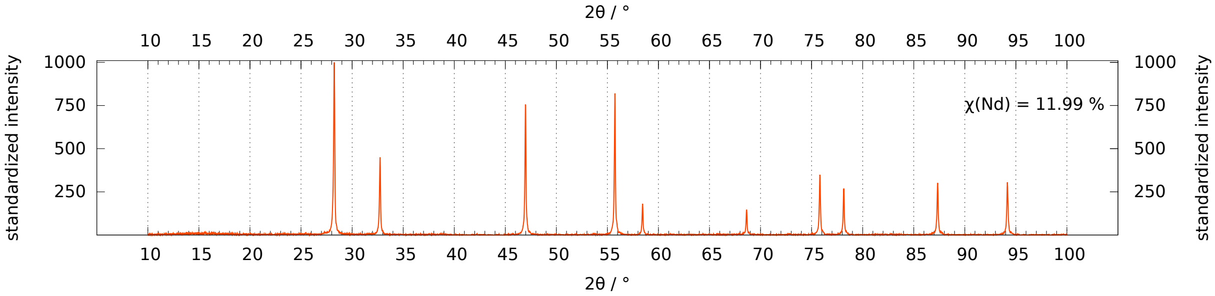

Figure 3.13.: X-ray diffraction pattern, example for microspheres treated in reducing atmosphere at 1300 °C (U / Nd composition with χ(Nd) = 11.99 %), 2Θ range of 10-100°.

The a_i value for each reflex was plotted as function of the resulting Nelson-Riley parameter, like it is shown in Figure 3.14. A linear regression was performed and the resulting interception point is equal to the samples lattice parameter a. In this example the result is

$$a = 5.4649\,\text{Å}.$$

Table 3.1.: Determined reflection angle 2Θ, Miller indexes (h, k, l), a_i and Nelson-Riley parameter $f(\Theta)$ of the U / Nd microspheres (χ(Nd) = 11.99 %), treated in H_2:Ar at 1300 °C.

2Θ / °	h	k	l	a_i / Å	$f(\Theta)$
28.254	1	1	1	5.4664	3.83
32.740	2	0	0	5.4662	3.24
46.984	2	2	0	5.4657	2.08
55.737	3	1	1	5.4655	1.64
58.448	2	2	2	5.4655	1.53
68.633	4	0	0	5.4654	1.17
75.810	3	3	1	5.4653	0.98
78.149	4	2	0	5.4652	0.92
87.339	4	2	2	5.4652	0.72
94.174	5	1	1	5.4651	0.60

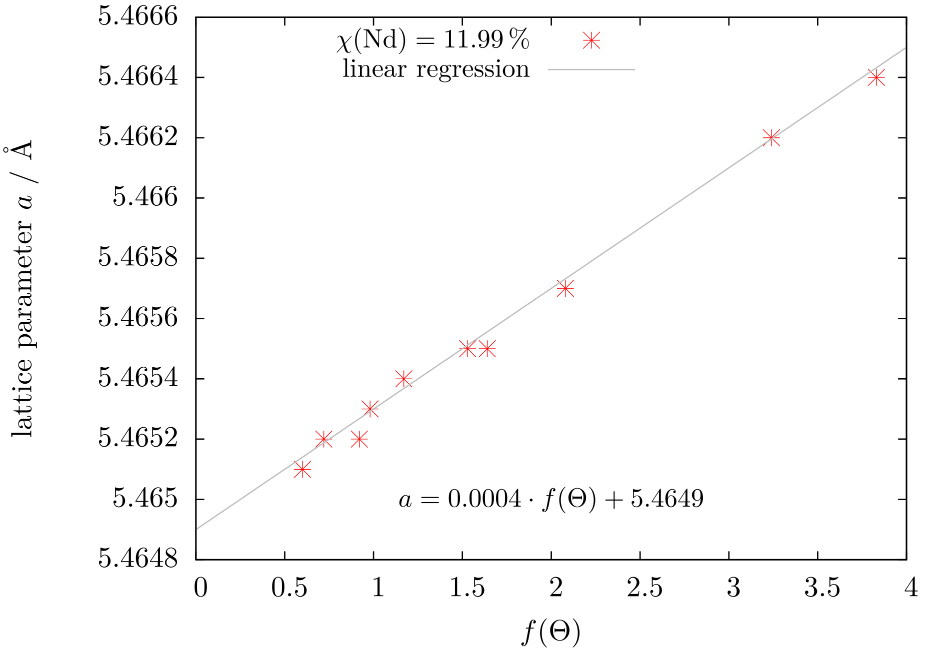

Figure 3.14.: Example of lattice parameter a determination for the U / Nd microspheres (χ(Nd) = 11.99 %), treated in H_2:Ar at 1300 °C, by the use of the Nelson-Riley method.

The mean crystal size L and the lattice distortion $< \epsilon^2 >^{0.5}$ were determined by applying the Hall-Williamson method. The linear regression which had to be generated to get these parameters is exemplarily shown for the already mentioned composition in Figure 3.15. The slope and interception point of the resulted linear function (compare equation (3.11)) were used to calculate the desired parameters. In this example a mean crystal size of

$$L = \frac{1}{1.00 \times 10^{-3}} = 99.68\,\mathrm{nm}$$

and a lattice distortion of

$$< \epsilon^2 >^{0.5} = \frac{1}{4} 6.69 \times 10^{-5} = 0.001\,74\,\%$$

were determined by applying this method.

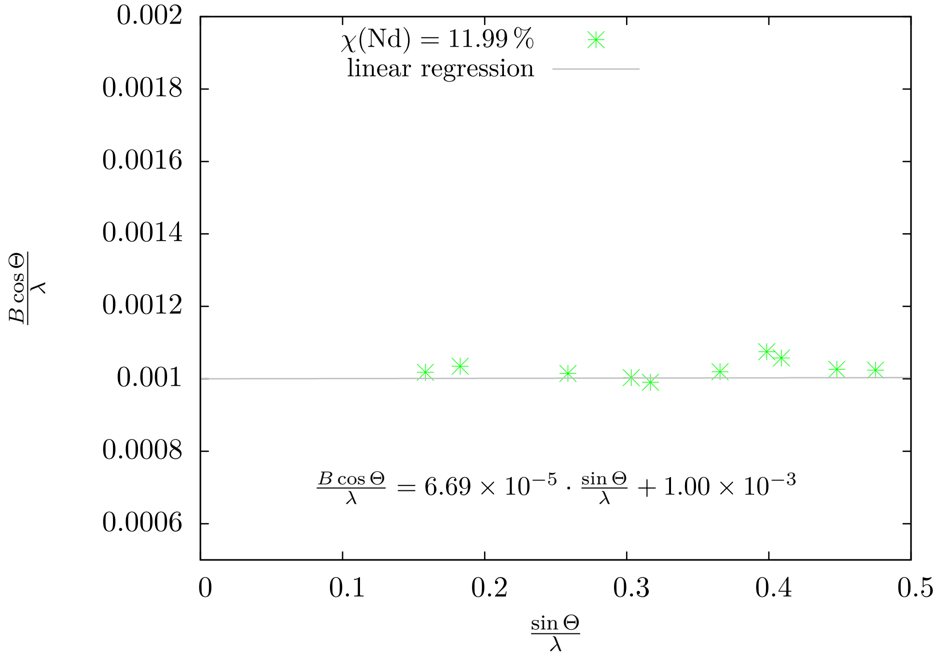

Figure 3.15.: Mean crystal size L and lattice distortion $< \epsilon^2 >^{0.5}$ determination by the use of Hall-Williamson method (particles, treated in H_2:Ar atmosphere at 1300 °C).

4. Results and Discussion

4.1. Fabrication of U / Nd oxide powders

Samples of the mixed U / Nd nitrate precursor solutions before the evaporation were taken to determine the uranium and neodymium concentration by ICP-MS. The results were used to calculate the Nd content, which is presented in Table 4.1. A photography of the resulting powders is shown in Figure 4.1, the crucibles are sorted with an increasing Nd content. The composition at the left contains the mixture with $\chi(\mathrm{Nd}) = 6.60\,\%$, while the right one contains $46.93\,\%$ Nd.

Figure 4.1.: Evaporated powders of all $\chi(\mathrm{Nd})$ compositions.

Before and after calcination in air, the mass loss was recorded by weighing the crucibles. An average mass loss (Δm) of $33\,\%$ was observed, the individual values of the corresponding compositions are listed in Table 4.1. Furthermore, the fabricated powders were investigated by EDX. A comparison of the results, before and after calcination, as well as $\chi(\mathrm{Nd})_{\text{ICP-MS}}$ is plotted in Figure 4.2.

Linear regression of the ICP-MS results shows that overall fractions $14.6\,\%$ more Nd was determined than expected. The correlation of $R^2 = 0.9957$ refers to a systematic error, which must have occurred during the pipetting of the precursor solutions.

EDX results for the powders after evaporation match in the region for Nd contents up to $20\,\%$ quite well to the ones determined by ICP-MS in the solutions. The EDX results for powder fractions containing higher Nd amounts show a kind of saturation at approximately $\chi(\mathrm{Nd})_{measured} = 30\,\%$. This phenomenon was not observed for the calcinated powders. The EDX results are comparable to the values determined by ICP-MS. The observed effect refers to a segregation of the Nd and U phases

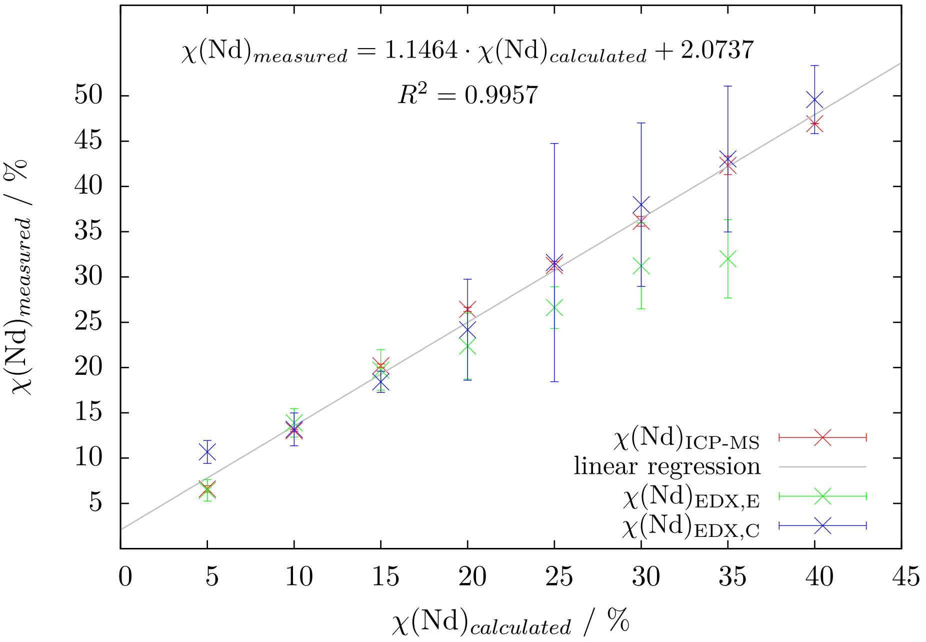

Figure 4.2.: Comparison of $\chi(\mathrm{Nd})_{measured}$ determined by ICP-MS and by EDX.

of the mixtures containing $\chi(\mathrm{Nd}) > 20\,\%$ during evaporation. The calcination seems to reverse this effect (compare $\chi(\mathrm{Nd})_{\mathrm{EDX,C}}$, Table 4.1). The EDX investigations lead to results, which have no significant difference to the $\chi(\mathrm{Nd})$ values determined by ICP-MS. This refers to a homogeneous Nd distribution in the calcinated powders. The large standard deviation can be decreased by an intensive grinding of the powders. All results are summarized in Table 4.1, $\chi(\mathrm{Nd})_{\mathrm{EDX,E}}$ indicate the EDX results of the mixtures before calcination, while the values achieved afterwards are represented as $\chi(\mathrm{Nd})_{\mathrm{EDX,C}}$. For further comparisons the $\chi(\mathrm{Nd})$ values determined by ICP-MS were used.

Table 4.1.: Nd content of the powders, determined by ICP-MS.

$\chi(\mathrm{Nd})_{theoretical}$ / %	$\chi(\mathrm{Nd})_{\mathrm{ICP\text{-}MS}}$ / %	σ	$\chi(\mathrm{Nd})_{\mathrm{EDX,E}}$ / %	σ	$\chi(\mathrm{Nd})_{\mathrm{EDX,C}}$ / %	σ	Δm / %
5	6.60	0.36	6.44	1.19	10.68	1.27	30.68
10	13.03	0.10	13.90	1.58	13.18	1.82	35.06
15	20.20	0.20	19.74	2.25	18.43	1.17	37.18
20	26.43	0.24	22.37	3.64	24.17	5.58	27.41
25	31.28	0.44	26.63	2.31	31.60	13.15	25.59
30	36.16	0.54	31.22	4.75	37.99	9.02	32.67
35	42.33	1.02	32.01	4.33	43.03	8.05	36.52
40	46.93	0.00			49.59	3.76	36.97

4.2. Preparation of microspheres

Results obtained for the synthesized U / Nd microspheres are discussed in the following sections. First, the fabrication and characterization of the untreated spherical particles, the so called green bodies, is discussed, followed by the results of the thermal treatment. The last section describes the results achieved by the thermal treatment.

4.2.1. Preparation of green bodys

4.2.1.1. Precursor solution

All prepared precursor solutions were analyzed by ICP-MS to determine the metal concentrations $c(M)$. The nitrate content in the ADUN solutions was furthermore analyzed with a photometer and a nitrate test kit. The metal concentrations of the initial solutions (before mixing) are summarized in Table 4.2. The $\mathrm{NO_3^-}$ content of the ADUN solution is expressed by $R(\mathrm{NO_3^-})$ which is defined as $\mathrm{NO_3^-}$ amount over the uranium amount, as expressed in equation (4.1).

$$R(\mathrm{NO_3^-}) = \frac{n(\mathrm{NO_3^-})}{n(U)} \tag{4.1}$$

Table 4.2.: Metal concentration (U, Nd respectively) $c(M)$ of the precursor solutions determined by ICP-MS, and $c(\mathrm{NO_3^-})$ as well $R(\mathrm{NO_3^-})$ of the ADUN solutions (photometer).

solution	$c(M)$ / $\frac{\mathrm{mol}}{\mathrm{L}}$	$c(\mathrm{NO_3^-})$ / $\frac{\mathrm{mol}}{\mathrm{L}}$	$R(\mathrm{NO_3^-})$
ADUN 1	2.58	3.89	1.51
ADUN 2	2.50	4.03	1.61
$\mathrm{Nd(NO_3)_3}$	2.98		

4.2.1.2. Gelation and washing

Figure 4.3 shows a photograph of the fabricated microspheres, dried at air. The pure uranium containing fraction in the crucible at the left can easily be identified by its yellow color. When more Nd is added a more intense red coloration can be observed. The U / Nd oxide particles at the right are the one containing a Nd amount fraction of 40 %.

The ICP-MS analysis of the dissolved spheres were used to calculate $\chi(\mathrm{Nd})$. The mass concentrations $\beta(\mathrm{U})$ and $\beta(\mathrm{Nd})$ were determined and transformed into the molar concentrations (c(U), c(Nd)). c(Nd) devided by the sum of c(U) and c(Nd) leads to $\chi(\mathrm{Nd})$. The results are summarized in Table 4.3.

The Nd content measured was found to be higher than expected for all compositions. Several side effects can cause this, on the one hand the systematic error due to pipetting which was already mentioned at the powder characterization could be a reason for this deviation. On the other hand, the ICP-MS results of the aging solutions and the washing solutions (Figure 4.4) show that some

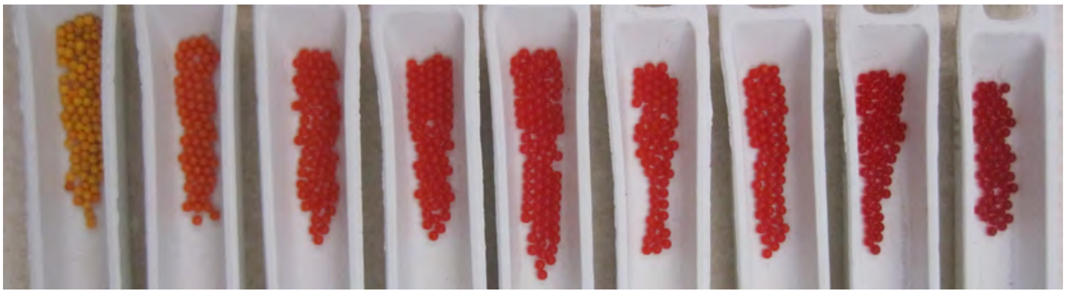

Figure 4.3.: Photography of prepared microspheres, dried at air.

Table 4.3.: Nd content of microspheres, determined by ICP-MS.

$\chi(\mathrm{Nd})_{theoretical}$ / %	$\chi(\mathrm{Nd})_{\text{ICP-MS}}$ / %	σ
5	5.80	0.002
10	11.99	0.003
15	17.40	0.006
20	22.62	0.004
25	27.59	0.013
30	33.49	0.007
35	37.68	0.010
40	42.63	0.006

fractions of either metal were washed out. The determined values are listed in Table 4.4. It can be observed that the amount of U removed from the particle is much higher than the Nd amount removed. For better comparison, the ratio of both metal concentrations of each sample was calculated for the aging solution ($\frac{c(\mathrm{U})}{c(\mathrm{Nd})}$). A decrease of the determined ratio with increasing $\chi(\mathrm{Nd})$ in the particle compositions was found.

The ICP-MS analysis were performed with the dissolved green bodies. This method taking into account the total volume, also the U concentration was determined by this method. The results are used as reference for further analysis.

Table 4.4.: Determined U and Nd concentration in the aging solution and second washing water.

	aging solution			washing water 2	
$\chi(\mathrm{Nd})$ / %	$c(\mathrm{U})$ / $\frac{\mathrm{mmol}}{\mathrm{L}}$	$c(\mathrm{Nd})$ / $\frac{\mathrm{mmol}}{\mathrm{L}}$	$\frac{c(\mathrm{U})}{c(\mathrm{Nd})}$	$c(\mathrm{U})$ / $\frac{\mathrm{mmol}}{\mathrm{L}}$	$c(\mathrm{Nd})$ / $\frac{\mathrm{mmol}}{\mathrm{L}}$
5.80	1.86931	0.00160	1167.2	0.00508	0.00003
11.99	2.81327	0.00279	1009.4	0.04225	0.00009
17.40	2.53786	0.00263	963.3	0.01054	0.00024
22.62	1.73506	0.00214	809.9	0.00956	0.00040
27.59	1.76635	0.01232	143.4	0.01409	0.00112
33.49	2.13455	0.01078	198.0	0.01423	0.00042
37.68	0.40817	0.00374	109.0	0.00744	0.00135
42.63	0.31792	0.15563	2.0	0.00326	0.00033

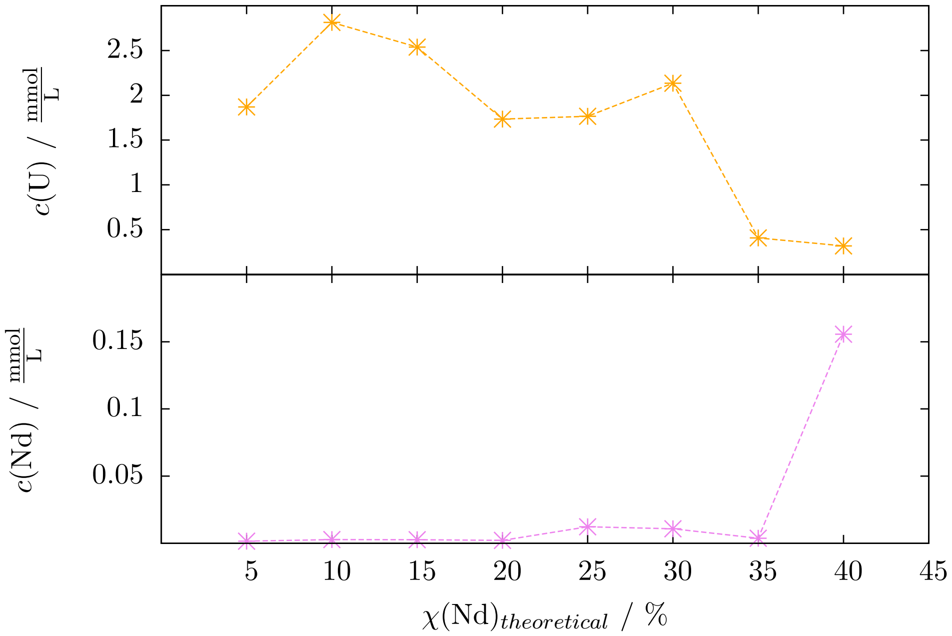

Figure 4.4.: U and Nd content in the aging solutions, measured by ICP-MS.

4.2.2. Characterization of green bodies

The prepared microspheres were characterized by determining the parameters mass (m) and diameter (d), which were used to calculate the particle volume (V) and its density (ρ).

4.2.2.1. Mass distribution

Thirty spheres (N) of each $\chi(\mathrm{Nd})$ composition were weighed. The difference in the minimum and maximum mass was determined and divided by $\sqrt{N}$. The achieved value was added as increment to the minimum value to generate a class. The increment was again added to the upper class range, in this way 5 classes were generated. The abundances of the mass for each class was count and is summarized in Table 4.5 and presented in Figure 4.5. Due to the fact that the microspheres were prepared manually the type of distribution function was not further investigated.

The average sphere mass $\overline{m}_{sphere}$ of each batch, as well as the standard deviation σ was calculated and are presented in Table 4.5 as well. There is no significant correlation between sphere mass and the Nd content. Each microsphere has a mass of approximately 5 mg. A histogram is representatively plotted for the $\chi(\mathrm{Nd}) = 5.80\,\%$ composition in Figure 4.5.

Table 4.5.: Mass distribution and average masses of 30 microspheres per batch.

χ(Nd) %	class 1	class 2	class 3	class 4	class 5	$\overline{m}_{sphere}$ / mg	σ
5.80	3.3 %	30.0 %	56.7 %	6.7 %	3.3 %	5.38	0.36
11.99	3.3 %	0.0 %	30.0 %	50.0 %	16.7 %	5.23	0.23
17.40	3.3 %	23.3 %	50.0 %	16.7 %	6.7 %	4.96	0.19
22.62	13.3 %	10.0 %	30.0 %	23.3 %	23.3 %	5.24	0.14
27.59	6.7 %	10.0 %	33.3 %	43.3 %	6.7 %	4.83	0.18
33.49	3.3 %	0.0 %	56.7 %	30.0 %	10.0 %	5.00	0.46
37.68	10.0 %	10.0 %	20.0 %	46.7 %	13.3 %	5.34	0.22
42.63	3.3 %	10.0 %	36.7 %	30.0 %	20.0 %	5.55	0.39

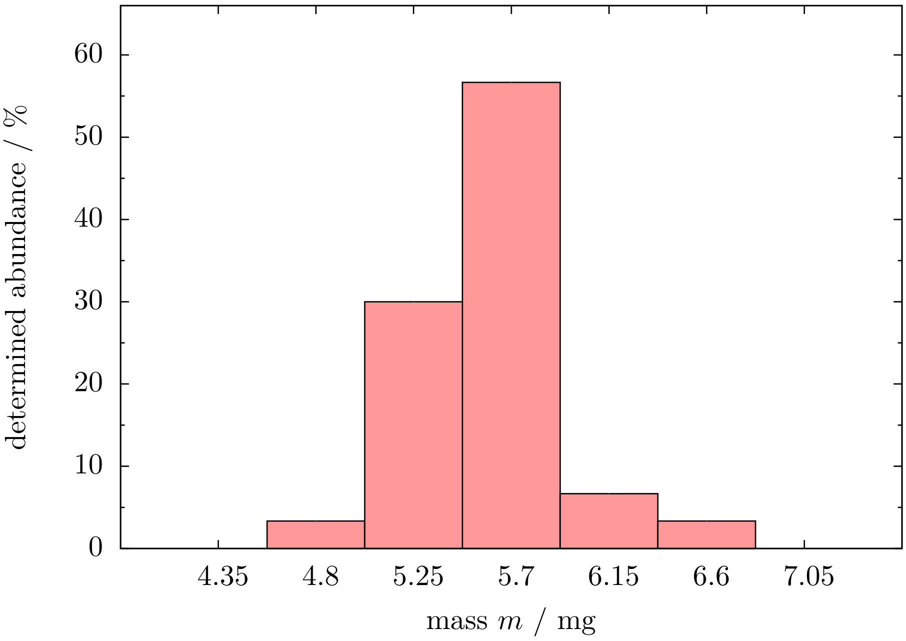

Figure 4.5.: Mass distribution of 30 microspheres χ(Nd) = 5.80 %.

4.2.2.2. Shape, diameter, volume

Investigations by SEM showed that spherical particles were synthesized. Images, recorded with a 150 fold magnification, of one particle of each fraction are visualized in Figure 4.6. The microspheres with lower Nd contents ($\leq 11.99\,\%$) show a large number of semi superficial cracks.

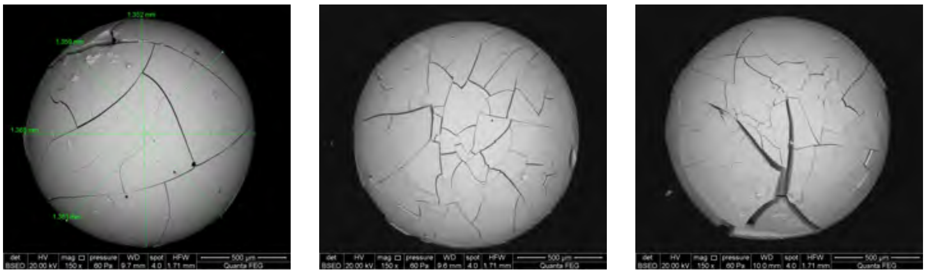

(a) χ(Nd)=0.00 % **(b)** χ(Nd)=5.80 % **(c)** χ(Nd)=11.99 %

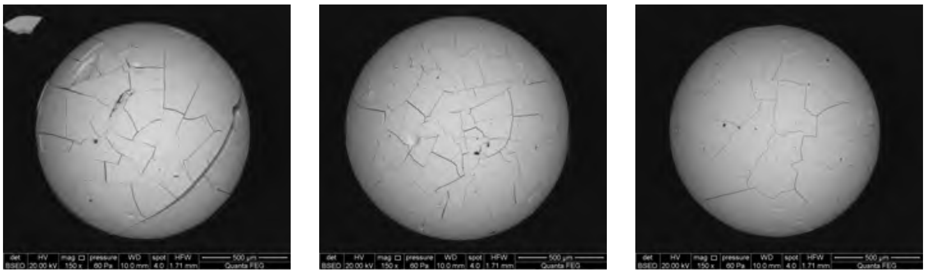

(d) χ(Nd)=17.40 % **(e)** χ(Nd)=22.62 % **(f)** χ(Nd)=27.59 %

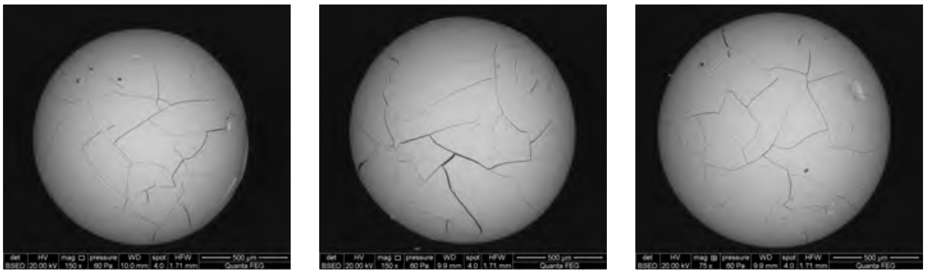

(g) χ(Nd)=33.49 % **(h)** χ(Nd)=37.68 % **(i)** χ(Nd)=42.63 %

Figure 4.6.: Green bodie of each particle composition during SEM analysis (magnification: 150x).

Furthermore, an example of the size measurements is shown as Figure 4.6, (a). The average diameter ($\overline{d}_{1,2,3,4}$) and the standard deviation of each observed particle were generated. These values were used to calculate the weighted mean $\overline{d}$ (compare eq. (4.2)) and the corresponding standard deviation (compare eq. (4.3)) for each fraction. The results of all diameter measurements are summarized in Table 4.6.

$$\overline{d} = \sqrt{\frac{\Sigma_{i=1}^{4} \frac{\overline{d}_{1,2,3,4}}{\sigma^2}}{\Sigma_{i=1}^{3} \frac{1}{\sigma^2}}} \tag{4.2}$$

$$\sigma_{weighted} = \sqrt{\frac{1}{\Sigma_{i=1}^{4} \frac{1}{\sigma^2}}} \tag{4.3}$$

Table 4.6.: Diameter determined for each observed green body by SEM.

χ(Nd) / %		d_1 / mm	d_2 / mm	d_3 / mm	d_4 / mm	$\overline{d}_{1,2,3,4}$ / mm	$\overline{d}$ / mm	σ
0	sphere 1	1.361	1.368	1.359	1.352	1.360	1.356	0.006
	sphere 2	1.348	1.321	1.332	1.358	1.340		
	sphere 3	1.374	1.333	1.324	1.345	1.344		
5.80	sphere 1	1.352	1.332	1.343	1.339	1.342	1.323	0.004
	sphere 2	1.320	1.314	1.327	1.310	1.318		
	sphere 3	1.306	1.319	1.321	1.311	1.314		
11.99	sphere 1	1.375	1.334	1.324	1.323	1.339	1.340	0.009
	sphere 2	1.360	1.330	1.350	1.347	1.347		
	sphere 3	1.348	1.335	1.307	1.324	1.329		
17.40	sphere 1	1.280	1.282	1.274	1.277	1.278	1.286	0.003
	sphere 2	1.293	1.295	1.305	1.297	1.298		
	sphere 3	1.304	1.314	1.327	1.308	1.313		
22.62	sphere 1	1.315	1.319	1.312	1.314	1.315	1.318	0.002
	sphere 2	1.322	1.330	1.325	1.331	1.327		
	sphere 3	1.316	1.320	1.310	1.307	1.313		
27.59	sphere 1	1.268	1.273	1.272	1.268	1.270	1.263	0.002
	sphere 2	1.246	1.250	1.255	1.250	1.250		
	sphere 3	1.273	1.257	1.253	1.266	1.262		
33.49	sphere 1	1.370	1.378	1.364	1.359	1.368	1.345	0.003
	sphere 2	1.359	1.360	1.368	1.365	1.363		
	sphere 3	1.288	1.275	1.288	1.277	1.282		
37.68	sphere 1	1.339	1.338	1.352	1.345	1.344	1.337	0.003
	sphere 2	1.334	1.329	1.337	1.336	1.334		
	sphere 3	1.337	1.342	1.361	1.349	1.347		
42.63	sphere 1	1.394	1.385	1.394	1.400	1.393	1.385	0.003
	sphere 2	1.395	1.382	1.386	1.392	1.389		
	sphere 3	1.368	1.372	1.382	1.373	1.374		

For the investigated particles a weighted mean diameter in a range of 1.26-1.39 mm was found. The small standard deviation leads to the assumption that a spherical shape was achieved.

The cracks on the particles surface point to a shrinkage during SEM parameter setting. Due to the low pressure of 60 Pa, residual humidity leaves the particles and may cause these cracks.

To prove the assumption for the crack formation, ESEM analysis were performed. Pictures of the ESEM investigations are shown in Figure 4.7. The three images show the same sector of one microsphere. Image (a) was taken at the initial conditions with a temperature of 5 °C. The humidity was 97.0 % and a pressure of 850 Pa was present. The high humidity is the reason for the cloudy view, but a surface integrity can be recognized. Image (b) shows the particle at 50 °C. At these condition the humidity was decreased to 31.6 % and the beginning of a crack formation can be seen. In image (c) this formation is completed.

This example proves the assumption for the crack formation during the adjustment of SEM conditions. It has to be concluded that the diameters determined by SEM are not valid for density calculations of these spheres due to a shrinkage. A method, working under ambient conditions, must be used to achieve accurate average diameters.

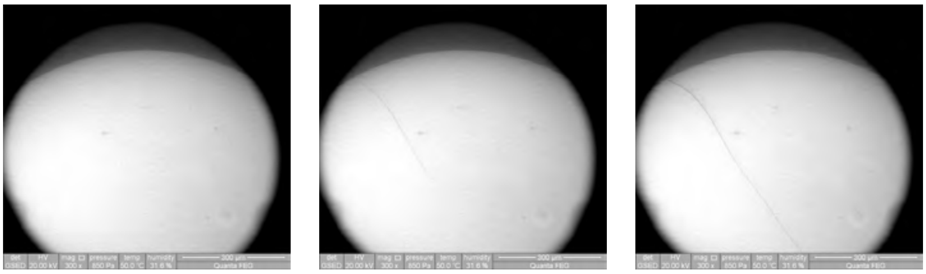
(a) (b) (c)

Figure 4.7.: Microsphere (χ(Nd) = 22.6 %) during ESEM analysis.

In order to measure diameters useful for density calculations further investigations with an optical microscope were performed. Images of thirty spheres of each particle composition were taken, an example is shown in Figure 4.8). At the center of the surface a reflection from the microscopy light can be recognized.

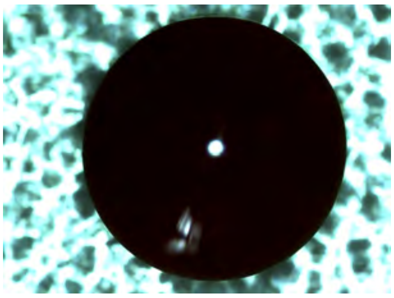

Figure 4.8.: Optical microscope image of a sphere.

The images achieved in this way were further analyzed by the software ImageJ, as described in section 3.3. A composite image containing 30 single images and a standard was generated for each U / Nd composition and used as input file for ImageJ. The software starts a particle detection procedure and determines characteristic particle parameters like the surface area A. Figure 4.9 shows an example for the recognized particles of the χ(Nd) = 42.63 % composition.

A spherical geometry was already proven by SEM and is confirmed by the optical microscopy investigations. Due to this fact, geometrical formulas are valid to calculate the diameter. The particle area A, determined by ImageJ, was used to calculate the circle diameter (compare equation (4.4)). Moreover the corresponding sphere volume according to equation (4.5) was calculated. To summa-

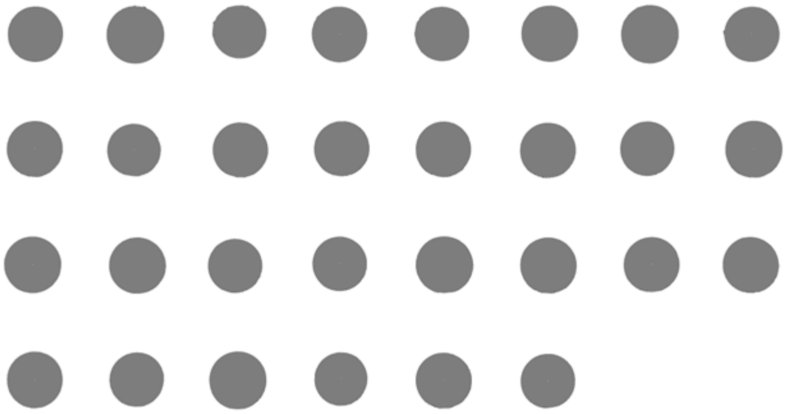

Figure 4.9.: Particles analyzed with ImageJ ($\chi(\text{Nd}) = 42.63\,\%$).

rize the results a weighted mean of the 30 diameters ($\overline{d}_{sphere}$) and volumes ($\overline{V}_{sphere}$) of the fabricated particle compositions, as well as their corresponding standard deviation (σ) were calculated and are presented in Table 4.7.

$$d_{circle} = \sqrt{\frac{4A_{circle}}{\pi}} \tag{4.4}$$

$$V_{sphere} = \frac{1}{6}\pi d_{sphere}^3 \tag{4.5}$$

Table 4.7.: Average sphere diameters and volumes, analyzed with ImageJ.

$\chi(\text{Nd})$ / %	$\overline{d}_{sphere}$ / µm	σ	$\overline{V}_{sphere}$ / mm^3	σ
5.80	1353.7	30.9	1.301	0.091
11.99	1352.5	19.1	1.296	0.055
17.40	1334.1	15.5	1.244	0.044
22.62	1375.4	12.8	1.363	0.038
27.59	1336.3	15.8	1.250	0.044
33.49	1353.7	29.0	1.301	0.086
37.68	1383.3	20.5	1.387	0.061
42.63	1406.7	33.4	1.460	0.104

The diameters determined by SEM (tab. 4.6) and microscopically determined diameters are shown in Figure 4.10 as function of the Nd content. The same trend can be observed, but the diameters, determined by SEM, are 15-75 µm smaller than the one determined with optical microscopy. This effect could be explained by the shrinkage of the spheres during the evaporation of residual humidity, while the pressure decrease to reach SEM conditions. The fact that the diameter difference varied over all composition leads to the assumption that some fractions contain more residual humidity than others. The $\chi(\mathrm{Nd}) = 11.99\,\%$ fraction seems to be quite dry in comparison to the other fractions, the largest diameter difference was found for the $\chi(\mathrm{Nd}) = 27.59\,\%$ composition.

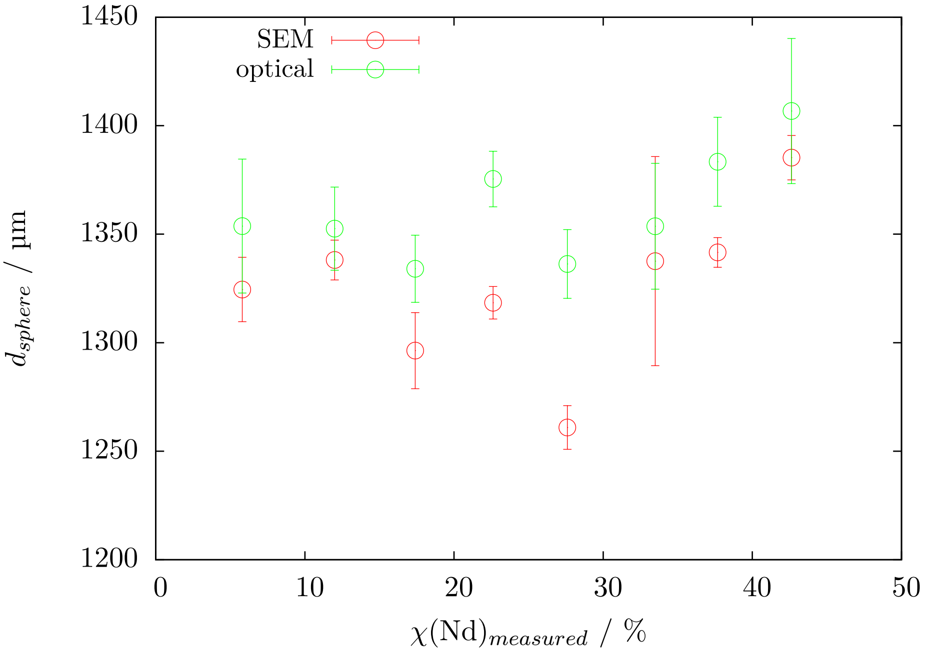

Figure 4.10.: Comparison of the average green body diameter d_{sphere}, determined by SEM at $P = 60\,\mathrm{Pa}$ and by optical microscopy at standard pressure.

4.2.2.3. Density

The density ρ of each sphere was calculated according to equation (4.6). To assess the particle density, the corresponding masses and calculated particle volumes were used. A weighted mean of the initial values for the average fraction masses and average volumes, as well as the results of the density calculations are listed in Table 4.8.

$$\rho_{sphere} = \frac{m_{sphere}}{V_{sphere}} \tag{4.6}$$

Furthermore, the results of the calculations are plotted as function of the Nd content in Figure 4.11. A negative linear trend up to a Nd content of 22.62 % can be observed. Fractions containing more Nd show a constant value of approximately $3.852\,\frac{\mathrm{g}}{\mathrm{cm}^3}$.

Table 4.8.: Calculated green body densities.

$\chi(\mathrm{Nd})$ / %	$\overline{m}_{sphere}$ / mg	σ	$\overline{V}_{sphere}$ / mm^3	σ	$\overline{\rho}_{sphere}$ / $\frac{\mathrm{g}}{\mathrm{cm}^3}$	σ
5.80	5.38	0.36	1.301	0.091	4.147	0.344
11.99	5.23	0.23	1.296	0.055	4.040	0.203
17.40	4.96	0.19	1.244	0.044	3.990	0.141
22.62	5.24	0.14	1.363	0.038	3.848	0.147
27.59	4.83	0.18	1.250	0.044	3.871	0.181
33.49	5.00	0.46	1.301	0.086	3.855	0.375
37.68	5.34	0.22	1.387	0.061	3.853	0.186
42.63	5.55	0.39	1.460	0.104	3.813	0.340

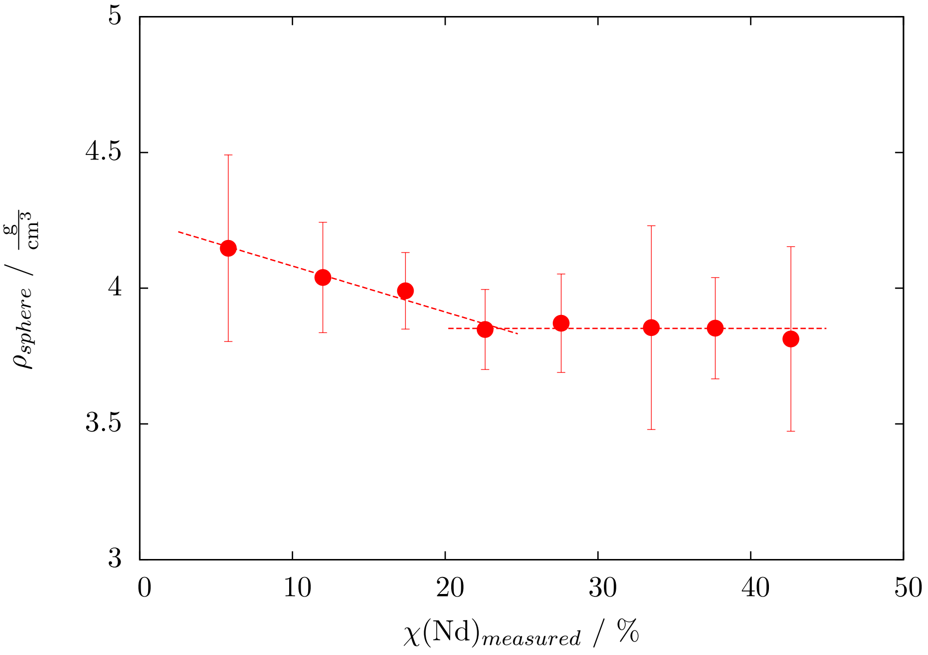

Figure 4.11.: Calculated average green body density $\overline{\rho}_{sphere}$ as function of $\chi(\mathrm{Nd})$.

4.2.2.4. Homogenity

SEM/EDX analysis were performed to determine the Nd distribution over the whole particle volume, and its chemical composition. Images with a 150x magnification were taken (compare Figure 4.6) and a squarish sector, as introduced in the previous chapter (Figure 3.11, p. 32), was analyzed by EDX. A spectrum was recorded for all observed particles. An example is shown in Figure 4.12 for a microsphere of the $\chi(\mathrm{Nd}) = 27.59\,\%$ composition.

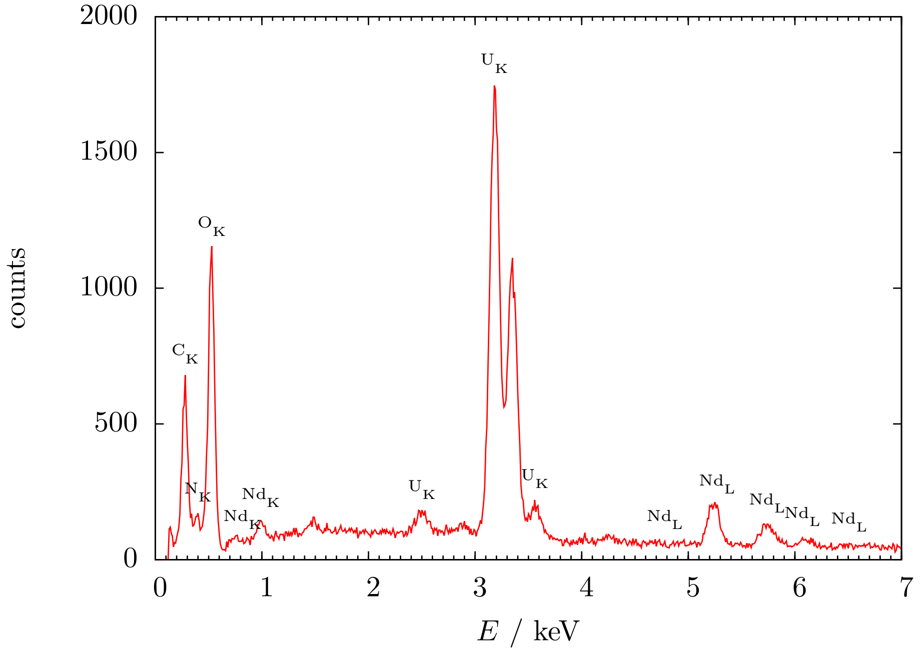

Figure 4.12.: Example of an EDX spectra ($\chi(\mathrm{Nd}) = 27.59\,\%$).

The indexes K and L indicate the origin shell of the electron transition. The typical signals for U and Nd can be recognized. Furthermore, a high intensity of carbon was found in this example. The peak is caused by the conductive tab, used to stick the particles onto the SEM specimen holder. The Nd content for each particle $\chi(\mathrm{Nd})_i$ was analyzed and the average value for each composition $\overline{\chi}(\mathrm{Nd})$, as well as its standard deviation σ were calculated and are summarized in Table 4.9.

Table 4.9.: Nd content of untreated spheres, determined by EDX.

$\chi(\mathrm{Nd})_{theoretical}$ / %	$\chi(\mathrm{Nd})_1$ / %	$\chi(\mathrm{Nd})_2$ / %	$\chi(\mathrm{Nd})_3$ / %	$\overline{\chi}(\mathrm{Nd})$ / %	σ
5	4.43	5.52	5.74	5.23	0.70
10	11.34	12.49	9.98	11.27	1.26
15	15.40	18.67	13.57	15.88	2.58
20	22.11	18.69	17.76	19.52	2.29
25	24.53	30.07	26.69	27.10	2.79
30	34.76	33.63	32.04	33.48	1.37
35	37.28	35.54	34.64	35.82	1.34
40	42.87	42.15	40.69	41.90	1.11

Figure 4.13 shows the Nd contents determined by EDX (Table 4.9) as function of the ICP-MS results (Table 4.3). The plotted linear function shows $\chi(\mathrm{Nd})_{EDX} = \chi(\mathrm{Nd})_{ICP-MS}$, which describes the achieved data points very well. Small exceptions show the U / Nd composition with a Nd content of 17.40 %, 22.62 % and 37.68 %. These deviations can be caused by morphological effects which disturb the EDX measurements. In comparison to the ICP-MS results a larger standard deviation (0.7-2.8 %) was found (Table 4.9 and 4.3).

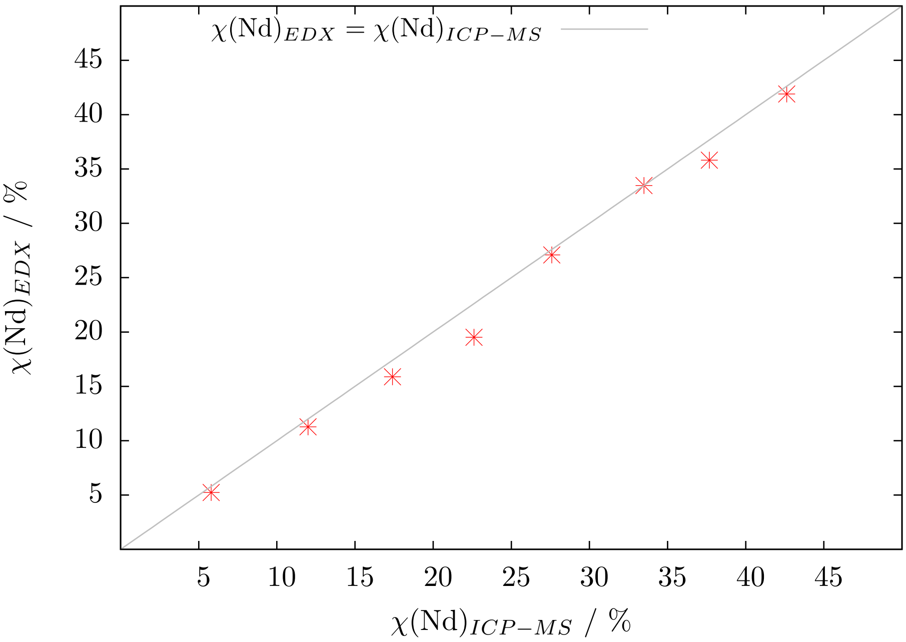

Figure 4.13.: Average $\chi(\mathrm{Nd})$ determined by EDX as function of $\chi(\mathrm{Nd})_{ICP-MS}$.

The fact that the EDX investigations penetrate the particle not very deep, leads to the conclusion that the Nd is homogeneously distributed in the whole uranium matrix of the spherical particle.

Considerations for the further analysis refer to the ICP-MS results because this measurement method analysis the whole sphere volume.

4.2.2.5. Thermal behavior

To study the thermal behavior of the microspheres, TG/DSC analysis were done. The results are summarized in Figure 4.14. A removal of the residual humidity as well as a decomposition of the organic gelification agents up to 400 °C was recognized.

The observed endothermic peaks in the region of 120-140 °C belong to a melting of urea. A further decomposition of urea into cyanic acid, HNCO, and ammonia, and the production of biuret $NH(CONH_2)_2$ takes place at the temperature range of 170-190 °C and was also observed as endothermic effect by DSC. These observed effects correspond to published investigations of the decomposition behavior of urea by Schaber et al. [30]. They also observed endothermic effects in the range of 220-250 °C, which goes in accordance with the decomposition of biuret and production of cyanuric acid $(CONH)_3$, cyanic acid and ammonia, which was also observed in the fabricated

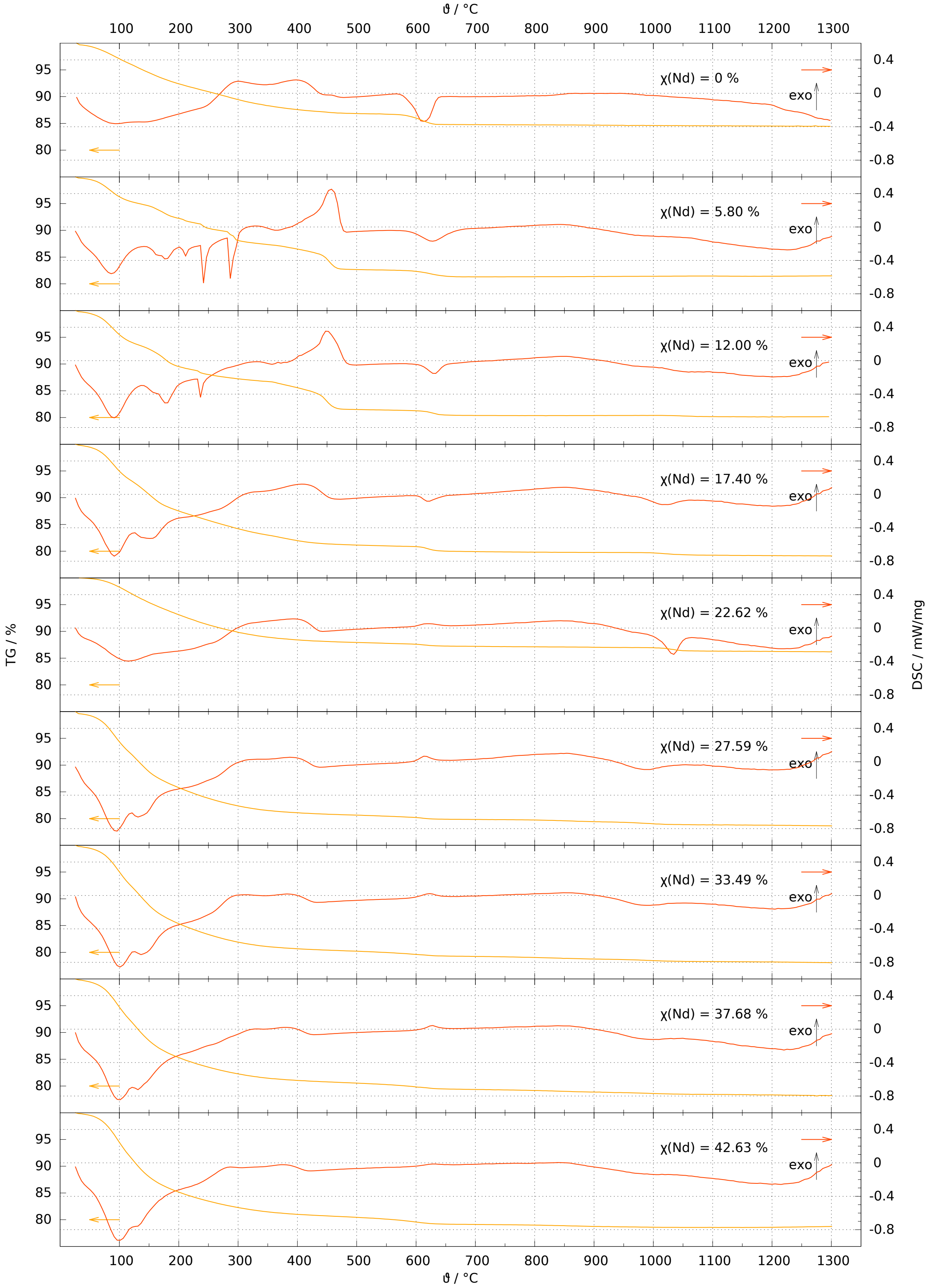

Figure 4.14.: TG/DSC of the prepared uranium and U / Nd green bodies, dried at air.

U / Nd particle compositions. Detailed investigations of the HMTA decomposition are published by Gusev et al. [31]. They observed an endothermic peak at 206 °C according to sublimation and decomposition of HMTA. Benay et al. [32] reproduced the discussed DSC measurements and analyzed a 1 : 1 mixture of HMTA and urea. They confirmed the published results and report about reactions between decomposition products of HMTA and urea, observed as an exothermic peak in the range of 310-350 °C.

At the temperature of ca. 450 °C exothermic effects due to the transformation of UO_2 to U_3O_8 were observed. In the region of 550-700 °C the particle compositions up to $\chi(\mathrm{Nd}) \leq 17.40\,\%$ undergo an endothermic phase transition accompanied with an stepwise mass loss, while the uranium particles containing higher Nd amount fractions showed an exothermic effect. This associates with the material crystallization, which is endothermic for uranium oxide and exothermic for neodymium oxide. Moreover an endothermic effect at $\vartheta > 900\,°\mathrm{C}$ was observed for some samples. Detailed investigations of the thermal effect at high temperature should be performed in the future.

The major mass loss for all uranium neodymium particle compositions took place up to 500 °C ($\approx 18\,\%$). The mass loss, observed for temperatures $> 500\,°\mathrm{C}$ is rather small ($1 - 3\,\%$). All samples show a total mass loss in a range of 19-22 %. The microspheres with $\chi(\mathrm{Nd}) = 22.62\,\%$ share the only exception, they lost ca. 14 % of their initial mass.

4.2.3. Thermal treatment

An example of particles treated in air and reducing H_2:Ar atmosphere is shown in Figure 4.15. Photos of the green bodies are shown on the top, while the particles after thermal treatment are at the bottom. The shown microspheres belong to the $\chi(\mathrm{Nd})$=33.49 % fraction.

(a) treated in air at 1300 °C **(b)** treated in H_2:Ar at 1300 °C **(c)** treated in H_2:Ar at 1600 °C

Figure 4.15.: Photos of microspheres belonging to the $\chi(\mathrm{Nd}) = 33.49\,\%$ composition, before (top) and after thermal treatment (bottom).

The treatment of all synthesized U / Nd compositions led to integer spherical particles. The mass loss of the treated samples was determined by a weighing of the crucibles before and after treatment. Figure 4.16 compares the percentage mass losses achieved by the TG/DSC analysis and the calculated one for the microspheres treated in the furnace.

Quite similar mass losses of 20-25 % can be recognized, even for the particles treated in the reducing atmosphere. The huge outliner in the TG/DSC results for the $\chi(\mathrm{Nd}) = 22.62\,\%$ composition can be explained by the fact, that these particles were more dry and less residual humidity in comparison to the other compositions vaporized during the analysis. These measurements should be repeated with constant initial parameters for the samples. The particles should be placed in a dryer, in order to ensure comparable residual humidity conditions. The discrepancy for the treated

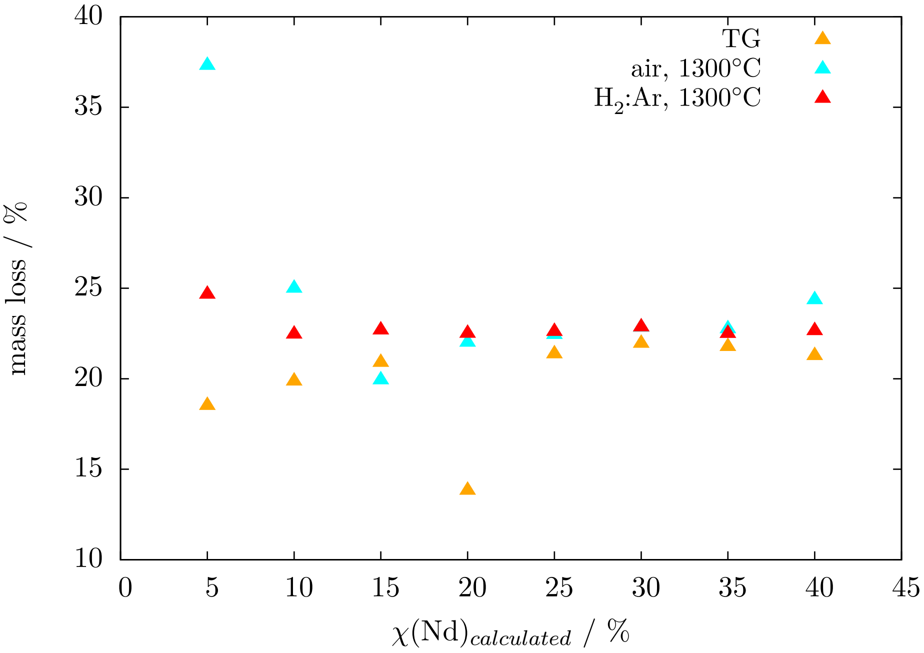

Figure 4.16.: Mass loss comparison of microspheres treated with TG and furnance.

microspheres in the furnace, containing low amounts of Nd, can be explained by decompositions of the organic residuals. This may have led to a particle distribution in the furnace and explain the high mass losses.

4.3. Characterization of microspheres

The SEM investigations showed that the particles underwent a shrinkage during the thermal treatment, as expected. Figure 4.17 shows an image of a green body (a) and a particle treated in air (b) at 1300 °C. Furthermore, particles treated under reducing conditions in a H_2:Ar atmosphere are shown, the microsphere in images (c) at 1300 °C and the one on (d) at 1600 °C. All particle belong to the $\chi(\mathrm{Nd}) = 42.63\,\%$ fraction and the images are recorded with a magnification of 150x.

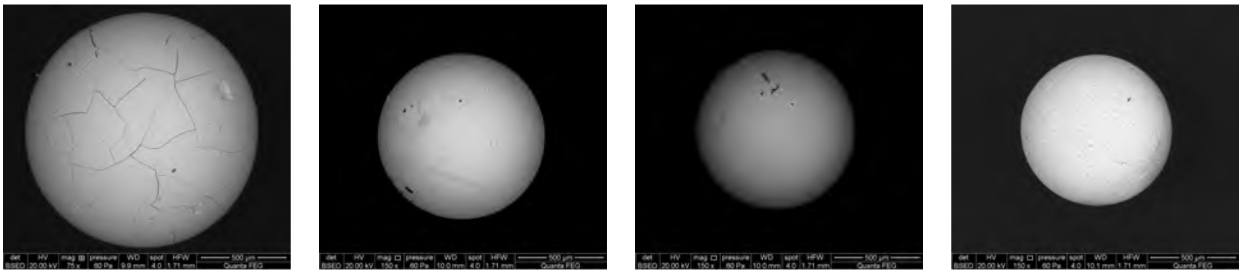
(a) green body **(b)** air, 1300 °C **(c)** H_2:Ar, 1300°C **(d)** H_2:Ar, 1600 °C

Figure 4.17.: SEM images ($\chi(\mathrm{Nd}) = 42.63\,\%$).

It can be recognized that the use of an reducing H_2:Ar atmosphere leads to quite dense particles in comparison to the treatment in air. The pore size correspond to the maximum temperature and total treatment time. The grains in particle (d) underwent a bigger diffusion than the one in particle (c).

The results of SEM and XRD measurements are summarized in the ongoing sections for each used thermal treatment atmosphere.

4.3.1. Characterization of particles treated in air

4.3.1.1. SEM/EDX analysis

A SEM image of a representative microsphere of each synthesized U / Nd composition, treated in air at 1300 °C, is presented in Figure 4.18. The trend regarding the integrity which was observed for the green bodies can also be recognized for the particles treated in air. Particles of compositions with $\chi(\text{Nd}) \leq 11.99\,\%$ seem to be more fragile than the microspheres containing higher Nd amounts.

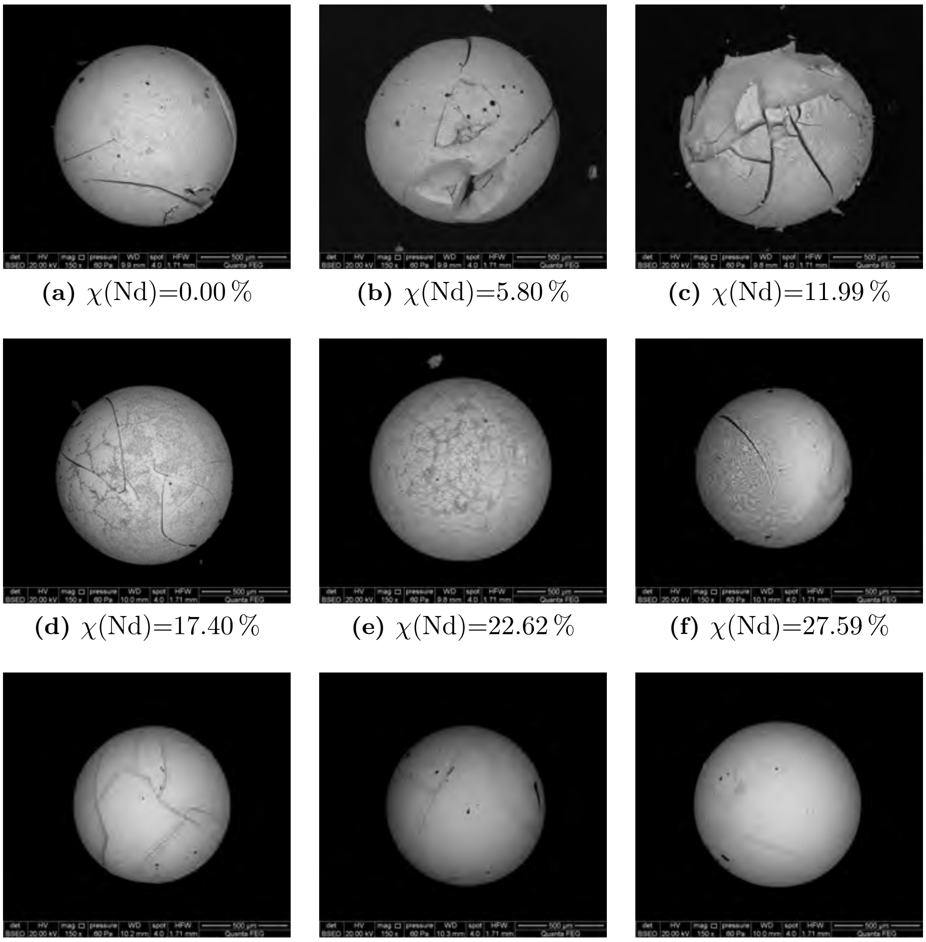

(a) $\chi(\text{Nd})=0.00\,\%$ **(b)** $\chi(\text{Nd})=5.80\,\%$ **(c)** $\chi(\text{Nd})=11.99\,\%$

(d) $\chi(\text{Nd})=17.40\,\%$ **(e)** $\chi(\text{Nd})=22.62\,\%$ **(f)** $\chi(\text{Nd})=27.59\,\%$

(g) $\chi(\text{Nd})=33.49\,\%$ **(h)** $\chi(\text{Nd})=37.68\,\%$ **(i)** $\chi(\text{Nd})=42.63\,\%$

Figure 4.18.: Microspheres of each composition, treated at 1300 °C in air during SEM analysis.

During detailed SEM investigations a huge porosity was observed for the particles treated in air. Figure 4.19 shows an overview and a closeup of a pure uranium sphere. Regarding the porosity it can be distinguished between intergrain and intragrain pores. The intragrain pores are within a grain and particularly depicted in the closeup. Intergrain pores describe pores that are in between multiple grains.

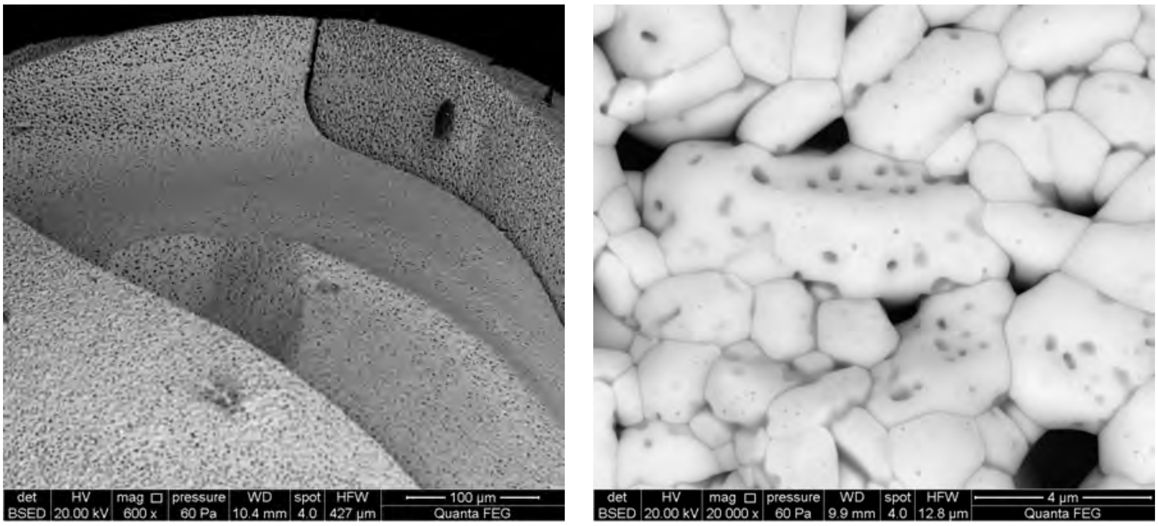

(a) 600x **(b)** 20,000x

Figure 4.19.: SEM investigations of a pure U particle treated in air at 1300 °C.

One particle of the U / Nd composition $\chi(\mathrm{Nd}) = 11.99\,\%$ showed braking edges and was used for detailed observations. An impression of the particle is given by the overview shown in Figure 4.20, (a). The porosity close to the surface is much higher then in the spheres center, which is visible in the image section shown as Figure 4.20, (b). Closeups with a magnification of 4,000x were taken from representative regions and analyzed by EDX. It figured out, that the Nd content in the center region (c) is quite high ($\chi(\mathrm{Nd}) \approx 30\,\%$). For the middle part, the region of the horizontal crack, compare image (b), was taken into account. At the bottom of the crack (d) a Nd content of $\chi(\mathrm{Nd}) \approx 4\,\%$ was found, the value, measured on the top of the crack shows only a small difference ($\chi(\mathrm{Nd}) \approx 6\,\%$). Closer to the border the Nd content increases. For the area shown in image (f) a content of $\chi(\mathrm{Nd}) \approx 8\,\%$ was determined. An inhomogeneous Nd distribution over the spheres volume is concluded.

The shape and morphology of the huge crack, crossing the particle shown in Figure 4.20, (a), indicates that the sphere broke already during the thermal treatment apart. This could explain the high $\chi(\mathrm{Nd})$ value which was determined in the center (Figure 4.20, (c)). Further particles, treated in air at 1300 °C, show higher Nd contents on the surface, which rises the assumption for a formation of Nd "layers" during calcination in air.

To investigate the Nd distribution in the U matrix in more detail, a further part of the already mentioned braking edges (Figure 4.20, (b)) was observed with an EDX mapping. The results are shown in Figure 4.21, (a) and (b). The bright area in micrographs (a) is corresponds to uranium ions, while the bright areas in image (b) belong to Nd. The assumption regarding the Nd distribution

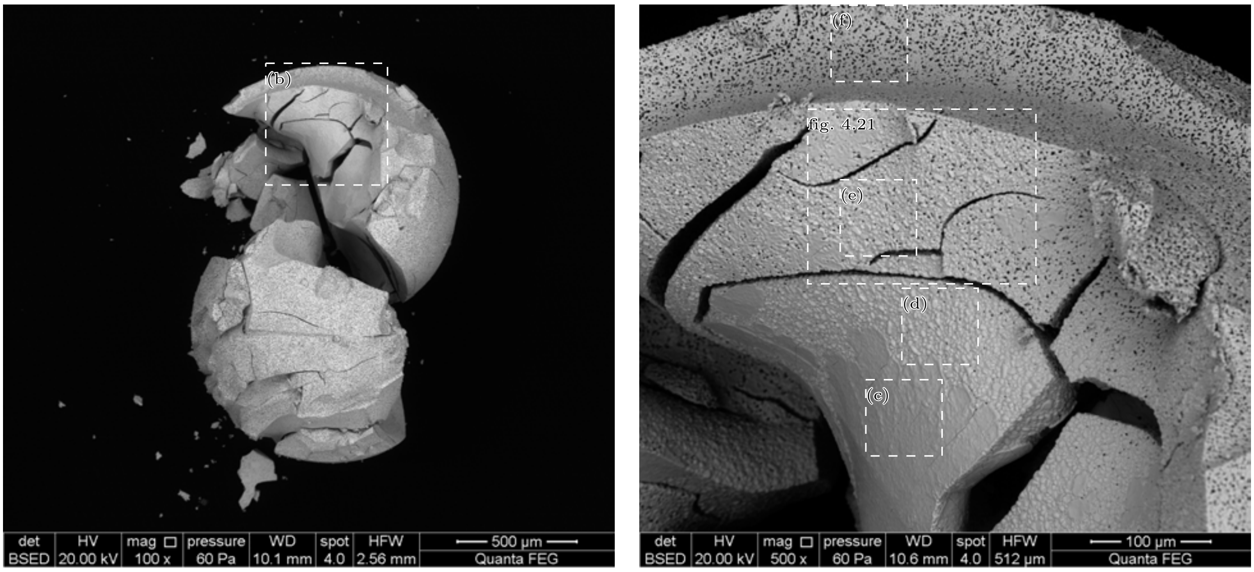

(a) 100x **(b)** 500x

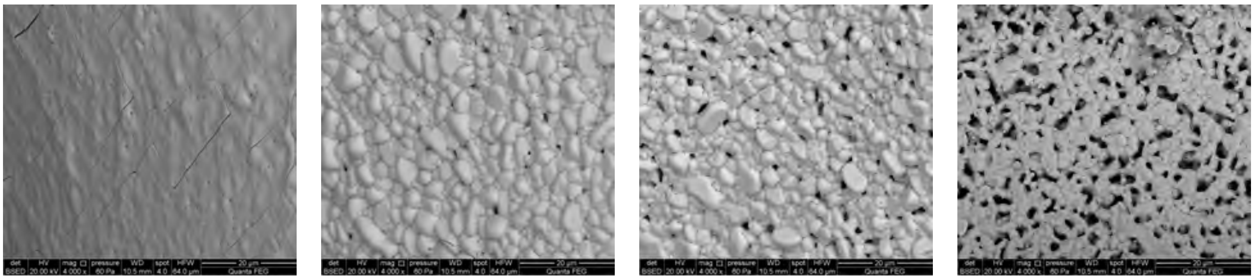

(c) 4000x **(d)** 4000x **(e)** 4000x **(f)** 4000x

Figure 4.20.: Detailed SEM analysis ($\chi(\mathrm{Nd}) = 11.99\,\%$ composition), treated in air at 1300 °C.

was proved. The Nd distribution in the uranium phase is inhomogeneous and the Nd content is quite low, an average value of $\chi(\mathrm{Nd})_{EDX} = 6.9\,\%$ for the investigated area was determined ($\chi(\mathrm{Nd})_{ICP-MS} = 11.99\,\%$).

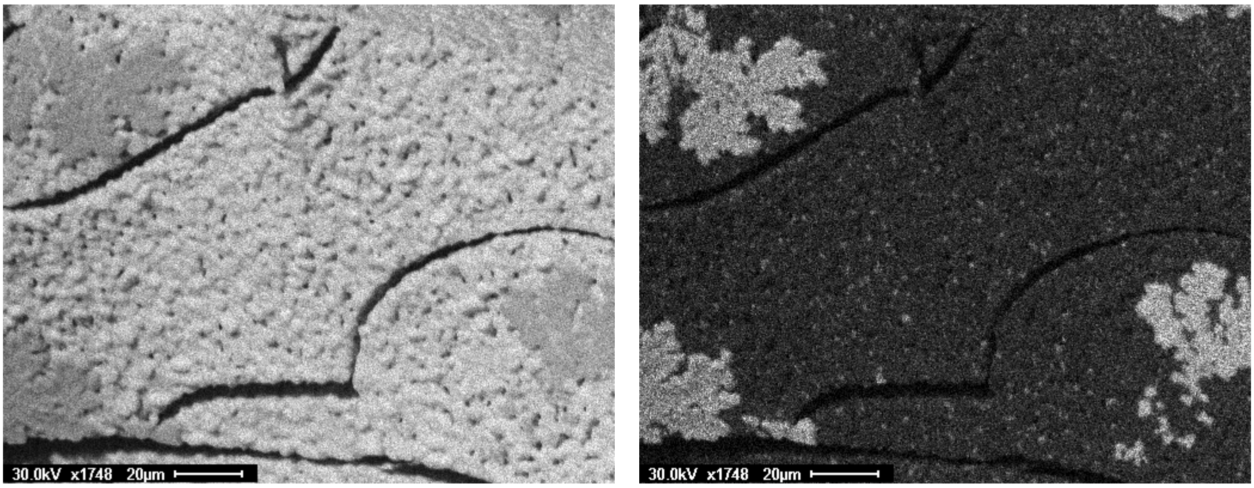

(a) U distribution **(b)** Nd distribution

Figure 4.21.: EDX mapping ($\chi(\mathrm{Nd}) = 11.99\,\%$ composition), treated in air at 1300 °C.

The Nd "layer" on the surface of some integer microspheres is exemplarily shown for a particle, belonging to the $\chi(\mathrm{Nd}) = 17.40\,\%$ composition in Figure 4.22. A 1,000 folded magnification (a) shows an overview of the Nd layer and the U phase on the particle surface, while the images (b) and (c) are closeups of the corresponding regions (8,000x). The higher Nd content for the layer was proven by EDX.

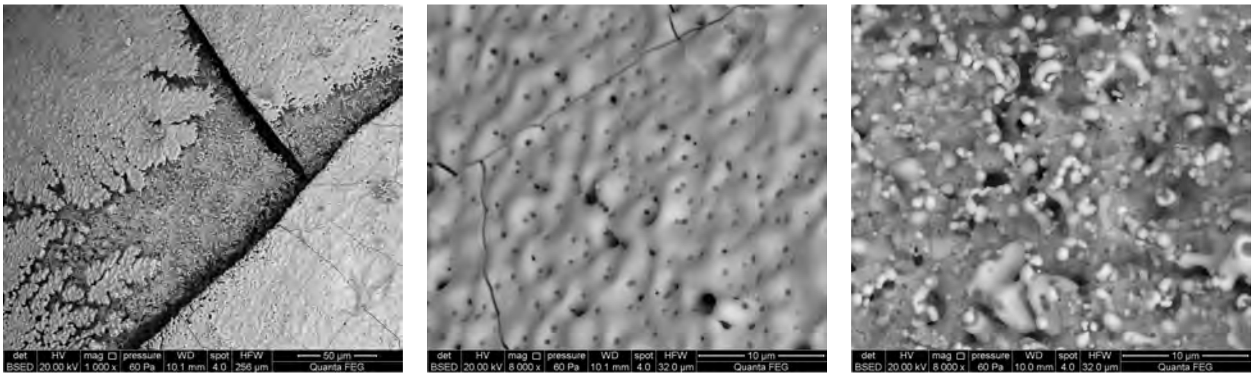

(a) overview **(b)** Nd "layer" **(c)** U phase

Figure 4.22.: Nd "layer" on a sphere ($\chi(\mathrm{Nd}) = 17.40\,\%$ composition), treated in air at 1300 °C.

Particles with higher Nd contents ($\chi(\mathrm{Nd}) \geq 33.49\,\%$) show only one U / Nd oxide phase (detailed XRD investigations following in section 4.3.1.2, p. 60). But the density difference between the spheres core and the surface, which was observed for particles containing less Nd, as well for the pure U particles, could also be recognized for this compositions. Representative micrographs belonging to a particle of the $\chi(\mathrm{Nd}) = 42.63\,\%$ composition are shown in Figure 4.23 (a) and (b). A further closeup (c) shows that only intergrain pores are existent in this microsphere. Moreover, crystal growth spirals were observed. Figure 4.23 (d) shows an example recorded with a magnification of 60,000x.

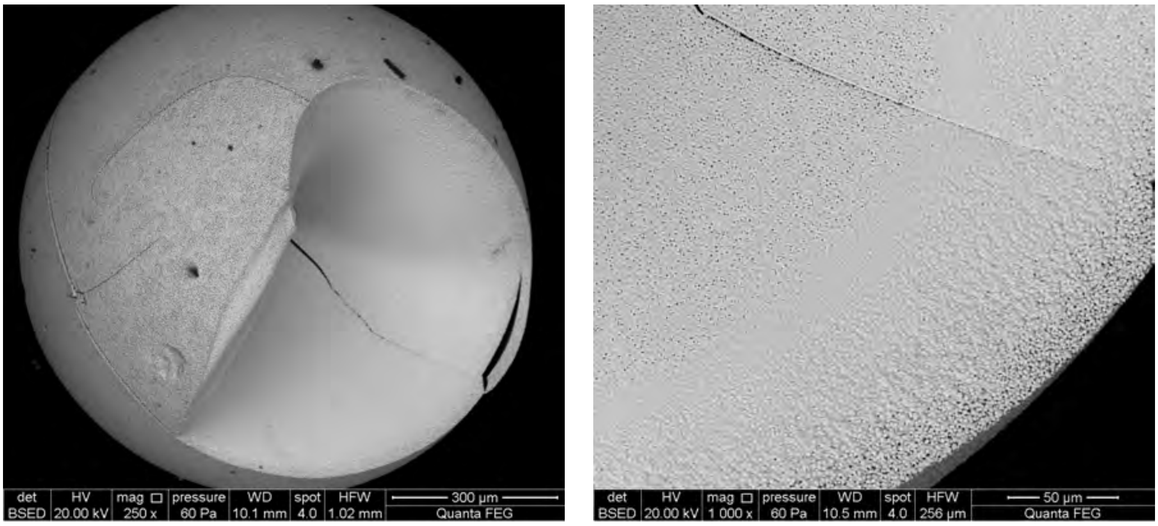

(a) 250x **(b)** 1,000x

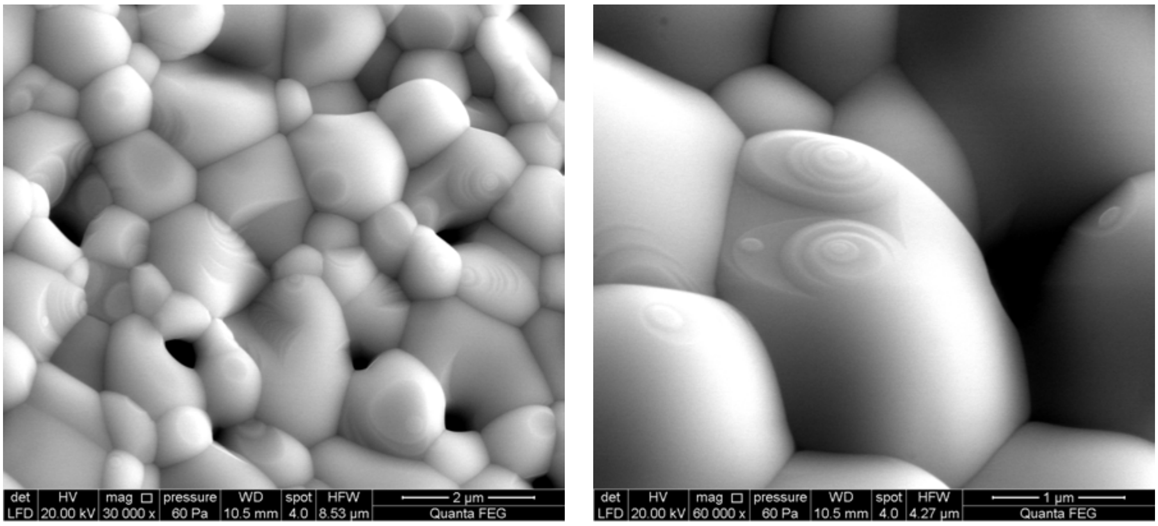

(c) 30,000x **(d)** 60,000x

Figure 4.23.: Detailed SEM analysis of a particle belonging to the $\chi(\mathrm{Nd}) = 42.63\,\%$ composition.

The EDX surface measurements of a squarish sector (magnification: 150x, Figure 4.18) on the surface of the microspheres were not performed for all particles, treated in air at 1300 °C. The analysis for two particles of the $\chi(\mathrm{Nd}) = 11.99\,\%$ composition and one particle of the $\chi(\mathrm{Nd}) = 27.59\,\%$ composition were impossible, since the particles did not show the integrity required. For the other particles the analysis were performed according to the procedure used for the green bodies. The results of this analysis are listed in Table 4.10. The Nd contents determined for the 33.49-42.63 % fraction show the same tendencies than the ICP-MS results of the green bodies. The particles with lower Nd contents behave very different. For the 5.80-22.62 % compositions the Nd content was found to be significantly higher than that of the green bodies, which underlines the formation of a Nd layer at the particles surface.

Table 4.10.: Nd content, measured at squarish sectors on the microspheres surface (treated in air at 1300 °C) by EDX.

χ(Nd) / %	$\chi(\mathrm{Nd})_{EDX,1}$ / %	$\chi(\mathrm{Nd})_{EDX,2}$ / %	$\chi(\mathrm{Nd})_{EDX,3}$ / %	$\overline{\chi}(\mathrm{Nd})_{EDX}$ / %	σ
5.80	9.94	8.84	9.13	9.30	0.57
11.99	17.27			17.27	
17.40	26.63	33.25	16.28	25.39	8.55
22.62	30.73	24.91	30.59	28.74	3.32
27.59	14.31	21.64	10.93	15.63	5.48
33.49	31.89	34.45	34.41	33.58	1.47
37.68	38.21	38.05	37.15	37.80	0.57
42.63	40.34	39.20	40.66	40.07	0.77

Furthermore, the diameter of the particles were measured in the same way than during the characterization of the green bodies. In the case of the treated particles, the mass of each observed sphere was also determined during SEM sample preparation. The determined diameters were used to calculate the volume of each observed sphere and finally its density, the results are summarized in Table 4.11.

Table 4.11.: Average mass $\overline{m}$, diameter $\overline{d}$ and density $\overline{\rho}$ of the particles treated in air at 1300 °C.

χ(Nd) / %	$\overline{m}$ / mg	σ	$\overline{d}$ / µm	σ	$\overline{\rho}$ / $\frac{\mathrm{g}}{\mathrm{cm}^3}$	σ
0.00	3.37	0.38	1110.36	37.52	5.88	0.09
5.80	3.63	1.20	1136.00	8.05	4.98	1.21
11.99	3.47	0.06	1058.14	12.81	4.52	0.04
17.40	3.53	0.40	1087.75	2.61	5.69	0.59
22.62	3.93	0.21	936.86	8.26	5.84	0.28
27.59	3.73	0.15	948.23	28.90	8.67	0.32
33.49	4.00	0.30	961.81	12.33	8.96	0.42
37.68	4.20	0.17	968.87	31.85	9.01	0.21
42.63	4.20	0.62	1029.67	41.91	8.77	0.51

Taking the determined mass loss of approximately 20 % derived from TG/DSC investigations (compare p. 51) into account, average particle masses of 3.3-4.2 mg (initially ca. 5 mg) were found. Furthermore, a decrease in diameter by approximately one-third, in comparison to the untreated particles, caused average diameters of 936-1136 µm. This lead to a significant increase of the density. The results, calculated for the green bodies were in a region of 3.8-4.2 $\frac{\mathrm{g}}{\mathrm{cm}^3}$, while the treatment in air caused average densities of 4.5-9.0 $\frac{\mathrm{g}}{\mathrm{cm}^3}$. The compositions can be split into two groups, the less Nd containing fractions (0-22.62 %) with an average density of 4.5-5.9 $\frac{\mathrm{g}}{\mathrm{cm}^3}$ and the fractions with high Nd contents. The determined density of the second group is with values of 8.7-9.0 $\frac{\mathrm{g}}{\mathrm{cm}^3}$ much higher than the one belonging to the first group. This agrees with the Nd “layers”, which were found on the surface of microspheres belonging to the first group.

4.3.1.2. XRD analysis

The treated particles were analyzed by XRD and the achieved data were standardized to an intensity of 1,000. A comparison of the X-ray diffraction pattern of all fractions treated at 1300 °C in air are shown as Figure A.1 in the appendix (p. vi). A diffraction angle range of 20-50° of the X-ray diffraction pattern for representative U / Nd compositions is summarized in Figure 4.24.

For the pure U particles an orthorhombic U_3O_8 structure was observed (Figure 4.24, (a)). For the samples with a Nd content in a range of 5.80-27.59 %, it could be investigated that two different phases were fabricated. This particles consist of the cubic $(UNd)O_2$ phase and an orthorhombic oxidic U / Nd phase (Figure 4.24, (b)). The samples with Nd amounts $\geq$ 33.49 % show only a cubic structure (Figure 4.24, (c)).

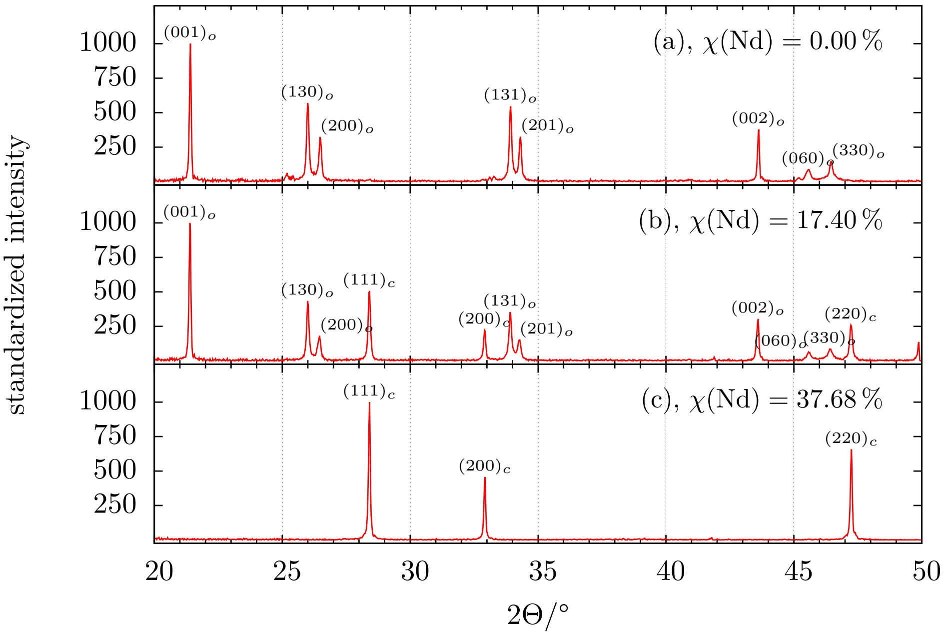

Figure 4.24.: X-ray diffraction pattern for microspheres with representative U / Nd compositions, treated at 1300 °C in air (2Θ range: 20-50°).

By the use of the intensity ratios, the content of the cubic phase to the total composition can be determined. In this work, the reflection with the maximum intensity was used for that purpose. For the orthorhombic phase the $(001)_O$ reflection was used, as described in equation 4.7. The content of the cubic phase was determined according to equation 4.8 by the use of $(111)_C$ (compare Figure 4.24). The results are plotted in Figure 4.25, the content of the cubic structure increases with higher Nd amounts in the microspheres. For particle composition with $\chi(\mathrm{Nd}) \geq 33.49\,\%$ the cubic phase was observed, only.

$$I_O = \frac{I(001)_O}{I(001)_O + I(111)_C} \tag{4.7}$$

$$I_C = \frac{I(111)_C}{I(111)_O + I(001)_C} \tag{4.8}$$

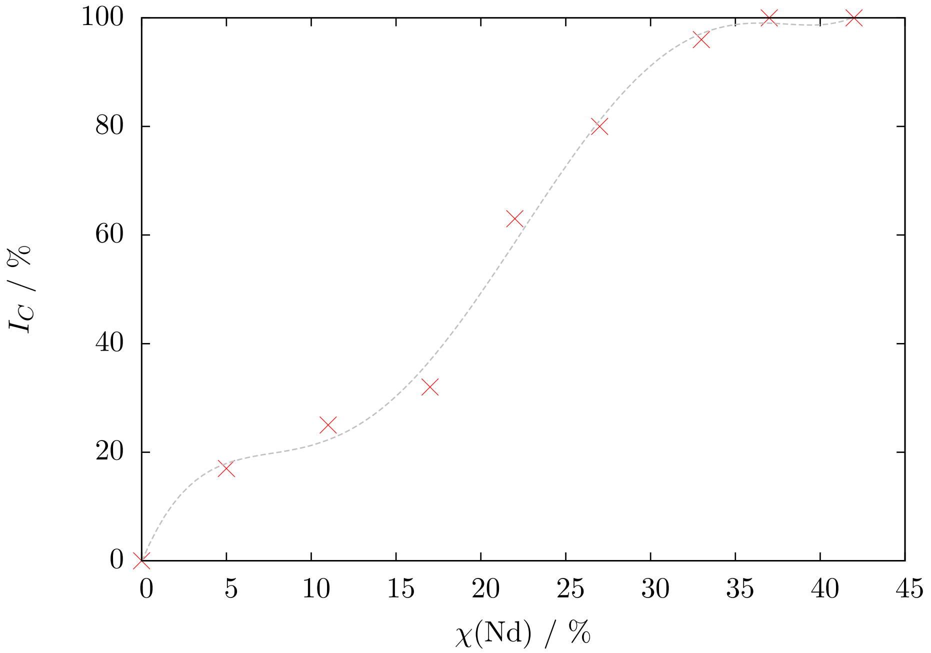

Figure 4.25.: Content of cubic phase to total composition I_C as function of χ(Nd).

Keller and Boroujerdi [33] made similar studies with the UO_2 / Nd_2O_3 system, fabricated by treatment in oxygen atmosphere. They investigated compositions treated at different temperatures (1100 °C, 1250 °C, 1400 °C and 1550 °C), and reported about a strong temperature dependency of a mixed phase region. Figure 4.26 summarizes the results obtained in this work and the results of Keller and Boroujerdi [33]. The lattice parameter a decreases with an increasing treatment temperature, a linear dependency according to Vegard's rule (equation (4.9)) was observed.

$$a_{AB} = a_A(1 - \chi_B) + a_B\chi_B \tag{4.9}$$

The region of cubic phase stability up top $\chi(\text{Nd}) = 62.5\,\%$ correlates with the phase diagram published by Lang et al. [34] and shown in Figure 4.27.

In this work, the lattice parameter was determined only for the cubic phase. Detailed investigations of the orthorhombic phase is planned for future work. The background of the used method, as well as the applied formulas, are explained in chapter 3.3.5 on page 33. The values, calculated for

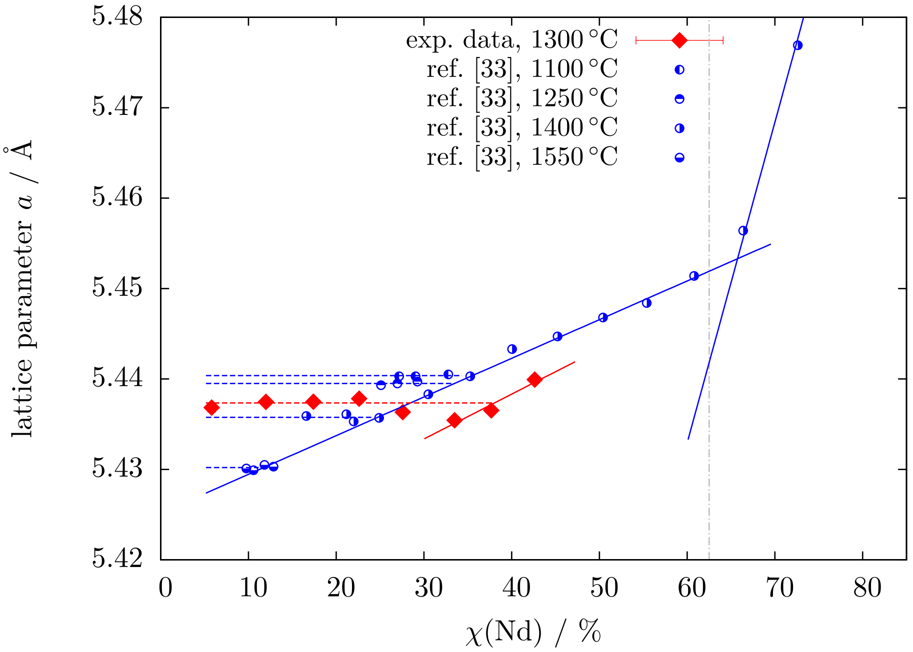

Figure 4.26.: Determined lattice parameter a as function of the Nd content in comparison with reference data of Keller and Boroujerdi [33].

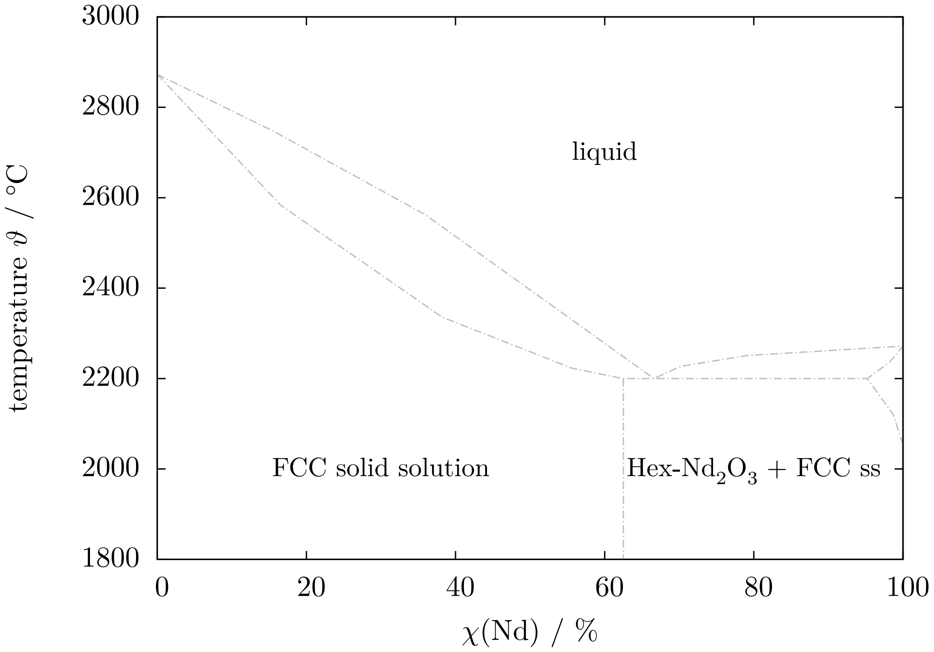

Figure 4.27.: UO_2 / Nd_2O_3 phase diagramm according to Lang et al. [34] for the 1800-3000 °C temperature range.

all investigated samples, treated in air at 1300 °C, are summarized in Table 4.12 and also presented in Figure 4.26.

The determined lattice parameter for the two phase region up to ca. 25 % Nd can be described as parallel line to the x-axis with $a \approx 5.4374$ Å. This is a similar behavior than the one described by Keller and Boroujerdi [33]. The interception point of the horizontal line, belonging to the U / Nd particles treated in air at 1300 °C, match very well between the published data for the treatment temperatures of 1250 °C and 1400 °C.

The last three experimental points correspond to the one phase region and show a linear dependency with a positive slope (Figure 4.26). A similar slope than the one belonging to the published data [33] was found, but the function is shifted to the right. This shift can be caused by the air atmosphere which was achieved during the thermal treatment of the U / Nd microspheres, while the data published by Keller and Boroujerdi [33] were determined from compositions treated in an pure oxygen atmosphere.

Furthermore the mean crystal size and the lattice distortion were determined by the Hall-Williamson method, which is explained in chapter 3.3.5 on page 33. The results are summarized as function of the Nd content in Figure 4.28 and listed in Table 4.12. A linear behavior of the mean crystal size L was determined. The value of L decreases with an increasing Nd amount in the particles. The lattice distortion $< \epsilon^2 >^{0.5}$ shows also a decrease with increasing χ(Nd). The determined $< \epsilon^2 >^{0.5}$ value for two phase region ($\chi(\mathrm{Nd}) \leq 27.59\,\%$) decreases moderately. For the one phase region a significantly decrease to almost zero was observed.

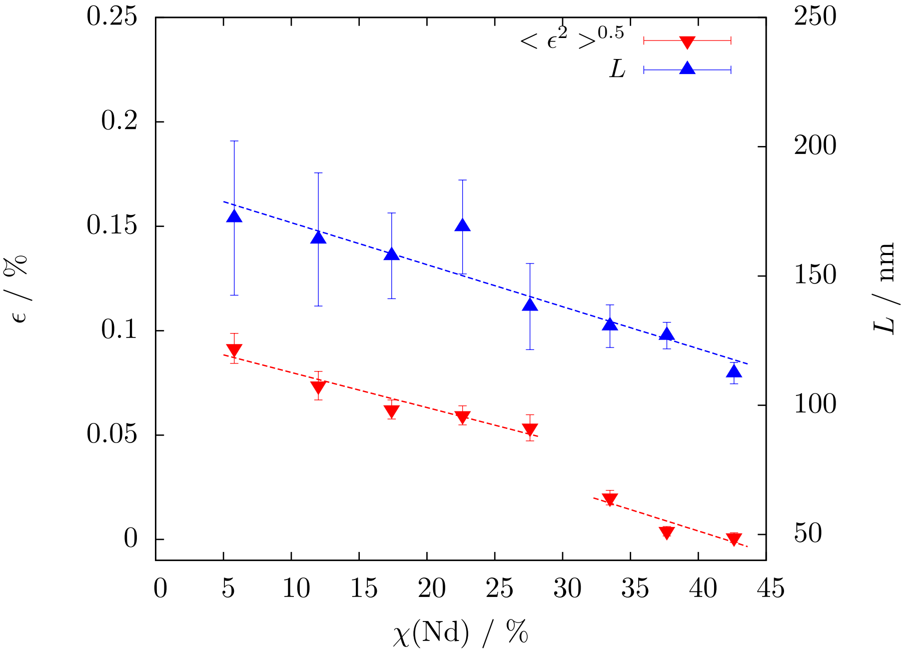

Figure 4.28.: Mean crystal size L and lattice distortion $< \epsilon^2 >^{0.5}$ vs. Nd content (particles, treated in air at 1300 °C).

Table 4.12.: Results of XRD analysis of particles, treated in air, at 1300 °C.

χ(Nd) / %	a / Å	da / Å	L / nm	dL / nm	ϵ / %	$d\epsilon$ / %
5.80	5.4368	0.0005	172.40	29.85	0.0915	0.0072
11.99	5.4375	0.0005	164.14	25.76	0.0737	0.0069
17.40	5.4375	0.0002	157.78	16.58	0.0623	0.0046
22.62	5.4378	0.0001	168.95	18.14	0.0594	0.0046
27.59	5.4363	0.0001	138.15	16.66	0.0535	0.0063
33.49	5.4354	0.0001	130.58	8.27	0.0200	0.0035
37.68	5.4365	0.0001	126.94	5.11	0.0040	0.0023
42.63	5.4399	0.0003	112.41	4.12	0.0009	0.0023

4.3.2. Characterization of particles treated in H_2:Ar

4.3.2.1. SEM/EDX analysis

The microspheres treated in reducing H_2:Ar atmosphere at 1300 °C were observed by SEM. One representative particle of each composition is shown with a magnification of 150x in Figure 4.29. An integrity spherical shape can be observed for the U / Nd compositions with $\chi(\mathrm{Nd}) \leq 17.40\,\%$. The presented SEM images of the microspheres show a uniform color distribution, which leads to the assumption of a homogeneous Nd spreading over the particle surface. Neodymium “layers”, like the particles treated in air showed, could not be observed for these samples.

A cross section of a particle ($\chi(\mathrm{Nd}) = 5.80\,\%$) that broke apart was investigated more in detail. Figure 4.30 (a) shows that the uniform color distribution is valid for the center of the sphere as well, but some kind of inner core was observed. This may be caused by an incomplete gelation. The image was taken with a magnification of 200x. EDX analysis of the particles center and border were performed with a magnification of 4,000x. The observed areas are shown in Figure 4.30 (b) and (c). It figured out that the Nd distribution is quite homogeneous. In the middle of the particle (b) a Nd content of $\chi(\mathrm{Nd}) = 6.4\,\%$ could be determined, while the Nd content at the border is $\chi(\mathrm{Nd}) = 6.6\,\%$ (c). Moreover the observed particle was almost free of pores and occurs quite dense.

The other fabricated particle compositions showed also almost no pores. A micrograph, taken from the surface of a particle belonging to the $\chi(\mathrm{Nd}) = 11.99\,\%$ composition is emphasizes a homogeneous Nd distribution. A further closeup was used to measure 10 random grain sizes. Picture (a) of Figure 4.31 shows this surface with a magnification of 4,000x. Grains from picture (b) (magnification 60,000x) were taken to perform the grain size measurements. The same area is shown as (c), recorded with the LFD detector. The determined grain sizes are in a range of 44.3-242.2 nm. Two grains match between 44.3-138.6 nm, while 6 are in a range of 207.4-242.2 nm. During this analysis, no intragrain pores were found in the observed microsphere.

The shown images are representative for all observed and prepared U / Nd compositions. On some particles impurities, see Figure 4.32, (a) (magnification 500x), were evident on the surface. This “ring” occurs independent on Nd content of the microspheres. Image (b) shows the border of the darker ring with a magnification of 4,000x. EDX measurements showed a Nd content of 91 %,

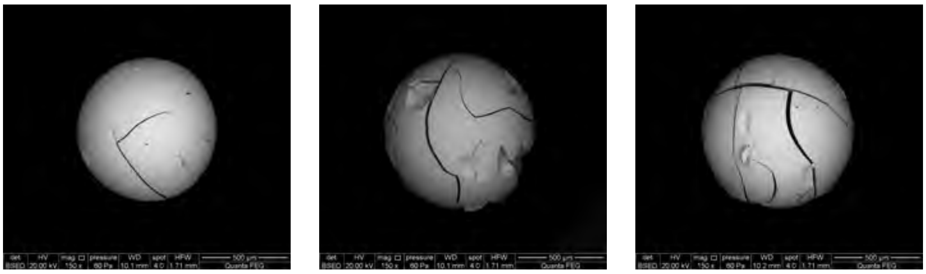

(a) χ(Nd)=0.00 % **(b)** χ(Nd)=5.80 % **(c)** χ(Nd)=11.99 %

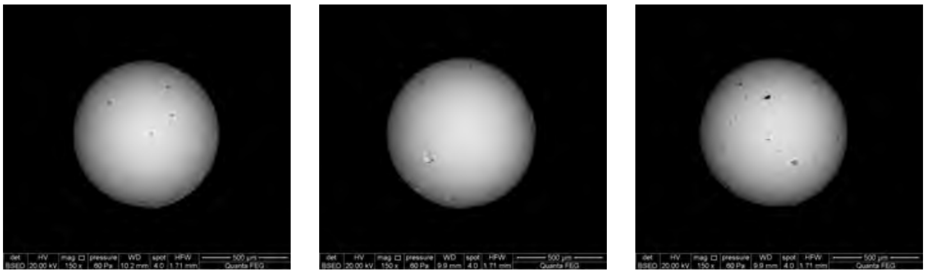

(d) χ(Nd)=17.40 % **(e)** χ(Nd)=22.62 % **(f)** χ(Nd)=27.59 %

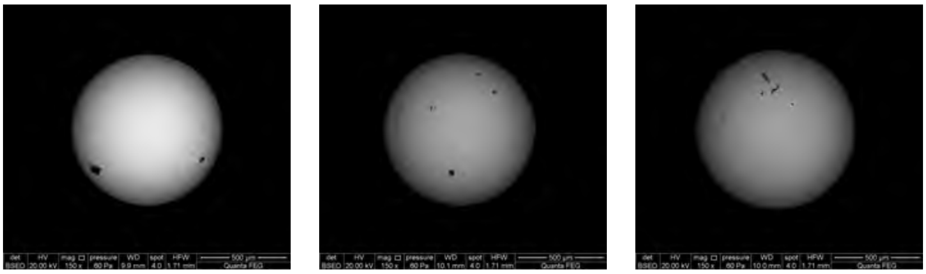

(g) χ(Nd)=33.49 % **(h)** χ(Nd)=37.68 % **(i)** χ(Nd)=42.63 %

Figure 4.29.: Microspheres treated at 1300 °C in H_2:Ar during SEM analysis.

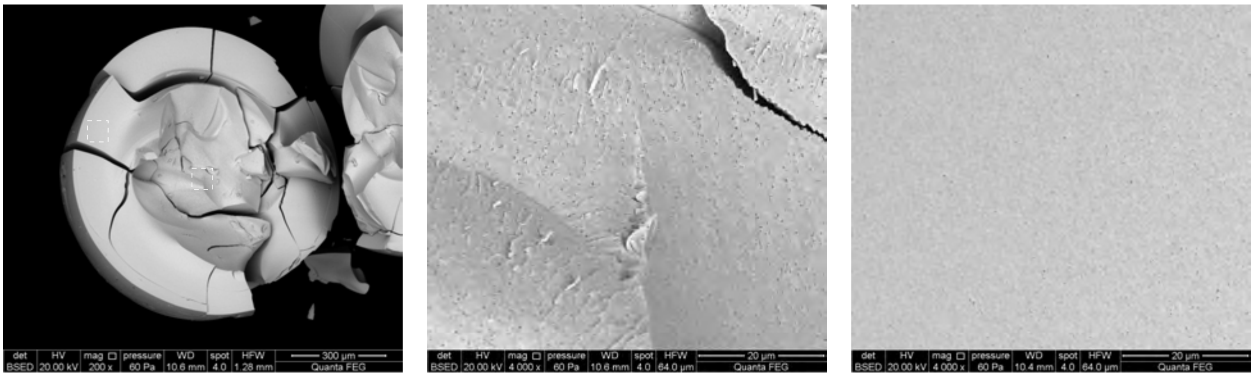

(a) 200x **(b)** center, 4,000x **(c)** border, 4,000x

Figure 4.30.: SEM cross section pictures (χ(Nd) = 5.80 %).

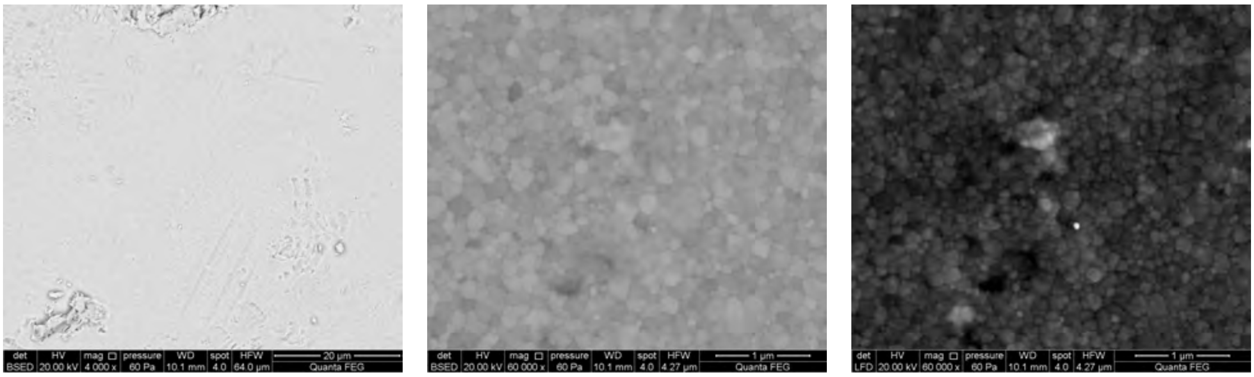

(a) surface **(b)** BSED **(c)** LFD

Figure 4.31.: SEM pictures of grains (χ(Nd) = 11.99 %).

while the bright inner area, shown in micrograph (c) (magnification 16,000x) contains 22 % Nd. The dark spots in the middle of the ring were determined as Al_2O_3. A reaction of the Al_2O_3 containing crucible and the particle during thermal treatment suggest itself.

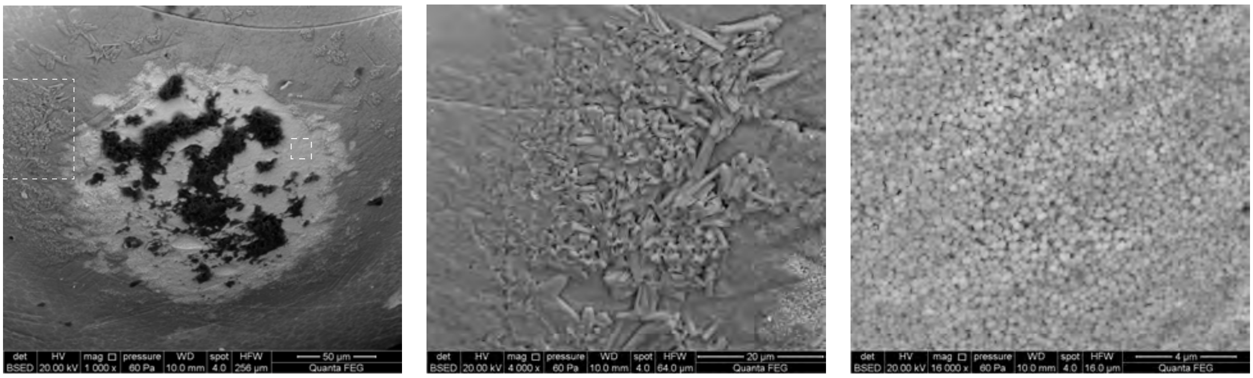

(a) 1,000x **(b)** dark ring, 4,000x **(c)** bright inner 16,000x

Figure 4.32.: SEM pictures surface impurities (χ(Nd) = 27.59 %).

The surface of each observed sphere was analyzed by EDX and the Nd content was estimated. The analysis were done for all fractions and performed in the same way than the analysis of the green bodies. An average Nd content per fraction was calculated ($\overline{\chi}(\mathrm{Nd})_{EDX}$), the results of this analyzes are listed in Table 4.13. The discrepancies which were achieved for some spheres lead to the partially high standard deviation. This can be caused by some of the formerly shown effects. The “ring”, which was found on some spheres surfaces (compare Figure 4.32, (b)) contained large quantities of Nd, which has a huge influence on the measurement. This phenomenon was mainly observed for particles containing higher Nd ratios and could explain the oultiner in the χ(Nd) = 33.49 % fraction. Generally it can be observed that the particles partially behave quite different than the others belonging to the same fraction.

Table 4.13.: Nd content of spheres, treated in H_2:Ar at 1300 °C, determined by EDX.

χ(Nd) / %	$\chi(\mathrm{Nd})_{EDX,1}$ / %	$\chi(\mathrm{Nd})_{EDX,2}$ / %	$\chi(\mathrm{Nd})_{EDX,3}$ / %	$\overline{\chi}(\mathrm{Nd})_{EDX}$ / %	σ
5.80	5.54	5.43	5.24	5.40	0.15
11.99	11.43	12.77	15.03	13.08	1.82
17.40	18.56	25.88	28.26	24.23	5.06
22.62	26.2	22.56	24.82	24.53	1.84
27.59	28.64	28.85	24.36	27.28	2.53
33.49	46.16	31.24	32.73	36.71	8.22
37.68	43.72	38.53	36.66	39.64	3.66
42.63	46.02	45.46	47.06	46.18	0.81

Furthermore, the density of these particles was calculated following the procedure that has been described previously. The results are summarized in Table 4.14.

Table 4.14.: Average diameter, mass and density of spheres, treated in H_2:Ar at 1300 °C, based on SEM analysis.

χ(Nd) / %	$\overline{m}$ / mg	σ	$\overline{d}$ / µm	σ	$\overline{\rho}$ / $\frac{\mathrm{g}}{\mathrm{cm}^3}$	σ
0	3.37	0.12	932.18	27.55	11.45	1.07
5.80	3.50	0.70	908.95	9.63	8.19	0.90
11.99	3.43	1.16	861.47	8.90	8.73	2.94
17.40	3.73	0.38	879.66	6.99	11.13	0.80
22.62	3.90	0.10	870.95	10.69	10.94	0.16
27.59	3.83	0.12	893.72	21.32	11.09	0.61
33.49	3.93	0.50	916.11	18.07	10.48	0.61
37.68	4.13	0.29	916.30	26.90	10.26	0.42
42.63	4.23	0.40	826.08	27.04	10.49	0.07

A comparable average mass of the particle fractions to the one for spheres treated in air atmosphere was found. This was due to the similar mass loss expected. The shrinkage during a treatment in H_2:Ar atmosphere is higher compared to the treatment in air. Average diameters in the range of 826-932 µm were determined. This leads to a significant increase of the density. The results, calculated for the green bodies were in a region of 3.8-4.2 $\frac{\mathrm{g}}{\mathrm{cm}^3}$, while the treatment in reducing H_2:Ar atmosphere caused average densities of 8.2-11.5 $\frac{\mathrm{g}}{\mathrm{cm}^3}$. Taking the deviation caused by the weighing and diameter measurement into account, this result is in accordance with the UO_2 literature density of 10.97 $\frac{\mathrm{g}}{\mathrm{cm}^3}$.

4.3.2.2. XRD analysis

The X-ray diffraction pattern of all fractions, treated in H_2:Ar at 1300 °C, show the same reflexes (Figure A.2, p. vii). The distribution of the reflexes indicate a cubic lattice structure of the samples. At higher diffraction angles, a decreasing intensity with higher Nd content was observed. All data underwent the same analysis.

The results of all compositions are summarized in a plot, which is shown as Figure 4.33. The lattice parameter belonging to particles with a Nd content up to 27 % behave linear. For higher Nd contents a more or less constant value of approximately $a = 5.4595$ Å was analyzed.

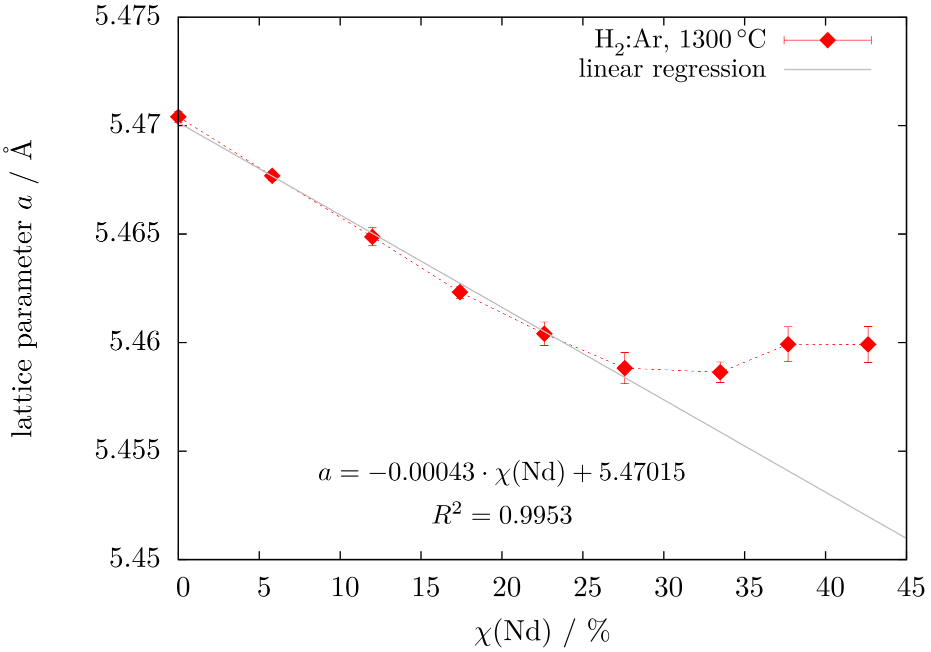

Figure 4.33.: Determined lattice parameter a as function of the Nd content (particles, treated in reducing H_2:Ar atmosphere at 1300 °C).

With respect to Vegard's rule, shown in equation (4.9) on page 61, a linear behavior should be expected. A fit based on the lattice parameters, estimated for the linear behaving region, was generated and is also plotted in Figure 4.33. A possible reasons for this unexpected behavior could be high degree of microdeformation. Further analysis were performed, to estimate the lattice distortion $< \epsilon^2 >^{0.5}$, as well as the mean crystal size.

The mean crystal size L and the lattice distortion $< \epsilon^2 >^{0.5}$ were determined by the use of the Hall-Williamson method, which is explained in chapter 3.3.5 on page 33. The linear regressions which had to be generated to get these parameters are exemplarily shown for some particle compositions in Figure 4.34.

A significant change in the regressions slope at high Nd concentrations can be recognized. For pure uranium spheres and the fractions with low neodymium content the slope is close to zero, whereas particles containing high amounts of neodymium cause a large positive slope. Due to the fact that the mean crystal size L and lattice distortion $< \epsilon^2 >^{0.5}$ are proportional to these values,

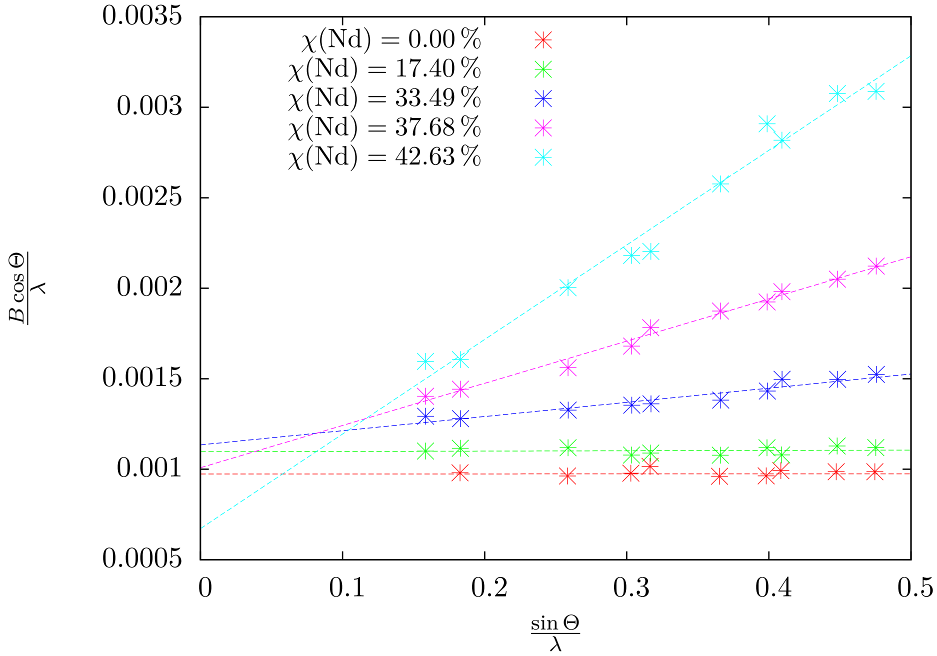

Figure 4.34.: Mean crystal size L and lattice distortion $< \epsilon^2 >^{0.5}$ determination by the use of Hall-Williamson method (particles, treated in reducing H_2:Ar atmosphere at 1300 °C).

they behave equal. Figure 4.35 shows the results of the Hall-Williamson analysis of all particle fractions.

The degree of microdeformation ϵ can also be estimated by another way. Assuming a linear behavior with respect to Vegard's rule (compare regression in Figure 4.33), the deviation to the experimental data represents the lattice distortion. The value of microdeformation (ϵ) can be described as the relation, shown in equation (4.10), where a_{calc} is corresponding to the lattice parameter according to Vegard's rule and a describes the experimental data point.

$$\epsilon = \frac{a_{calc} - a}{a_{calc}} \tag{4.10}$$

On the base of the determined results, it can be assumed, that an increase of the lattice parameter a causes an increase of the microdeformation ϵ, like it was found for the compositions with high Nd contents. A reasonable explanation could be a difficult homogeneous distribution of the Nd atoms in the crystal lattice at high Nd contents. A higher treatment temperature as well as a longer sintering time would increase the material diffusion and would maybe lead to results with a more homogeneous Nd distribution.

The result (ϵ) is an expression for the percentage deviation to the expected lattice parameter and can be compared with the $< \epsilon^2 >^{0.5}$ value, got by the Hall-Williamson analysis. This comparison is plotted as Figure 4.36. Within the degree of uncertainty the same behavior can be observed.

The results of the XRD data analysis for the particles treated in H_2:Ar at 1300°C are summarized in Table 4.15.

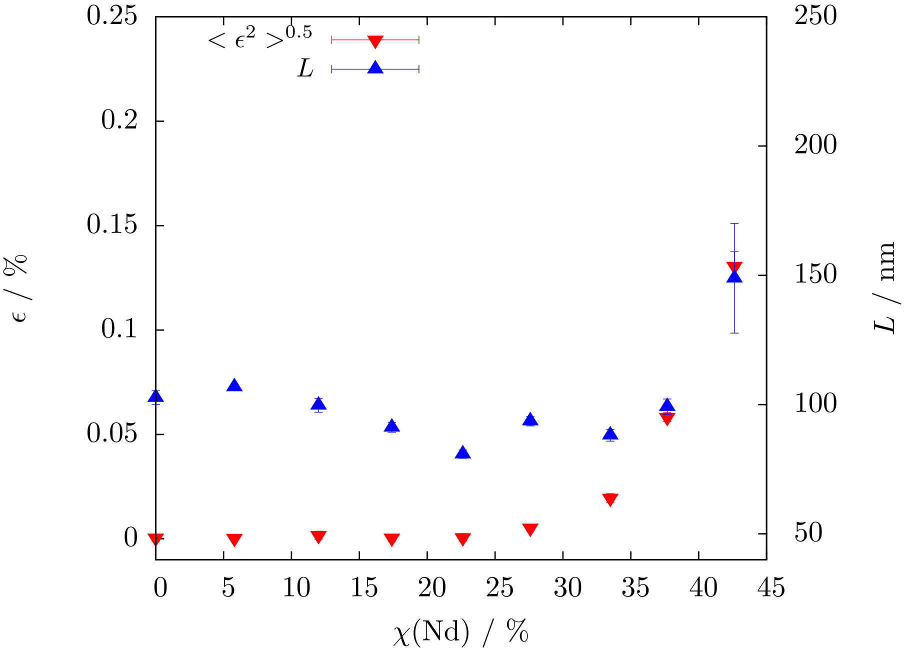

Figure 4.35.: Mean crystal size L and lattice distortion $< \epsilon^2 >^{0.5}$ as a function of χ(Nd) (particles treated in reducing atmosphere at 1300 °C).

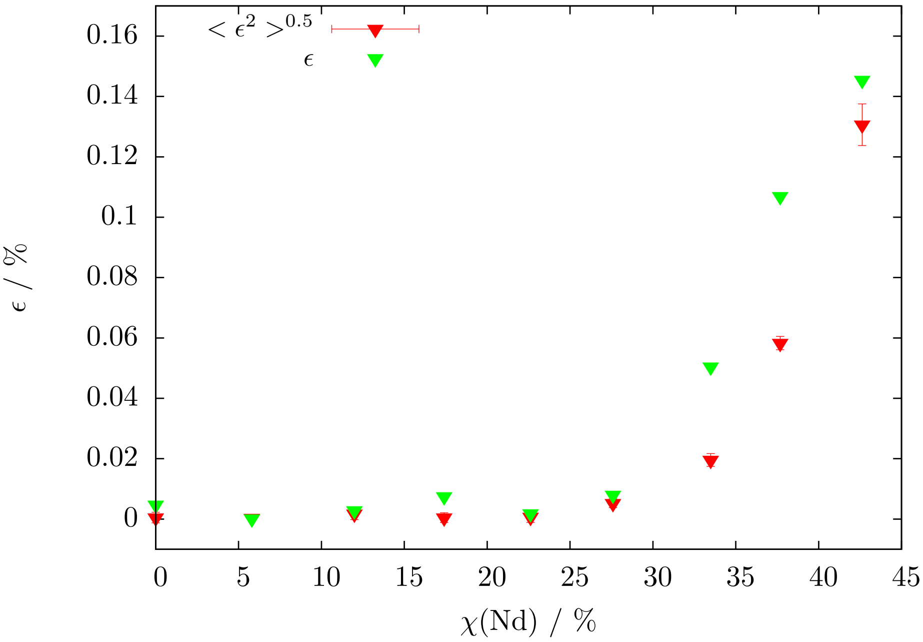

Figure 4.36.: Lattice deformation $< \epsilon^2 >^{0.5}$ and ϵ as function of χ(Nd) (particles treated in reducing atmosphere at 1300 °C).

Table 4.15.: Results of XRD analysis of particles, treated in H_2:Ar, at 1300°C.

χ(Nd) / %	a / Å	da / Å	L / nm	dL / nm	ϵ / %	$d\epsilon$ / %	a_{cal} / Å	$\frac{da}{a_{cal}}$ / %
0	5.4704	0.0003	102.69	2.64	0.0005	0.0017	5.4701	0.0047
5.80	5.4677	0.0002	106.78	0.90	0.0004	0.0006	5.4677	0.0002
11.99	5.4649	0.0004	99.68	2.65	0.0017	0.0019	5.4650	0.0029
17.40	5.4623	0.0003	91.19	1.89	0.0005	0.0016	5.4627	0.0075
22.62	5.4604	0.0005	80.82	1.63	0.0007	0.0018	5.4605	0.0018
27.59	5.4588	0.0007	93.59	1.84	0.0053	0.0014	5.4584	0.0080
33.49	5.4586	0.0005	88.13	2.29	0.0196	0.0021	5.4559	0.0505
37.68	5.4599	0.0008	99.14	3.01	0.0583	0.0022	5.4541	0.1069
42.63	5.4599	0.0008	148.84	21.20	0.1307	0.0069	5.4520	0.1455

4.4. Comparison of particles and powders

The X-ray diffraction pattern, got for the treated powders in reducing H_2:Ar atmosphere (appendix, Figure A.3 p. viii), are in good agreement with the results of the particles. The powder compositions with a Nd content of 6.60 %, and the mixtures with high Nd contents (31.28 %, 36.16 %, 42.33 % and 46.99 %) show one cubic phase. For this compositions, the X-ray reflections could be fitted with a Gaussian function (Figure 4.37).

The data analysis was performed in the same way than for the results of the particles. During the detailed data analysis, it figured out that the peak shape of the reflexes belonging to some fractions (13.03 %, 20.20 % and 26.43 %), could better be fitted by the use of two Gaussian functions, indicating the evidence of a second phase. An example for the reflex found at a diffraction angle range of 77.9-78.5° for representative fractions are shown in Figure 4.37. Detailed investigations showed a cubic lattice structure of both phases. Based on this results it can be concluded that two cubic phases for some powder fractions are present. The determined intensities of the two Gaussian functions were used to calculate the content of phase 1 according to formula (4.11).

$$I_{phase1} = \frac{I_{phase1}}{I_{phase1} + I_{phase2}} \tag{4.11}$$

A more or less constant ratio of phase 1 to the sum of phase 1 and phase 2 was investigated for the whole 2Θ range, the result of the powders with two phases are shown as Figure 4.38. An average phase 1 content of 35.3 % was determined for the $\chi(\mathrm{Nd}) = 13.03\,\%$ composition. For the powder fraction containing 20.20 % Nd, an average phase 1 content of 20.9 % was calculated. A further decrease to an average phase 1 content of 17.0 %, for the powder fraction containing 26.43 % Nd, was observed.

The determination of the lattice parameter a was done in the common way and is plotted in Figure 4.39. For the powders, where two cubic phases were observed, two a values were calculated, respectively. The cyan symbol in Figure 4.39 indicates phase 1, observed in the powder compositions,

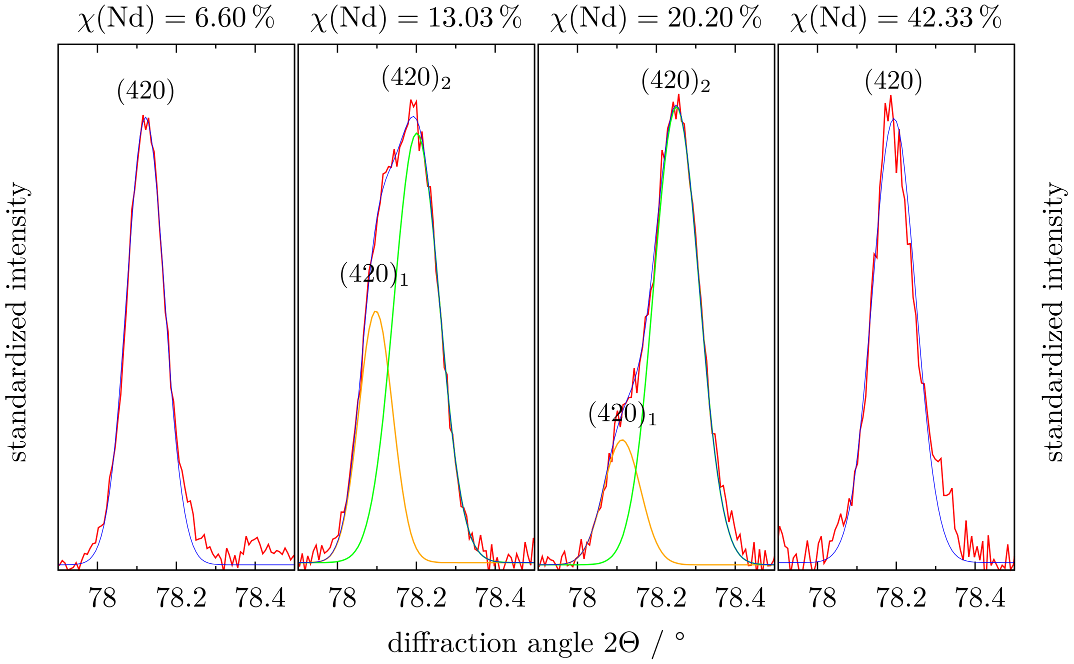

Figure 4.37.: Fitting of reflex (420) with one and two Gaussian functions (powder fractions, treated in reducing atmosphere at 1300 °C).

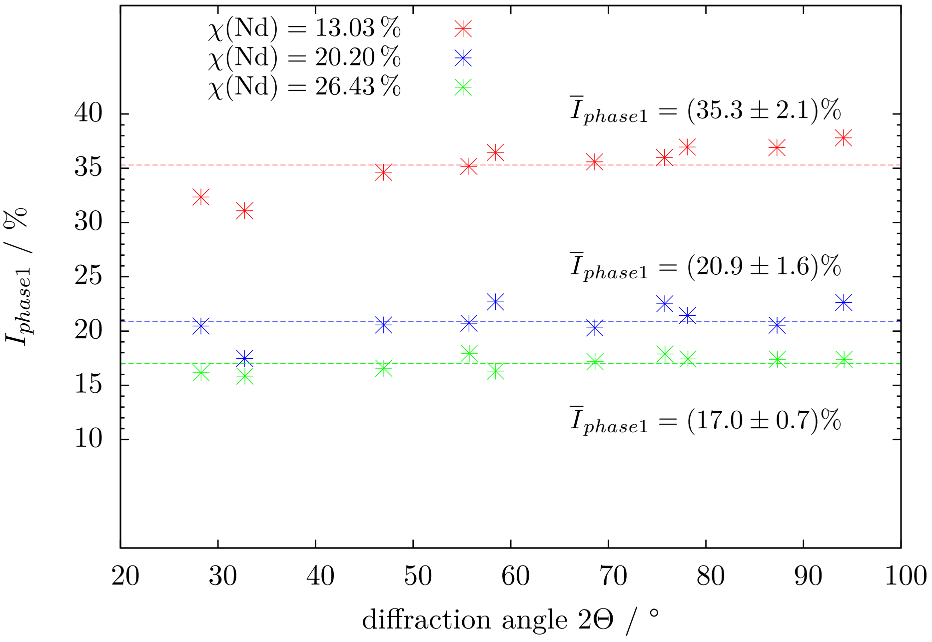

Figure 4.38.: Content of phase 1 as function of 2Θ.

while phase 2 is symbolized by the violet one. The two phases show a big difference in the a value. Further detailed studies were performed. By the use of the determined average phase 1 content, an average lattice parameter $\overline{a}$ was calculated according to equation (4.12).

$$\overline{a} = I_{phase1} \cdot a_{phase1} + (1 - I_{phase1}) \cdot a_{phase2} \tag{4.12}$$

The average lattice parameters for the two phase compositions (13.03 %, 20.20 % and 26.43 % Nd content) are also shown in Figure 4.39 and indicated by the orange symbol. The determined point for the $\chi(\mathrm{Nd}) = 6.60\,\%$ composition and the calculated average values of the two phase mixtures behave linear. A correlation of 0.9924 was determined by a linear regression.

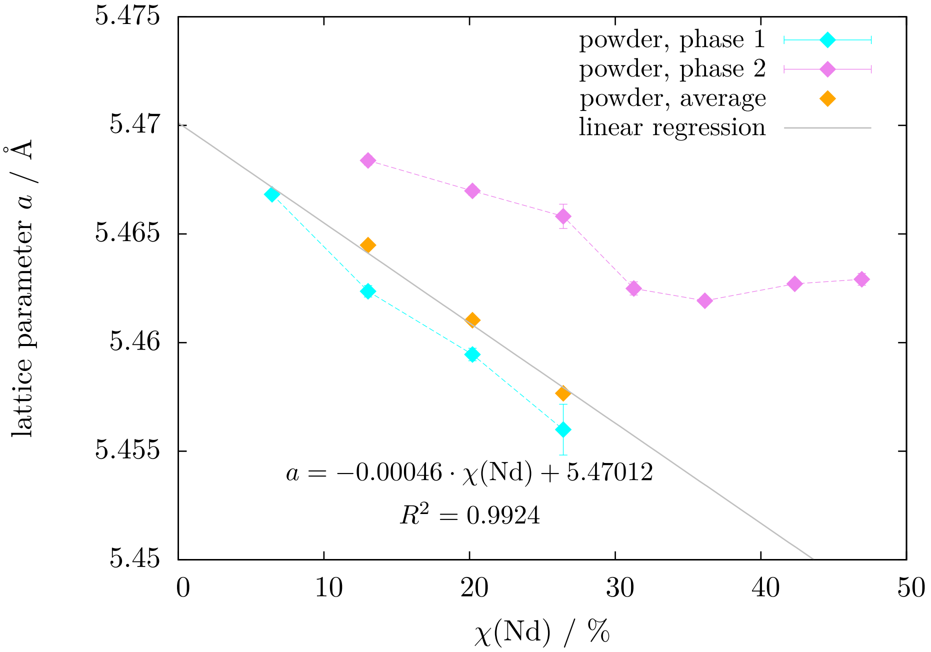

Figure 4.39.: Determined lattice parameter a as function of the Nd content (powders, treated in reducing H_2:Ar atmosphere at 1300 °C).

The determined lattice parameter for compositions with Nd contents ≥ 31.28 % show a linear dependency with a more or less constant a value of 5.4625 Å, similar like the observed behavior of the microspheres treated in reducing H_2:Ar atmosphere at 1300 °C. A comparison of the lattice parameter a, determined for powders and particles (treated in reducing H_2:Ar atmosphere at 1300 °C), was done and is summarized in Figure 4.40. The characteristic of the powder is quite similar than the observed one for the particles. The calculated average $\overline{a}$ values for the powders match very well to the linear behaving region of the values, determined for the particle.

During the discussion about the results of the lattice parameter determination of the microspheres (section 4.3.2.2, p. 68), the assumption of a high degree of microdeformation ϵ in the crystal lattice, causing this behavior, came up. The three U / Nd particle compositions with the highest Nd contents (33.49 %, 37.68 % and 42.63 %) were treated at 1600 °C for 5 hours in the reducing H_2:Ar atmosphere to prove this assumption. XRD analysis of the resulting particles were performed and the lattice parameter a was calculated (5.4552 Å, 5.4535 Å and 5.4517 Å). This experimental data are presented in Figure 4.40 and indicated by the blue symbols. The resulted lattice parameter decreased and correspond to the expected linear dependency.

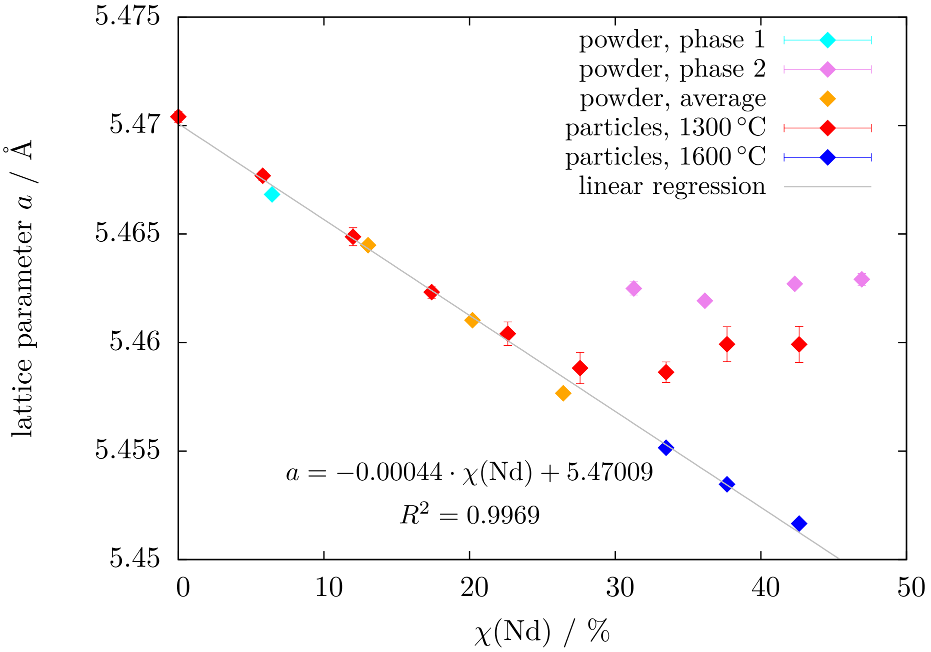

Figure 4.40.: Comparison of determined lattice parameter a vs. Nd content (powders and particles, treated in reducing H_2:Ar atmosphere at 1300 °C and 1600 °C).

The powders treated at 1300 °C (average a values) and the particles treated at 1300 °C and 1600 °C in H_2:Ar atmosphere can be fitted by a linear function. It can be concluded that Vegard's rule is valid for the UO_2 / Nd_2O_3 binary system. The value of a decreases linearly with an increasing Nd content in the composition, which is caused by the addition of Nd_2O_3 in the UO_2 matrix. The exchange of U^{4+} cations ($radius = 1.00$ Å, [35]) with the smaller Nd^{3+} cations ($radius = 0.983$ Å, [35]) takes place.

The Hall-Williamson method was applied and the mean crystal size L and lattice distortion $< \epsilon^2 >^{0.5}$ were calculated. For the two phase region average $\overline{L}$ and $\overline{< \epsilon^2 >^{0.5}}$ were calculated in the way like the average lattice parameter $\overline{a}$ was generated. The results of these analysis are shown as function of χ(Nd) in Figure 4.41. A decrease of L and $< \epsilon^2 >^{0.5}$ with an increasing χ(Nd) content can be observed.

The XRD results for the powders treated in reducing H_2:Ar atmosphere at 1300 °C are summarized in Table 4.16.

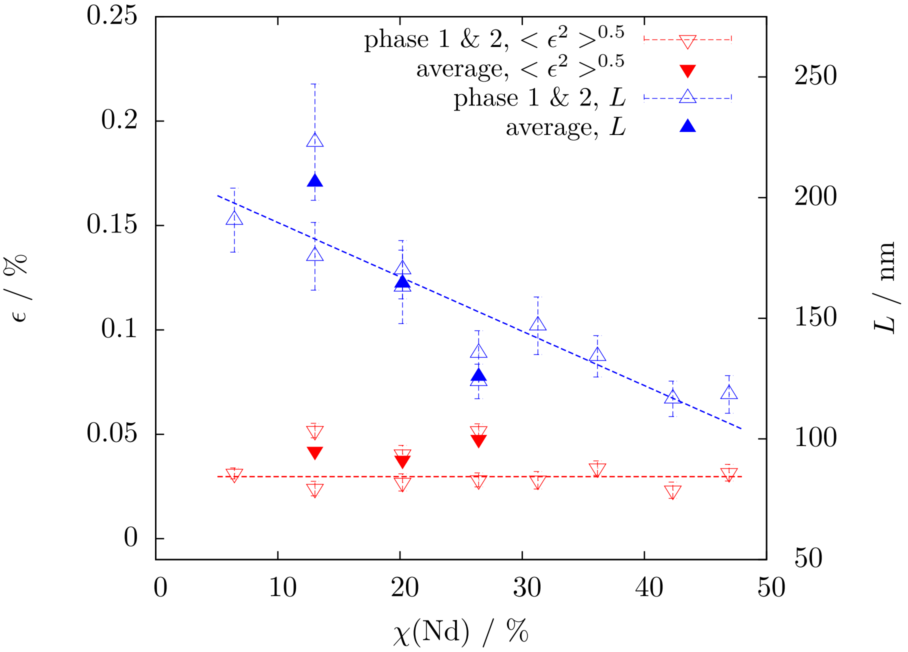

Figure 4.41.: Mean crystal size L and lattice distortion $< \epsilon^2 >^{0.5}$ vs. Nd content (powders, treated in reducing H_2:Ar atmosphere at 1300 °C).

Table 4.16.: Results of XRD analysis of powders, treated in H_2:Ar, at 1300°C.

χ(Nd) / %	a / Å	da / Å	L / nm	dL / nm	ϵ / %	$d\epsilon$ / %	a_{cal} / Å	$\frac{da}{a_{cal}}$ / %
6.44	5.4668	0.0002	190.68	13.26	0.0312	0.0026	5.4674	0.0105
13.03	5.4624	0.0003	222.97	24.10	0.0518	0.0035	5.4646	0.0409
20.20	5.4595	0.0003	162.99	15.22	0.0405	0.0041	5.4615	0.0382
26.43	5.4560	0.0012	123.82	7.16	0.0516	0.0034	5.4589	0.0530
31.28	5.4625	0.0003	146.89	11.92	0.0280	0.0042	5.4568	0.1039
36.16	5.4619	0.0001	134.25	8.58	0.0338	0.0034	5.4547	0.1318
42.33	5.4627	0.0002	116.60	7.35	0.0232	0.0039	5.4521	0.1942
46.93	5.4629	0.0003	118.43	7.77	0.0316	0.0040	5.4502	0.2341
13.03	5.4684	0.0002	175.69	14.05	0.0240	0.0035	add. phase	
20.20	5.4670	0.0002	170.13	12.06	0.0269	0.0041		
26.43	5.4658	0.0006	135.56	9.29	0.0282	0.0034		
13.03	5.4645		206.28		0.0420		average	
20.20	5.4610		164.48		0.0377			
26.43	5.4577		125.82		0.0476			

The data of this work and a summary of reference data are presented in Figure 4.42. Data for pure UO_2 were taken from *PDF-2* database provided by *International Centre for Diffraction Data* (ICDD) [36]. The data achieved in this work are symbolized as in Figure 4.40 and fit well into the summary of reference data, although a huge spreading of the reference data exist. A strong dependence of UO_2 from O_2 content ($UO_{2\pm x}$) could explain this variation. This dependency is demonstrated in Figure 4.43, [36].

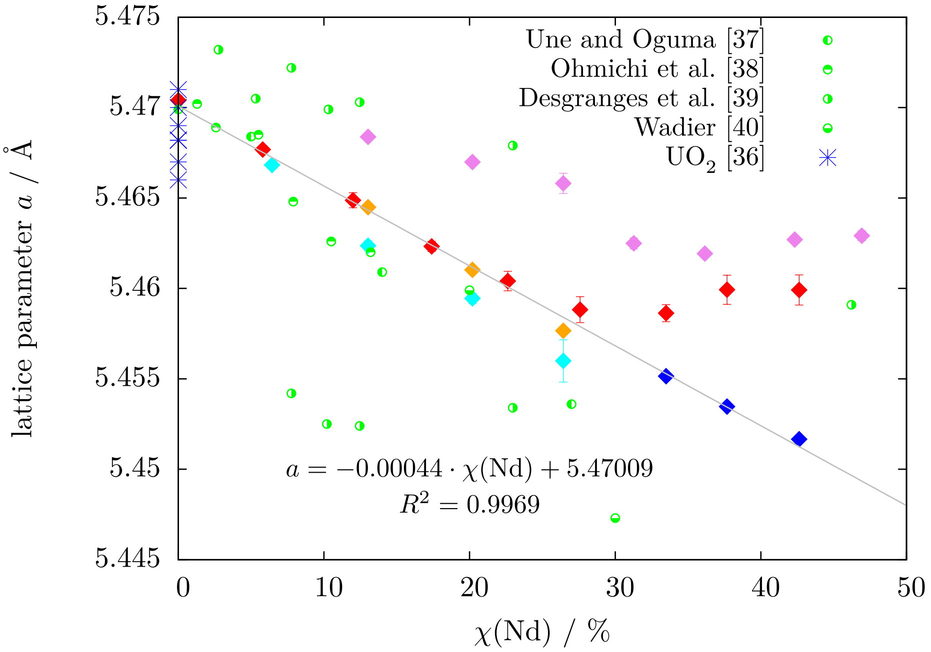

Figure 4.42.: Comparison of determined lattice parameter a investigated for the powders and particles in comparison with published reference data, as function of the Nd content.

The experimental data of pure UO_2, of this work, show a good correlation with results, published by Une and Oguma [37]. They also investigated the UO_2 / Nd_2O_3 system in detail and their results are included in Figure 4.42. Further investigations were published by Ohmichi et al. [38], they observed a single phase region for compositions with a Nd content up to 5 % and a two phase region. The data investigated for phase 1 by Ohmichi et al. [38] are also shown in Figure 4.42.

Desgranges et al. [39] investigated mixtures in a χ(Nd) range of 3-46 %. They report about an existence of two phases for all observed compoisitions. They concluded that the phase with the small lattice parameter correspond to the $(UNd)O_2$ phase. The phase with the higher a value, which was also observed, belongs to the $(UNd)O_{2-x}$ phase. The results of Desgranges et al. [39] are also shown in Figure 4.42. It can be observed, that their published lattice parameters strongly differ from other published data, as well as from the results of this work. Further compositions were investigated by Wadier [40].

The lattice parameter comparison (Figure 4.42) shows a good correlation of the experimental data achieved for the single phases of the fabricated powders (H_2:Ar atmosphere, $\vartheta = 1300\,°C$) and the data published by Une and Oguma [37], Ohmichi et al. [38], for the region with a Nd content $\geq 7\,\%$. The two phase region, observed in the powders treated in the reducing H_2:Ar atmosphere at

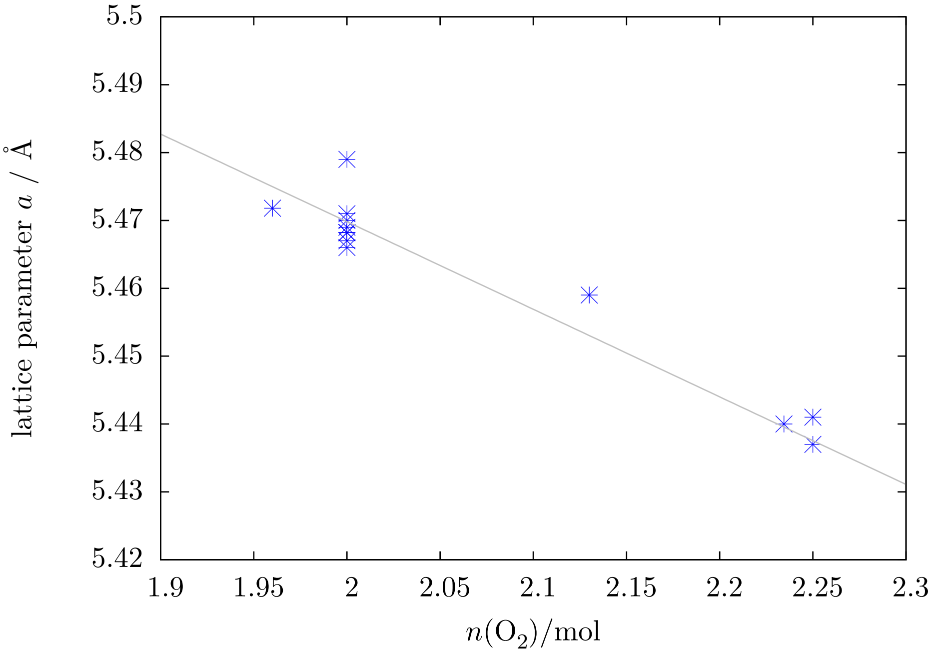

Figure 4.43.: Lattice parameter a of UO_x as function of O_2 content).

1300 °C, also agrees with the results of Une and Oguma [37], Ohmichi et al. [38], for a Nd content of 20 % the data of Wadier [40] were confirmed.

Desgranges et al. [39] observed two phases. Their second phase and the second phase observed for the powder compositions treated at 1300 °C in (H_2:Ar atmosphere show a good correlation (χ(Nd): 13.03 %, 20.20 % and 26.43 %). The value, they published for the $\chi(\mathrm{Nd}) = 46\,\%$ composition agrees with the achieved lattice parameter of the microspheres treated in the reducing H_2:Ar atmosphere at 1300 °C.

All published reference data were achieved with pellet sample, prepared by pressing of powders and sintering at high temperatures (1700-1800 °C). It can be concluded that the formation of single phase compositions with this fabrication techniques is difficult. In contrast to the prepared powders of this work, which show similar effects, the particles prepared by internal gelation method leads to single phase compositions. The results of this work showed that equilibrium solid solutions of the sensitive UO_2 / Nd_2O_3 system can be fabricated with the internal gelation technique.

5. Summary and Outlook

The present work shows that the preparation of UO_2 / Nd_2O_3 with Nd contents up to $\approx$ 45 % is possible by the internal gelation technique. ADUN solutions were used as precursor for the fabrication of the microspheres. During synthesis constant conditions regarding the gelification agents urea and HMTA were kept. U / Nd green bodies in a χ(Nd) range of $0 - 42.63$ % were synthesized.

Although the process was manual, an average particle mass with a small standard deviation was achieved. A spherical particle shape was proven by SEM and with optical microscopy. The green body diameter was measured and a particle density was calculated.

The thermal behavior of the U / Nd microspheres was investigated by TG/DSC, in the region of 550-700 °C the particle compositions with χ(Nd) $\leq$ 17.40 % transit endothermic accompanied with an stepwise mass loss. The spheres containing higher Nd amounts showed an exothermic effect. Moreover, an endothermic effect at $>$ 900 °C was observed for some samples. Detailed TG/DSC analyses of particles, with comparable initial conditions, should be performed in the future to investigate the thermal effects at high temperatures.

XRD analyses show orthorhombic and cubic crystal lattice structure of the particle compositions treated in air ($\vartheta = 1300$ °C), which agrees with SEM investigations. The lattice parameter of the cubic structure was determined. The result of this analyses goes in accordance with published data [33] and a crystallization as described in a phase diagram for higher temperature was confirmed. Detailed investigations on the orthorhombic structure should be performed in the future.

Investigation of the control group powders, treated in a reducing H_2:Ar atmosphere at 1300 °C, showed in a χ(Nd) range of 13-26.4 % a formation of two cubic phases. This goes in accordance to published data [39]. Comparisons with reference data shows that formation of a UO_2 / Nd_2O_3 single phase composition is difficult for this χ(Nd) range.

The particles, synthesized by internal gelation and treated in H_2:Ar atmosphere ($\vartheta = 1300$ °C) showed only one cubic phase, for the whole observed χ(Nd) range. However, the expected linear behavior according to Vegard's rule was observed for compositions χ(Nd) $\leq$ 27.59 %, only. An additional sintering process of the particles with compositions of χ(Nd) $\geq$ 33.49 % at a higher temperature ($\vartheta = 1600$ °C) for 5 hours led to the expected crystallization of a single phase UO_2 / Nd_2O_3 ceramic behaving to Vegard's rule.

The results of this work show that equilibrium solid solutions of the sensitive UO_2 / Nd_2O_3 system can be fabricated by the internal gelation synthesis route with Nd contents of $\leq$ 42.63 %.

Acknowledgment

This work was supported by the ASGARD project, which has received funding from the European Atomic Energy Community's 7th Framework Programme (FP7 2007-2011) under grant agreement No. 295825.

I would like to express my thanks to Prof. Dr. D. Bosbach for the opportunity to carry out the necessary activities of the present work at the Forschungszentrum Jülich GmbH, IEK-6: Nuclear Waste Management and Reactor Safety.

Thanks to Prof. Dr. U. W. Scherer for his interest in this work, the great degree of patience and being my supervisor.

Further on I would like to thank Dr. G. Modolo for supervising my work and for all the support and many suggestions he brought to me.

Special thanks to Dr. A. Bukaemskiy for explaining me the basis of the XRD analysis used in this work and his assistance.

I thank my colleagues J. Dellen, J. Heuser and S. Schmitz for the numerous XRD measurements, and Dr. M. Klinkenberg for explanations regarding the SEM and a nice time during the observations.

I also wish to thank Dr. S. Neumeier for all the help, and all members of the institute for their collaboration and the nice atmosphere they brought.

Finally, I thank the ASGARD community for the great time of rich experience and nice acquaintances that I could do.

References

[1] Kernenergie Weltreport 2011. *atw*, 4:271–276, April 2012.

[2] G. Choppin, J. Rydberg, and J.-O. Liljenzin. *Radiochemistry and Nuclear Chemistry.* Butterworth-Heinemann, 3. edition, 2001.

[3] K. H. Lieser. *Einführung in die Kernchemie.* Wiley-VCH, 3. edition, 1991.

[4] G. Faccanoni. A diagram of a pressurized water reactor. WWW, March, 23 2013. URL `http://www.texample.net/media/tikz/examples/TEX/pressurized-water-reactor.tex`.

[5] J. Magill, G. Pfennig, and J. Galy. Karlsruher nuklidkarte, 7th. EC–DG JRC–ITE, Karlsruhe, Germany, 2006.

[6] M. Volkmer. Basiswissen kernenergie. *Informationskreis Kernenergie Naturstrom Rheinland-Pfalz GmbH*, Juni 2007.

[7] A. Holleman and E. Wiberg. *Lehrbuch der anorganischen Chemie.* de Gruyter, 57–70 edition, 1964.

[8] S. Barrett, A. Jacobson, B. Tofield, and B. Fender. The preparation and structure of barium uranium oxide $BaUO_x^{3+}$. *Acta Crystallographica Section B: Structural Crystallography and Crystal Chemistry*, 38(11):2775–2781, 1982.

[9] A. Geist, K. Gompper, M. Weigl, and T. Fanghänel. Reduzierung der Radiotoxizität abgebrannter Kernbrennstoffe durch Abtrennung und Transmutation von Actinoiden: Partitioning. *NACHRICHTEN - Forschungszentrum Karlsruhe*, 2:97–102, 2004.

[10] Entsorgung von Kernkraftwerken – Eine technisch gelöste Aufgabe. WWW, March, 23 2013. URL `www.vgb.org/abfallmanagement.html`.

[11] C. Madic, B. Boullis, P. Baron, F. Testard, M. Hudson, J.-O. Liljenzin, B. Christiansen, M. Ferrando, A. Facchini, A. Geist, et al. Futuristic back-end of the nuclear fuel cycle with the partitioning of minor actinides. *Journal of Alloys and Compounds*, 444:23–27, 2007.

[12] M. Pouchon, G. Ledergerber, F. Ingold, and K. Bakker. Sphere-Pac and VIPAC Fuel. In R. J. Konings, T. R. Allen, R. E. Stoller, and S. Yamanaka, editors, *Comprehensive Nuclear Materials*, volume 3: Advanced Fuels/Fuel Cladding/Nuclear Fuel Performance Modeling and Simulation, chapter 11, pages 275–312. Elsevier, Oxford, February 2012.

[13] Advanced fuelS for Generation IV reActors: Reprocessing and Dissolution: ASGARD. WWW, March, 23 2013. URL `http://asgardproject.eu/download/var/files/poster1_full.jpg`.

[14] V. Vaidya. Status of sol–gel process for nuclear fuels. *Journal of Sol-Gel Science and Technology*, 46(3):369–381, 2008.

[15] C. Ganguly, H. Langen, E. Zimmer, and E. Merz. Sol-gel microsphere pelletization process for fabrication of high-density Tho_2 -2 % UO_2 fuel for advanced pressurized heavy water reactors. *Nuclear technology*, 73(1):84–95, 1986.

[16] H. Nickel, H. Nabielek, G. Pott, and A. Mehner. Long time experience with the development of HTR fuel elements in Germany. *Nuclear Engineering and Design*, 217:141–151, 2002.

[17] F. Charollais, S. Fonquernie, C. Perrais, M. Perez, O. Dugne, F. Cellier, G. Harbonnier, and M.-P. Vitali. CEA and AREVA R&D on HTR fuel fabrication and presentation of the CAPRI experimental manufacturing line. *Nuclear engineering and design*, 236(5):534–542, 2006.

[18] X. Fu, T. Liang, Y. Tang, Z. Xu, and C. Tang. Preparation of UO_2 kernel for HTR-10 fuel element. *Journal of Nuclear Science and Technology*, 41(9):943–948, 2004.

[19] F. Van Der Brugghen, M. Hermans, J. Kanij, A. Noothout, T. Van Der Plas, and H. Slooten. Sol-gel processes for the preparation of spherical thorium-containing fuel particles. Technical report, Keuring van Electrotechnische Materialen, NV, Arnhem (Netherlands), 1968.

[20] R. Förthmann. Die chemischen Grundlagen des Hydrolyseverfahrens zur Herstellung sphärischer Kernbrennstoffteilchen. Technical report, Forschungszentrum Jülich GmbH, 1973.

[21] A. Deptula and C. Majani. Sol–gel processes and their applications. Technical report, ENEA, 1986.

[22] J. L. Collins, M. Lloyd, and R. Fellows. The basic chemistry involved in the internal-gelation method of precipitating uranium as determined by pH measurements. *Radiochim. Acta*, 42: 121–134, 1987.

[23] P. A. Haas. HTGR fuel development: loading of uranium on carboxylic acid cation-exchange resins using solvent extraction of nitrate. *ORNL-TM-4955*, September 1975.

[24] P. A. Haas. HTGR fuel development: Use of $U0_3$ to load cation exchange resin for microsphere preparation. *ORNL-TM-3817*, September 1972.

[25] M. Matthias. Bragg diffraction. WWW, March, 23 2013. URL `http://upload.wikimedia.org/wikipedia/commons/c/ca/Bragg.svg`.

[26] V. Wheeler, R. Dell, and E. Wait. Uranium trioxide and the UO_3 hydrates. *Journal of Inorganic and Nuclear Chemistry*, 26(11):1829–1845, 1964.

[27] H. Daniels, S. Neumeier, A. Bukaemskiy, G. Modolo, and D. Bosbach. Fabrication of oxidic uranium-neodymium microspheres by internal gelation. *Progress in Nuclear Energy*, 57:106–110, May 2012.

[28] J. B. Nelson and D. P. Riley. An experimental investigation of extrapolation methods in the derivation of accurate unit-cell dimensions of crystals. *Proceedings of the Physical Society*, 57 (3):160, 1945.

[29] G. Williamson and W. Hall. X-ray line broadening from filed aluminium and wolfram. *Acta Metallurgica*, 1(1):22–31, 1953.

[30] P. M. Schaber, J. Colson, S. Higgins, D. Thielen, B. Anspach, and J. Brauer. Thermal decomposition (pyrolysis) of urea in an open reaction vessel. *Thermochimica Acta*, 424(1):131–142, 2004.

[31] E. A. Gusev, S. V. Dalidovich, and L. I. Krasovskaya. Investigation of urotropine thermal decomposition reaction in self-generated atmosphere by means of thermal analysis method. *Thermochimica acta*, 93:21–24, 1985.

[32] G. Benay, F. Hubert, and G. Modolo. Preparation of yttria-stabilized zirconia-ceria kernels as fuel precursors using internal gelation. *Radiochim. Acta*, 96:285–291, 2008.

[33] C. Keller and A. Boroujerdi. Phasengleichgewichte in den Systemen UO_2–UO_3–$NdO_{1.5}$ und $NpO_2 + x NdO_{1.5}$. *Journal of Inorganic and Nuclear Chemistry*, 34:1187–1193, 1972.

[34] S. Lang, F. Knudsen, C. Fillmore, and R. Roth. High temperature reactions of uranium dioxide with various metal oxides. Technical report, DTIC Document, 1956.

[35] R. Shannon. Revised effective ionic radii and systematic studies of interatomic distances in halides and chalcogenides. *Acta Crystallographica Section A: Crystal Physics, Diffraction, Theoretical and General Crystallography*, 32(5):751–767, 1976.

[36] International Centre for Diffraction Data (ICDD). PDF-2, 2007. 148,379 entries.

[37] K. Une and M. Oguma. Oxygen potentials of $(UGd)O_{2\pm x}$ solid solutions in the temperature range 1000–1500°C. *Journal of Nuclear Materials*, 115(1):84–90, 1983.

[38] T. Ohmichi, S. Fukushima, A. Maeda, and H. Watanabe. On the relation between lattice parameter and o/m ratio for uranium dioxide-trivalent rare earth oxide solid solution. *Journal of Nuclear Materials*, 102(1):40–46, 1981.

[39] L. Desgranges, Y. Pontillon, P. Matheron, M. Marcet, P. Simon, G. Guimbretiere, and F. Porcher. Miscibility gap in the U–Nd–O phase diagram: a new approach of nuclear oxides in the environment? *Inorganic Chemistry*, 2012.

[40] J. Wadier. R-4507. Technical report, CEA, 1973.

A. Appendix

List of chemicals used

Table A.1.: List of chemicals used

Application	Substance	Specifics	Distributor
particle & powder fabrication	$UO_2(NO_3)_2 \cdot 6\,H_2O$		Merck
	$Nd(NO_3)_3 \cdot 6\,H_2O$		Sigma Aldrich
	urea		Merck
	HMTA		Merck
	NH_4OH		Merck
	silicone oil		
	H_2:Ar		
ICP-MS measurement	Calibration Standards		CPI International
	HNO_3	Suprapur®	Merck
Miscellaneous	ultra pure H_2O		FZ Jülich
	H_2O		FZ Jülich
	HNO_3		Merck
	acetone		Merck

List of Tables

List of Figures

Figure A.1.: X-ray powder diffraction pattern of the Nd/U spheres, treated in air at 1300 °C.

Figure A.2.: X-ray powder diffraction pattern of the Nd/U spheres, treated in H_2:Ar at 1300 °C.

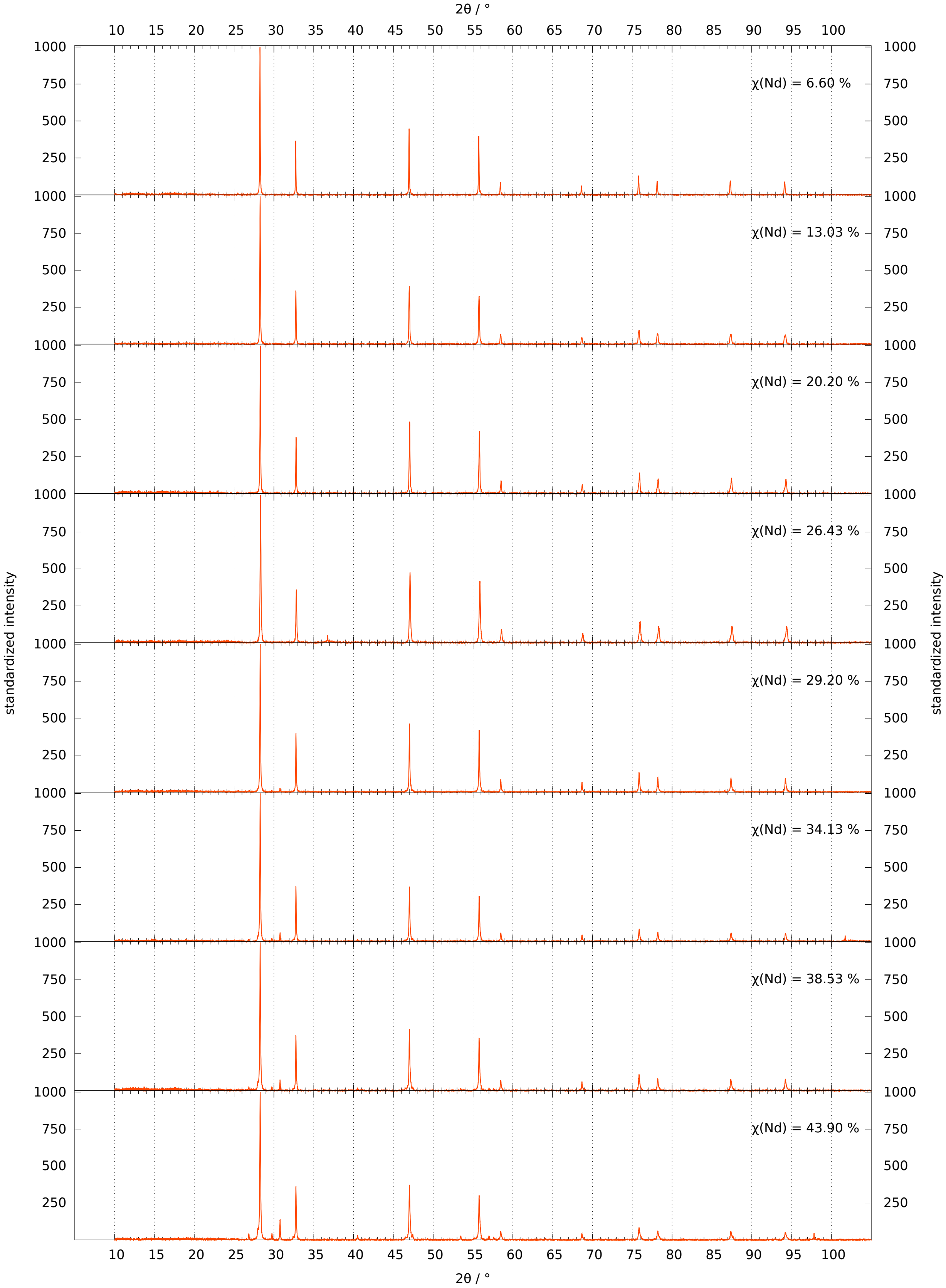

Figure A.3.: X-ray powder diffraction pattern of the Nd/U powders, treated in H_2:Ar at 1300 °C.